Discovery of small molecule modulators for Eps15 homology domain containing proteins

Inaugural-Dissertation
to obtain the academic degree
Doctor rerum naturalium (Dr. rer. nat.)

submitted to the Department of Biology, Chemistry, Pharmacy
of Freie Universität Berlin

by

Mohd Saif

Berlin
October 2022

The present work was carried out between March 2017 and June 2022 at the Max-Delbrück-Center for Molecular Medicine (MDC-Berlin) under the supervision of

Prof. Dr. Oliver Daumke

1st Reviewer: Prof. Dr. Oliver Daumke

2nd Reviewer: Prof. Dr. Udo Heinemann

Date of defense: 19th January 2023

Acknowledgment

I would like to thank Prof. Dr. Oliver Daumke for giving me the opportunity to work in his lab. His mindset of giving freedom to his doctoral students to do research and availability for discussion has made it a pleasure working with him.

Big thanks to our former lab member Dr. Claudia Matthäus (NIH, USA), who through her suggestions helped me with the cell-based assays. Thanks to Dr. Stephan Grunwald (Berlin, Germany) who helped me in the lab and showed me around when I was new. Huge thanks to Dr. Tobias Bock-Bierbaum, Dr. Audrey Xavier, Dr. Kathrin Funck, Dr. Katja Fälber, Dr. Jeff Noel, Dr. Stefan Grunwald, Elena Vazquez Sarandeses, Dr. Oleg Ganichkin, Dr. Yvette Roske, Yu Jie Li, Marius Weismehl, and Evangelia Nathanail for all the advice and discussions. Scientific discussions with them were always a good learning experience. I would also like to thank our technicians Sabine Werner, Jeanette Schlegel and Carola Bernert for their excellent support in providing a wonderful working environment. Thanks to Prof. Dr. Udo Heinemann for his suggestions during our joint seminars. Thanks to all the former and current Daumke and Heinemann lab members for helping with protocols, reagents, instruments, advice, and scientific discussions during our joint seminar and also for a wonderful office and lab environment.

I would like to thank the members of the screening platform at FMP, Berlin where I did my high-throughput screening. I would like to mention in particular Dr. Martin Neuenschwander and Andreas Oder who were available for scientific discussions and screening experiments.

Huge thanks to the online scientific community from various social media platforms who helped me with their suggestions and lively discussions. I learned a lot regarding drug discovery from them. Here, I would like to especially thank Dr. Adam Shapiro (Principal Investigator at Entasis Therapeutics) who was very patient and always responded to my queries. Online discussions with him cleared many of my concepts on enzyme kinetics in context to drug discovery.

Thanks to the Advance Light Microscopy facility (ALM) where I used the confocal microscope. Thanks to Sandra Raimundo from ALM who very patiently trained me at the confocal. I would like to thank my friend Tim Abel (AG Sommer) who helped with

the script writing in Fiji. It was a great help, thank you Tim. Thanks to Regina Piske from the Kettermann lab who provided access to and support with their plate reader. I would like to thank Dr. Tobias Bock-Bierbaum, Dr. Claudia Matthäus (NIH, USA), Elena Vazquez Sarandeses and Dr. Katja Fälber who proofread my thesis. Thanks to Dr. Yvette Roske who did the German translation for some parts of my thesis.

I would like to thank my parents and friends for their support. I would like to mention my mother for her unconditional love throughout my dissertation.

Selbstständigkeitserklärung

Hiermit bestätige ich, dass ich die vorliegende Arbeit selbstständig und nur unter Zuhilfenahme der angegebenen Literatur erstellt habe.

Geistiges Eigentum anderer Autoren wurde als entsprechend gekennzeichnet. Ebenso versichere ich, dass ich an keiner anderen Stelle ein Prüfungsverfahren beantragt bzw. die Dissertation in dieser oder anderer Form an keiner anderen Fakultät als Dissertation vorgelegt habe.

Berlin, den

_____

Unterschrift

Abbreviations

ADP	Adenosine diphosphate
AEBSF	4-(2-aminoethyl)benzenesulfonyl fluoride ATP
ATP	Adenosine triphosphate
AU	Arbitrary unit
AUC	Analytical ultracentrifugation
bp	Base pair(s)
C-terminus	Carboxy-terminus
DMSO	Dimethyl sulfoxide
DNA	Deoxyribonucleic acid
DOPS	1,2-dioleoyl-sn-glycero-3-phospho-L-serine
Drp1	Homo sapiens dynamin related protein-1
DTT	Dithiothreitol
E. coli	*Escherichia coli*
EDTA	Ethylenediaminetetraacetic acid
ER	Endoplasmic reticulum
GDP	Guanosine di-phosphate
GTP	Guanosine tri-phosphate
HEPES	4-(2-hydroxyethyl)-1-piperazineethanesulfonic acid
HPLC	High-performance liquid chromatography
HTS	high throughput screening
IMAC	Immobilized metal ion affinity chromatography
IPTG	Isopropyl β-D-1-thiogalactopyranoside
ITC	Isothermal titration calorimetry
KD	Dissociation constant
KO	knock out
LB	Lysogeny broth (medium)
LBS	Lipid binding site
MALDI-TOF-MS	Matrix-assisted laser desorption/ionization time of flight mass spectrometry
MDC	Max-Delbrück-Centrum für Molekulare Medizin in der Helmholtz-Gemeinschaft (Berlin)

MEF	mouse embryonic fibroblast
MES	2-(*N*-morpholino)ethanesulfonic acid
mmEHD2	mouse Eps 15 homology domain containing protein 2
mmEHD2ΔN	N-terminal deleted, mouse Eps 15 homology domain containing protein 2
mmEHD4	mouse Eps 15 homology domain containing protein 4
MW	Molecular weight
MWCO	Molecular weight cut-off
Ni-NTA	Nickel-nitrilotriacetic acid (nickel-charged resin)
N-terminus	Amino-terminus
OD600	Optical density, measured at 600 nm
P	Pellet
PAGE	Polyacrylamide gel electrophoresis
PCR	Polymerase chain reaction
PM	plasma membrane
PS	phosphatidyl-serine
RMSD	Root-mean-square deviation
SDS	Sodium dodecyl sulfate
SDS-PAGE	Sodium dodecyl sulfate polyacrylamide gel electrophoresis
SEC	Size exclusion chromatography
SN/S	Supernatant
TAE	Tris/Acetate/EDTA (buffer)
TB	Terrific broth (medium)
TBE	Tris/Borate/EDTA (buffer)
v/v	Volume per volume
w/v	Weight per volume
w/w	Weight per weight

Table of Contents

1. Summary

Eps15 (epidermal growth factor receptor pathway substrate 15) homology domain containing proteins (EHDs) comprise a family of dynamin-related ATPases. The four mammalian members of this family (EHD1-4) are involved in various endocytic and membrane trafficking pathways. Structural studies revealed that EHDs assemble at the surface of membranes to form ring-like filaments. Assembly on membranes was shown to stimulate the ATPase activity. In case of EHD2, ring-like oligomers were proposed to stabilize the neck of caveolae, which in turn regulates cellular fatty acid uptake.

The aim of this thesis was the identification of small molecule inhibitors that modulate EHD2 function and therefore cellular fatty acid uptake. Until now, there are no known inhibitors for EHD proteins. To this end, I optimized a malachite green-based ATPase assay to be robust and reproducible for a high-throughput setup. Drug screening was then employed to identify small molecules that inhibit the liposome-stimulated ATP hydrolysis of EHDs. Since EHD2 showed only a low ATPase activity, I initially screened for inhibitors against the closely related homologue EHD4. Validated hits were subsequently evaluated for inhibition against EHD2 in an HPLC-based setup. In this way, I identified chemical compounds that inhibited the ATPase activity of EHD4 and EHD2, and validated them in different biochemical assays. Interestingly, two of these small molecules were found to increase and decrease lipid droplet size in a cell-based assay. I also identified three inhibitors that were specific to EHD4 and did not interfere with the ATPase of EHD2 and the GTPase activity of Drp1, which was used as a control. Another exciting finding in this project were discovery of two compounds that accelerated the liposome-stimulated GTPase activity of Drp1.

The identified inhibitors may have future applications to explore the function of EHD- and Drp1-dependent cellular signaling pathways. Furthermore, they may be developed as therapeutic agents. Finally, my assay optimizations can be used to systematically and efficiently identify inhibitors for other dynamin superfamily members

2. Zusammenfassung

Eps15 (epidermal growth factor receptor pathway substrate 15) homology domain containing proteins (EHDs) umfassen eine Familie von Dynamin-verwandten ATPasen. Die vier Säugetiermitglieder dieser Familie (EHD1-4) sind in verschiedenen endozytischen- und Membran-Transportwegen beteiligt. Strukturelle Studien zeigten, dass sich EHDs an der Oberfläche von Membranen zu ringförmigen Filamenten zusammenlagern, wobei die Anordnung an Membranen die ATPase-Aktivität stimuliert. Im Fall von EHD2 wurden ringförmige Oligomere vorgeschlagen, die den Hals von Caveolae stabilisieren, was wiederum die zelluläre Fettsäureaufnahme reguliert.

Das Ziel dieser Arbeit war die Identifizierung niedermolekularer Inhibitoren, die die EHD2-Funktion und damit die zelluläre Fettsäureaufnahme modulieren. Bisher sind keine Inhibitoren für EHD-Proteine bekannt. Zu diesem Zweck optimierte ich einen auf Malachitgrün-basierenden ATPase-Assay, um ihn robust und reproduzierbar für einen Hochdurchsatz-Screen zu machen. Anschließend wurde ein Inhibitorscreening durchgeführt, um kleine Moleküle zu identifizieren, die die Liposomen-stimulierte ATP-Hydrolyse von EHDs hemmen. Da EHD2 nur eine geringe ATPase-Aktivität zeigte, suchte ich zunächst nach Inhibitoren gegen das engverwandte Homolog EHD4. Validierte Hits wurden anschließend in einem HPLC-basierten Setup auf Hemmung gegen EHD2 ausgewertet. Auf diese Weise habe ich chemische Verbindungen identifiziert, die die ATPase-Aktivität von EHD4 und EHD2 hemmen, die ich in verschiedenen biochemischen Assays validiert habe. Interessanterweise wurde festgestellt, dass zwei dieser kleinen Moleküle in einem zellbasierten Assay Einfluss auf die Lipidtröpfchengröße haben, d.h. diese vergrößern oder verringern. Ich identifizierte auch drei Inhibitoren, die spezifisch für EHD4 waren und nicht die ATPase von EHD2 und die GTPase-Aktivität von Drp1 stören, welche als Kontrolle verwendet wurden. Eine aufregende Entdeckung in diesem Projekt waren zwei Verbindungen, die die Liposomen-stimulierte GTPase-Aktivität von Drp1 beschleunigten.

Die identifizierten Inhibitoren können in zukünftigen Studien zur detaillierten Untersuchung der zellulären Funktion von EHD- und Drp1-abhängigen Signalwegen genutzt werden. Darüber hinaus können sie als Therapeutika weiter entwickelt werden. Letztendlich können meine Assay-Optimierungen auch verwendet werden, um Inhibitoren für andere Mitglieder der Dynamin-Superfamilie systematisch und effizient zu identifizieren.

3. Introduction

3.1. Endocytosis

Eukaryotic cells rely on transport of molecules across the plasma membrane, for example for nutrient uptake or signaling. This transport can be passive, e.g. mediated by channels, or active, e.g. mediated by transporters or endocytosis (Doherty & McMahon, 2009).

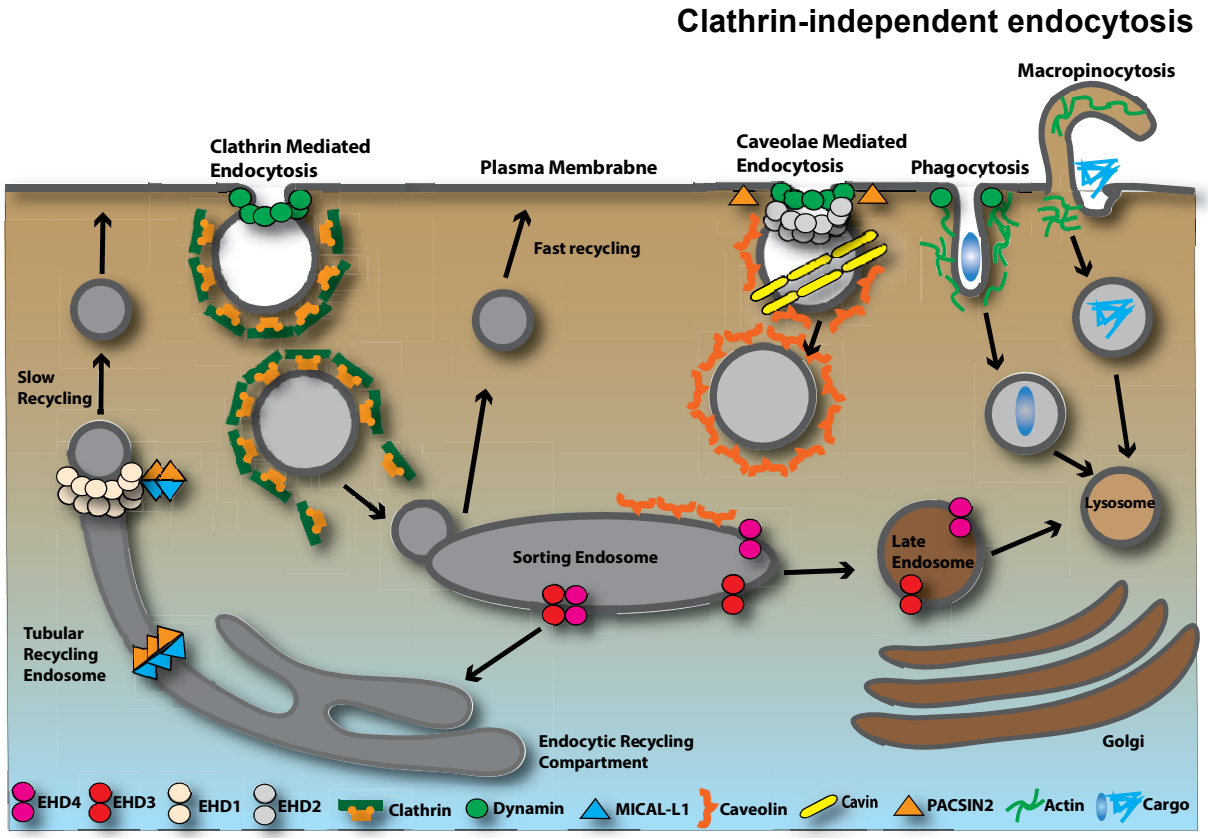

Figure 1: Different endocytic pathways and their itineraries. Multiple pathways function at the cell surface. These pathways can be divided on the basis of their requirement for clathrin and clathrin independent endocytosis (CIE). Endosomes formed from CIE pathways fuse with the sorting endosome from which material is sorted to the recycling endosome. The sorting endosome matures to the late endosomes, which subsequently fuses with the lysosomes. Dynamin superfamily protein members have been mentioned in their respective pathways. Figure modified and redrawn (de Souza et al., 2009; Joseph Jose Thottacherry, 2019).

Endocytosis is a key cellular process required for nutrient uptake, regulation of signaling and maintaining plasma membrane compositional homeostasis. Multiple endocytic mechanisms operate in the cell (see Figure 1). There have been many ways

to group these pathways (Conner & Schmid, 2003; Edeling et al., 2006; Joseph Jose Thottacherry, 2019; Mayor & Pagano, 2007). One major criterion is the requirement of clathrin in clathrin-mediated endocytosis (CME) or the uptake in clathrin-independent endocytosis (CIE) (Joseph Jose Thottacherry, 2019; Kirkham & Parton, 2005; Mayor & Pagano, 2007; Mayor et al., 2014). It is estimated that about 70% of extracellular uptake occurs via CIE (Howes et al., 2010; Sandvig et al., 2011; Shvets et al., 2015).

Cargo uptake occurs via receptors located in the plasma membrane. Cargo binding leads to the clustering of these receptors and the formation of membrane invaginations, which further progresses to form vesicles. Transport occurs by the trafficking of membrane vesicles inside the cell (Ross et al., 2008). CME is the prime example for such a mechanism. An example for CIE is the caveolae-dependent pathway. In this thesis, the caveolar system and its role in fatty acid uptake will be further elaborated. In subsequent chapters, the involved key players, dynamin and the dynamin-related Eps15-homology domain containing proteins (EHDs), will be introduced in detail.

3.2. Caveolae

With the advent of electron microscopy, small cellular compartments could be appreciated for the first time. Caveolae comprised one such example, which were discovered by electron microscopists Palade and Yamada in 1950s in the plasma membrane of endothelial cells (Palade, 1953; Yamada, 1955).

Caveolae are “sac/cave like” invaginations of the plasma membrane and are 70-100 nm in diameter (see Figure 2). Caveolae are enriched in cholesterol, sphingolipids and ceramides, thereby providing a reservoir (Parton & del Pozo, 2013; Zhou et al., 2020). They are present in most cell types but found abundantly in muscle cells, astrocytes, fibroblasts, endothelial cells and adipocytes (Cameron et al., 1997; Conner & Schmid, 2003; Joseph Jose Thottacherry, 2019; Matthaeus & Taraska, 2021; Parton & del Pozo, 2013).

3.2.1. Structure and formation of caveolae

Caveolae are composed of several proteins (see Figure *2*), which are responsible for its formation and stabilization. These are caveolin (Cav), an integral membrane protein having three orthologues in human (Cav1-3), Cavin (Cavin1-4), the BAR domain protein PACSIN2 and EHD2 (see Figure 2) (B. Han et al., 2016; Lamaze et al., 2017).

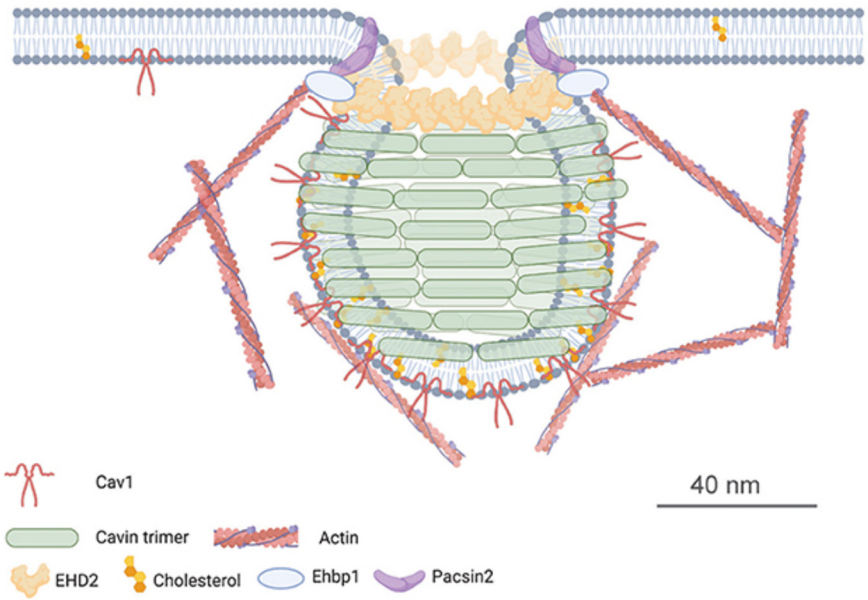

Figure 2: Structure of caveolae and its components. The proteins associated with caveolae are depicted in this figure. Figure taken from (Matthaeus & Taraska, 2021).

Caveolin-1 (Cav1) and Cavin1 were shown to be the most important players for caveolae formation (Drab et al., 2001; Hill et al., 2008; Lipardi et al., 1998; Liu. et al., 2008; Razani et al., 2002). Caveolae biogenesis is tightly coupled to plasma membrane composition and is thought to be driven by cholesterol-sensitive oligomerization of caveolin1 and subsequent association with cavin proteins (Parton & del Pozo, 2013). Cav1 is a 178 amino acid long integral membrane protein that adopts a hairpin-like topology in the lipid bilayer such that N and C- terminal are exposed to the cytoplasm of the interior cell (Root et al., 2015). Cryo-EM has shown that the human caveolin-1 complex is composed of 11 protomers organized into a tightly packed disc that contains an outer rim and a central β-barrel turn and α-helical spokes (Porta et al., 2022).

Loss of Cav1 results in a complete loss of caveolae (Drab et al., 2001; Liu. et al., 2008) while overexpression of Cav1 in caveolin knockout (KO) cells was sufficient to induce caveolae re-formation (Fra et al., 1995; Lipardi et al., 1998). Cav1-3 and Cav1/Cav3-deficient mice were viable and fertile but showed muscular, pulmonary and lipid metabolism disorders (Park et al., 2002; Prakash et al., 2000; Razani et al., 2001; Razani et al., 2002).

Also cavin coat proteins are proposed to induce membrane remodeling to create the cave-like invaginations of caveolae. Cavin proteins are recruited from the cytosol, oligomerizes into trimers and surround the caveolar membrane resulting in a structured caveolar coat (Kovtun et al., 2015; Ludwig et al., 2013). Loss of cavin1 results in a loss of caveolae leading to a flat plasma membrane (Hill et al., 2008; Liu. et al., 2008).

It is supposed that the F-BAR protein PACSIN2 is important for bending the membrane during caveolae formation (Seemann et al., 2017). It contains a F-BAR domain, which is associated with the generation or maintenance of membrane curvature (Hansen et al., 2011).

The role of dynamin and EHD2 proteins in regards to caveolar mobility, are discussed later (in sections 3.3.5 and 3.5 respectively). Caveolar mobility is important for its physiological function, as outlined below.

3.2.2. Functions of caveolae

The wide array of functions of caveolae across many different pathways, highlights its importance in signaling and physiology (Matthaeus & Taraska, 2021). Previous studies revealed that caveolae are involved in cellular lipid and fatty acid uptake (Matthaeus et al., 2020; Pilch & Liu, 2011), endothelial transcytosis of large molecules (Cheng & Nichols, 2016; Frank et al., 2009), regulation of the endothelial nitric oxide synthase (Förstermann & Sessa, 2012; Matthaeus et al., 2019), neurovascular coupling (Chow et al., 2020), viral internalization (Pelkmans et al., 2001; Xing et al., 2020) and pigmentation in melanocytes (Domingues et al., 2020). Caveolae are estimated to account for more than 50% of the cell surface area in adipocytes (Hubert et al., 2020) and its dense packing in endothelial and adipocytes hints towards a specialized role in homeostasis and metabolism. It serves as a unique membrane domain for plasma membrane proteins involved in several signaling pathways (Matthaeus & Taraska,

2021). KO mice model studies from Cav1 and Cavin1-4 have shown that caveolae are involved in lipid metabolism, blood pressure changes, muscular dystrophy and cardiomyopathies (Cheng & Nichols, 2016; Pilch & Liu, 2011).

Altered levels of caveolin gene expression, mutated and/or modified caveolae endocytosis and trafficking pathways can be linked to metabolic diseases. These include obesity and lipodystrophy (Catalán et al., 2008; Matthaeus et al., 2020; Pilch & Liu, 2011; Schrauwen et al., 2015), cancer (Carver & Schnitzer, 2003; Ketteler & Klein, 2018; Martinez-Outschoorn et al., 2015) as well as cardiovascular disease (Bing Han et al., 2016; Lian et al., 2019), neurological disease. As such, caveolae is a therapeutic target for its role in the above mentioned diseases.

Formation and trafficking of caveolae depends on membrane remodeling events like membrane deformation and fission. These events rely on protein machineries that are recruited to the caveolar membrane (Bonifacino & Glick, 2004). For example, proteins of the dynamin superfamily play a critical role in various membrane remodeling processes in the cell (Praefcke & McMahon, 2004).

3.3. Dynamin superfamily of proteins

Proteins of the dynamin superfamily of proteins are large GTP-binding (G) proteins involved in different cellular processes e.g. division of mitochondria, peroxisomes, chloroplast, viral host defense mechanism, budding off transport vesicles, fission and fusion (see Figure 3) (Praefcke & McMahon, 2004). They utilize the energy from GTP hydrolysis to actively remodel membranes and as such, are known as mechano-chemical enzymes (Faelber et al., 2013). Dynamin superfamily of proteins can be distinguished from other GTPases by their low micro-molar affinity for nucleotides, relative high basal GTPase enzymatic activity and their lipid dependent oligomerization that leads to self-assembly and stimulated GTPase activity (Daumke & Praefcke, 2016). Members of this protein family are segregated into classical dynamins and dynamin related proteins.

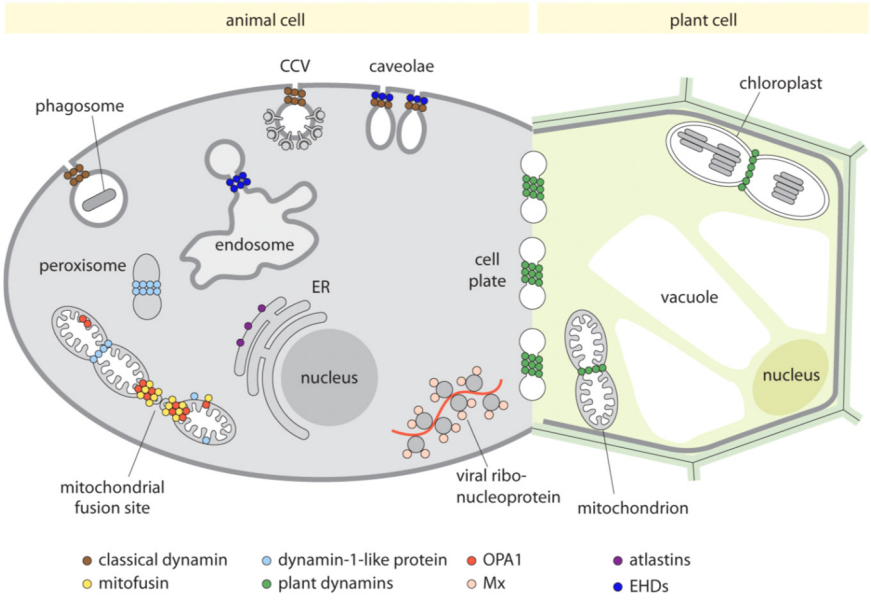

Figure 3: Dynamin superfamily of proteins. Cellular localization and their functions. Figure modified from (Alasdair Steven, 2016).

3.3.1. Dynamin proteins

Discovered in 1987 as a GTPase that was co-purified with brain microtubules (Obar et al., 1990; Shpetner & Vallee, 1989), dynamins are the best characterized protein of the dynamin superfamily. Invertebrates have a single dynamin gene (Clark et al., 1997) and mammals have three isoforms of dynamin (Dyn1-3). The isoforms share the same domain organization and have 80% sequence homology (Ferguson & De Camilli, 2012). Dyn1 shows high expression in neurons (Ferguson et al., 2009; Liu et al., 2008) whereas Dyn2 is expressed ubiquitously (Cao et al., 1998; Raimondi et al., 2011). Dyn3 is also found in neurons but at lower levels than Dyn1 and in testis. (Cao et al., 1998; Raimondi et al., 2011). The overall domain organization includes an N-terminal GTPase domain, a bundle signaling element (BSE), stalk domain, a pleckstrin homology domain (PH) and a C-terminal proline rich domain (PRD) (see Figure 4) (Faelber et al., 2013).

The role of dynamin proteins in endocytosis was shown when the mutations responsible for the temperature sensitive paralytic phenotype of *Drosophila melanogaster* shibire mutants were mapped to the dynamin gene. (Chen et al., 1991; van der Bliek & Meyerowitz, 1991). The three closely related dynamins have been

shown to mediate cleavage of clathrin-coated vesicles in various cellular functions e.g. recycling of synaptic vessels in neurons, uptake of nutrients or signaling factors in almost all cell types (Faelber et al., 2013). They are also involved in clathrin-independent budding events at caveolae and phagosomes (see Figure 3) (Praefcke & McMahon, 2004).

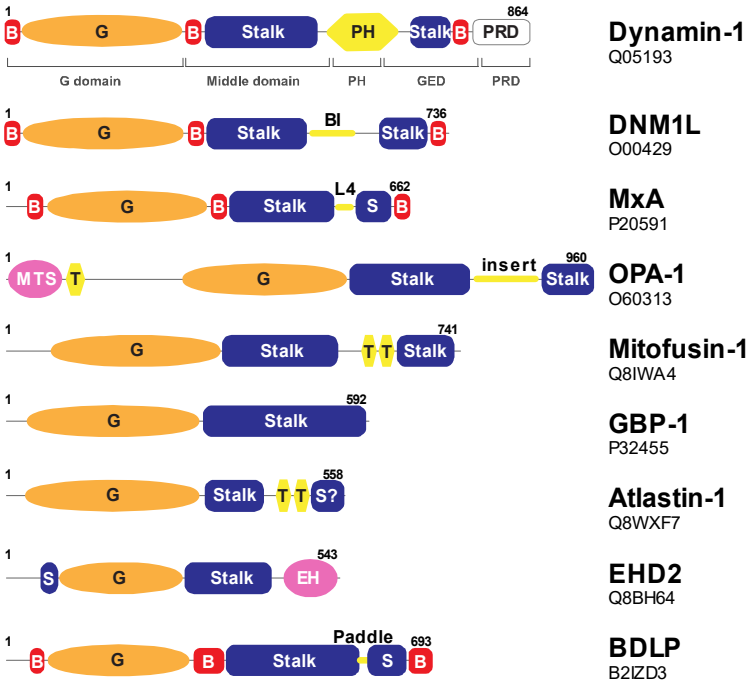

Figure 4: Domain architecture of dynamin superfamily proteins. Structure-based domain architecture of dynamin superfamily proteins, with Uniprot accession number indicated (G: G-domain; B: bundle-signaling element (BSE); MTS: mitochondrial targeting sequence, S: stalk; PH: pleckstrin homology domain (PH); PRD: Proline rich domain; BI, B insert; L4: Loop 4; MTS: mitochondrial targeting sequence; T: predicted transmembrane domain; EH: Eps15 homology domain). The C-terminal region of atlastin-1 was not present in the crystal structure and has not been identified as part of the stalk. Figure modified from (Faelber et al., 2013)

3.3.2. Dynamin related proteins

Several dynamin-related proteins mediate various cellular functions. Myxovirus resistance proteins (Mx proteins) are induced by interferons and confer resistance against RNA viruses (Haller & Kochs, 2011; Pavlovic et al., 1993). Bacterial dynamin-like proteins (BDLPs) have been proposed to mediate membrane tethering

and conferring resistance against phage infection (Guo & Bramkamp, 2019; Low & Löwe, 2006). Atlastins localize to newly formed three-way junction at the ER and mediates tethering and membrane fusion (Prakash et al., 2000; Wang et al., 2016). Guanylate-binding proteins (GBPs) are expressed in response to interferons and provides host defense against pathogens (Tripal et al., 2007). Eps15 homology domain containing proteins (EHDs) (Daumke et al., 2007) are involved in the regulation of membrane trafficking at caveolae and endosomes (Naslavsky & Caplan, 2018). Mitofusin proteins (Cao et al., 2017; Hales & Fuller, 1997) and optic atrophy protein 1 (OPA1) facilitate the fusion of outer and inner mitochondrial membranes respectively (Alexander et al., 2000; Liu & Chan, 2017). Dynamin-related protein 1 (Drp1) mediates the division of peroxisome and mitochondria (Gammie et al., 1995; McBride & Frost, 2016).

3.3.3. GTP hydrolysis in dynamin proteins

Common feature in all dynamin superfamily proteins is their ability to assemble into oligomers on a suitable membrane template. For example, dynamin can self-assemble around microtubules or at the neck of clathrin coated vesicles (Takei et al., 1995). Self-assembly of dynamin proteins can be reconstituted *in vitro* on membrane templates like liposomes (Warnock. et al., 1996). Once oligomerized on a lipid template, the low basal GTPase activity of dynamin is stimulated up to 200-fold. It has been shown that the stimulated GTPase is due to the conformational changes associated with dimerization of the GTPase domain that result in the reorientation of the catalytic active residues favoring nucleotide hydrolysis (Daumke & Praefcke, 2016).

The G-domain in GTPases contains a set of five (G1-G5) sequences that are responsible for nucleotide binding and hydrolysis (see Figure 5). **G**xxxx**GKS**/**T** (G1), **T** (G2), **D**xx**GQ**/H/T (G3), T/N**K**x**D** (G4), C/S**A**K/L/T (G5) (x stands for any amino acid and invariant residues are in bold) (Daumke & Praefcke, 2016; Hall, 2004). All of these motifs are conserved in dynamin superfamily proteins except G5 that shows variations. G1 is known as phosphate-binding (P-) loop, whereas G2 and G3 are also termed switch I and switch II, respectively. The P loop mediates nucleotide binding by wrapping around the β-phosphate. Its terminal residue, serine or threonine, coordinates with a Mg^{2+} ion, which is essential for nucleotide hydrolysis. The P-loop also participates in

stabilizing the transition state of nucleotide hydrolysis. The conserved threonine of the G2 motif mediates a direct and the conserved aspartate a water-mediated contact for Mg^{2+} ion binding. The G2 and G3 motif also interact with the γ-phosphate of the nucleotide directly and undergo nucleotide dependent conformational change (Daumke & Praefcke, 2016).

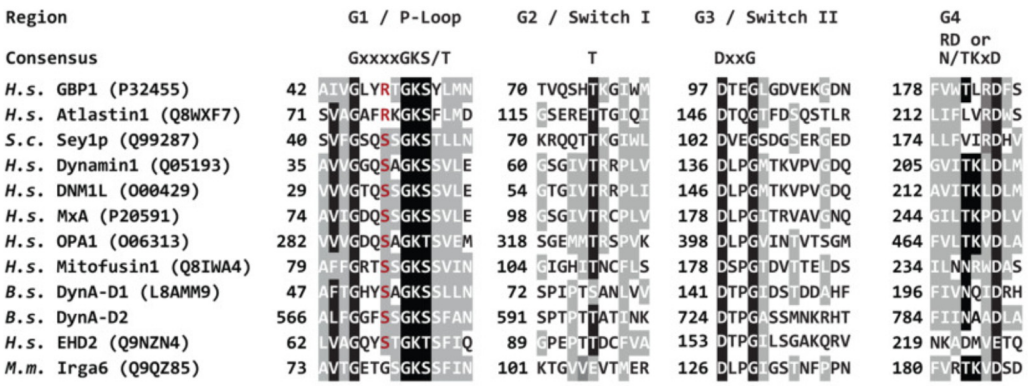

Figure 5: Catalytic mechanism of dynamin superfamily of proteins. Sequence alignment of dynamin superfamily of proteins in the G1–G4 motifs. Conserved canonical residues are highlighted in black or dark gray, other conserved residues in light grey. The catalytic arginine and serine in the P-loop are shown in red. Figure taken from (Daumke & Praefcke, 2016).

G4 motif is involved in binding to the base and as such recognizes specific nucleotide. In Dynamin, the G4 motif mediates specific binding to the guanine base in trans via D211 of the opposing monomer (Chappie et al., 2010).

The non-conserved G5 motif may interact with the guanine base or the ribose backbone of the nucleotide. Partially invariant asparagine and arginine residues can be found at positions roughly equivalent to G5 motif (Mears et al., 2007).

3.3.4. The GTP-dependent power stroke

Dynamins are mechano-chemical GTPases which convert the energy of GTP hydrolysis to a mechanical output. This output is mostly exploited for remodeling of membranes e.g. dynamin was the first protein shown to actively catalyze membrane fission. In this process, dynamin is recruited to the neck of clathrin coated vesicles via

interaction of its PRD with Src-homology 3 domain (SH3) of BAR domain proteins, e.g. Bin/Amphiphysin (Soulet et al., 2005), endophilin (Ringstad et al., 1999), SNX9 (Daumke et al., 2014). Dynamin then oligomerizes into a helical polymer via three interfaces in the stalk domain. This leads to GTP-dependent membrane constriction and, finally, membrane scission upon GTP hydrolysis (Antonny et al., 2016). The nucleotide-hydrolysis driven conformational change that leads to the scission has been termed the “power stroke” (see Figure 6) (Chappie et al., 2010). This power stroke is thought to pull the adjacent dynamin filaments along each other thereby constricting the underlying membrane in a sling-like fashion. Putative role of power stroke is also present in dynamin like proteins e.g. Drp1 in mitochondrial membrane scission (Labrousse et al., 1999; Smirnova et al., 2001) and Atlastin in pulling membranes together during membrane fusion (Wang et al., 2016).

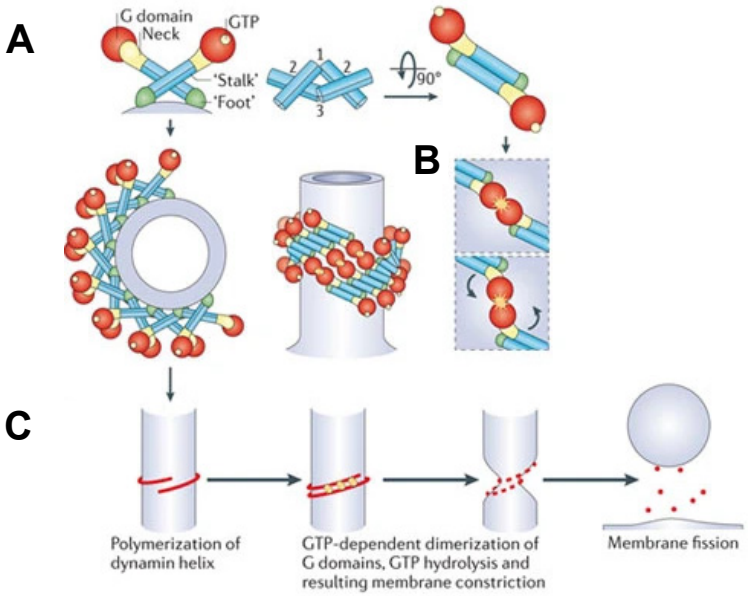

Figure 6: Putative mechanism of dynamin-mediated membrane fission. (A) Schematic representation of dynamin dimers and of helical dynamin polymers around a tubular template in two different orientations (90 degrees rotation). Red- G-domain, Blue- Stalk domain, Green- PH domain, Purple- PRD domain. (B) The GTP-dependent dimerization of G domains between adjacent rungs of the dynamin helix (highlighted in yellow stars, longitudinal view of the helix). (C) Schematic view of the key steps leading to dynamin-mediated membrane fission. Figure taken from (Ferguson & De Camilli, 2012).

3.3.5. Putative role of Dyn2 in caveolae scission

It has been shown that GTP-dependent caveolae internalization is dependent on Dyn2 (Henley et al., 1998; Oh et al., 1998). Previous studies indicated that Dyn2 localizes to caveolae in kidney cells (Yao et al., 2005), in overexpressing MEFs or endothelial cells (Matthaeus et al., 2020; Shajahan et al., 2004). Over-expression of Dyn2-K44A, a non-GTP hydrolyzing mutant, reduced caveolar mobility, detachment and trafficking from the plasma membrane (Matthaeus & Taraska, 2021; Oh et al., 2012; Pelkmans et al., 2001; Senju et al., 2011). These data indicate the involvement of dynamin in caveolae scission and detachment.

However, more recent studies (Larsson et al., 2022; Matthaeus et al., 2022) revealed that a loss of Dyn2 does not impair caveolae internalization to a large extent. In fact quantitative correlative light and electron microscopy failed to localize dynamin to caveolae domains at the plasma membrane in various cell types (Matthaeus et al., 2022). Additionally, the lack of all three dynamin isoform also did not alter caveolae number at the plasma membrane (Matthaeus et al., 2022). Furthermore, when Dyn2 was overexpressed caveolae mobility was reduced (Larsson et al., 2022) suggesting that dynamin is not directly involved in caveolae membrane scission.

Drp1 and EHD proteins have been studied in this thesis and will thus be introduced in more detail in the subsequent chapters.

3.3.6. Dynamin related protein-1 (Drp1)

Drp1, also known as dynamin 1-like protein, was discovered in the mid 90ies during a genetic screening in budding yeast *Saccharomyces cerevisiae* (the yeast homologue is known as Dnm1) (Okamoto & Shaw, 2005). Drp1 is an 80 kDa protein and has three domains, a G-domain, a stalk and the BSE (see Figure 4). Drp1 is expressed ubiquitously in all tissues but shows higher expression levels in muscle, brain and heart (Nunnari & Suomalainen, 2012).

It has been shown that Drp1 mediates the fission of mitochondria (Labrousse et al., 1999; Smirnova et al., 2001) and peroxisomes (Koch et al., 2003) (see Figure 3). Drp1 is produced in the cytosol and is recruited to the mitochondrial surface by receptor

proteins present on the mitochondrial outer membrane (mom) at discrete foci (Benard & Karbowski, 2009). There are currently four known Drp1 receptor proteins: Fis1, MFF, MID49 and MID51 (Chan, 2012). Out of these, depletion of MFF has been shown to cause the greatest defect in mitochondrial fission (Losón et al., 2013; Otera et al., 2010). Once recruited to mitochondria, Drp1 self assembles into an oligomeric ring that drives constriction and scission of the mitochondrial tubule (see Figure 7) (Fahrner et al., 2016; Ingerman et al., 2005).

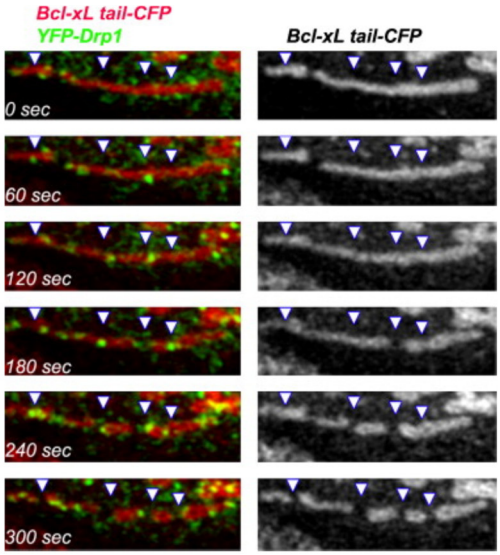

Figure 7: Drp1 mediates mitochondrial fission. Drp1 is recruited to the outer mitochondrial membrane and initiates the mitochondrial division. Time-lapsed confocal microscopy picture series showing mitochondrial scission events in HeLa cells. Colored pictures show mitochondria in red and Drp1 in green. The corresponding monochrome pictures on the right are shown for better identification of scission sites. Figure is taken from (Benard & Karbowski, 2009).

3.3.7. Drp1-related disease

Mitochondria are essential organelles for the eukaryotic cells. They are involved in respiration, energy production, intermediary metabolism, calcium ion signaling and apoptosis. Defects in mitochondrial fusion were observed in several neurodegenerative diseases, including Charcot-Marie-Tooth disease type 2A, Parkinson´s disease and autosomal dominant optic atrophy (Frohlich et al., 2013; Vanstone et al., 2016).

De novo biogenesis of mitochondria does not occur but they proliferate by the division of pre-existing mitochondria (Shiota et al., 2015). As such, their fission is crucial to maintain their number and function. Dissipation of mitochondrial membrane potential or apoptotic stimulus induces mitochondrial recruitment of Drp1. This stimulates mitochondrial fission, while fusion is inhibited (Cassidy-Stone et al., 2008; Frank et al., 2001; Otera & Mihara, 2011).

As a key component of mitochondrial fission, Drp1 is essential for proper mitochondrial function and critical in the functioning of mammalian brain and for survival (Fahrner et al., 2016). Constitutive homozygous KO mice for Drp1 die during embryogenesis (Ishihara et al., 2009). Ablation in mouse brain leads to developmental defects of the cerebellum (Wakabayashi et al., 2009), whereas conditional ablation of Drp1 in mature Purkinje cells leads to gradual cell death and degeneration in adults (Kageyama et al., 2012). All these phenotypes are linked to impaired mitochondrial fission.

In humans, three probands have been reported with heterozygous dominant *de novo* missense mutations in the Drp1 gene. A new born girl with microcephaly, abnormal brain development, optic atrophy and hypoplasia, persistent lactic acidemia and a mildly elevated plasma concentration of very long-chain fatty acids (Waterham et al., 2007) died 37 days after birth and carried a mutation leading to an A395D exchange. Consequently, defects in mitochondrial and peroxisomal function were observed (Waterham et al., 2007). A second proband expressing the G326D variant of Drp1 was diagnosed with developmental delay, refractory epilepsy. He showed hyper-fusion of the mitochondrial network with abnormal and concentric cristae in ultra-morphological analyses (Vanstone et al., 2016). The third proband expressing the R403C missense mutation had normal childhood development, but minor metabolic insults resulted in status epilepticus, refractory epilepsy, encephalopathy, developmental regression, myoclonus and brain atrophy (Fahrner et al., 2016). All three mutations can be located to the stalk region of Drp1, which is important for the assembly into oligomeric rings (Frohlich et al., 2013). Accordingly, previous work has shown that these mutations affect the oligomerization of Drp1 (Fahrner et al., 2016; Waterham et al., 2007). Yeast two hybrid system has shown that the effect of the mutation preventing Drp1 oligomerization is stronger for A395D compared to R403C. (Fahrner et al., 2016). This could explain the less severe and mild clinical phenotype of R403C mutation compared to the neonatal lethal mutation of A395D.

Two more conditions have been reported for individuals with Drp1 mutations. A heterozygous truncating mutation in siblings led to encephalopathy, hepatic dysfunction and, giant intra-neuronal mitochondria. Both of them died within their first month (Yoon et al., 2016). Another *de novo* missense mutation led to developmental delay (Roback, 2015).

3.4. The EHD family

Eps15-homolgy domain containing proteins (EHDs) comprise a highly conserved dynamin-related protein family with four members in mammals (EHD1-4) and one in *Drosophila melanogaster* (Past-1) and *Caenorhabditis. elegans* (Rme-1). EHDs are expressed specifically in different tissues: While EHD1 is highly expressed in kidney, lung and testis, EHD2 shows high expression in adipose, heart and skeletal muscles (Matthaeus et al., 2020; Matthaeus & Taraska, 2021), EHD3 in brain, kidney, lung and muscles and EHD4 appears abundantly expressed (Uhlén et al., 2015).

Similar to other members of the dynamin superfamily, EHDs have a low nucleotide affinity, the ability to tubulate liposomes *in vitro*, the propensity to oligomerize around lipid tubules forming ring like structures and stimulated nucleotide hydrolysis after membrane binding (Daumke et al., 2007).

3.4.1. Structural organization of EHD proteins

Members of the EHD family share a similar basic domain architecture with the dynamin superfamily (see Figure 4). The first determined EHD structure was that of EHD2 (Daumke et al., 2007). This structure helped in understanding the domain functions, dimerization, residues important for ATP hydrolysis and membrane binding.

EHDs have a N-terminal G-domain followed by a helical domain which is connected to the C-terminal EH domain by a short flexible linker (see Figure 8A) (Daumke et al., 2007). The N-terminal G-domain of EHDs binds and hydrolyzes ATP as shown in *C. elegans* (Lee et al., 2005) and in mammals (Daumke et al., 2007; Melo et al., 2017; Moren et al., 2012; Shah et al., 2014). Despite its ATP-binding activity, the domain is

still referred to as G-domain due to its sequence and fold similarity with other G-domains (Daumke et al., 2007).

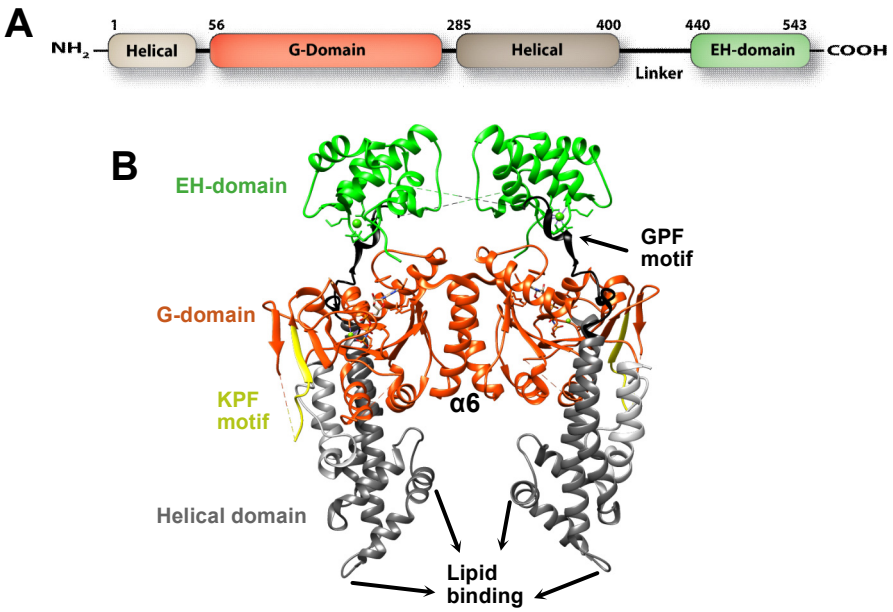

Figure 8: EHD2 structural organization. (A) Domain structure of EHD2 protein. Numbering is according to mouse EHD2. (B) EHD2 dimer (PDB: 2QPT). Molecules are colored as per the domain organization in A. EH domain locks on the opposing molecule in the dimer.

The G-domain exhibits a typical dynamin G-domain fold containing the five signature motifs (G1-G5). Similar to dynamin, it also contains two additional β-strands close to the switch I region. It has 6 parallel and two anti-parallel β-strands surrounded by 7 α-helices (α1- α7) (see Figure 8B) (Daumke et al., 2007; Reubold et al., 2005). More specifically, Met223 after the G4 specificity motif protrudes into the nucleotide binding site and sterically inhibits binding of the amino group in the guanine base. Thus, Met223 may contribute to the ATP-binding specificity of EHDs (Daumke et al., 2007). Residues participating in ATP hydrolysis are found in the two switch regions of the G-domain. These two switch regions along with the surrounding area form another conserved interface (Daumke et al., 2007) (Melo et al., 2017) for oligomerization (see Figure 9). This so-called G-interface extends across the nucleotide binding site and is a conserved feature in dynamin superfamily of proteins. Mutations in G-interface residues make EHD2 either deficient or slow in ATP hydrolysis and leads to a disruption of liposome-stimulated ATPase activity (Daumke et al., 2007).

The helical domain of EHD2 is composed of two α-helices from the N-terminal region of the G domain (α1 and α2) and 5 helices from the C-terminal region (α8- α12). Helix α8 acts as an organizing scaffold. Furthermore, the membrane-binding site has been located in this domain (Daumke et al., 2007; Shah et al., 2014) (see Figure 8B). Two EHD2 molecules form a scissor-shaped dimer (see Figure 8B), in which the membrane is proposed to bind between the blades. Mutational studies have shown that amino acids present near the tip are involved in membrane binding (Daumke et al., 2007). The same was also shown by studies involving site-directed spin labelling approach combined with EPR spectroscopy (Shah et al., 2014).

The helical domain is connected to the EH-domain via a 40 amino acid long linker containing a GPF motif (residues 420-422).

A sequence stretch at the very N-terminus is highly conserved in the EHD family. X-ray and electron paramagnetic resonance (EPR) studies have shown that 8 amino acids from the N-terminus fold back into a conserved hydrophobic pocket of the G-domain in the EHD2 structure. Upon recruitment to the membrane, the N-terminal residues are released into the membrane (Shah et al., 2014). This switch mechanism is thought to negatively regulate membrane interaction, an idea which was supported by an increased membrane recruitment of an N-terminal deleted EHD2 variant when expressed in cells (Shah et al., 2014). The N-terminal switch might also play a role in caveolar targeting of EHD2 by influencing the positioning of a peripheral loop of the G-domain containing an ‘KPF’ linear motif (also known as ‘KPF loop’) (see Figure 8B). It has previously been shown that the KPF loop is involved in caveolar targeting of EHD2 (Moren et al., 2012; Shah et al., 2014). Furthermore, by deleting the auto-inhibitory N-terminal sequence of EHD4, a supposedly active, open conformation was obtained (Melo et al., 2017).

3.4.2. Oligomerization and conformational change

EHD proteins form a stable dimer in solution through a conserved dimerization interface in the G-domain unique to the EHD family of proteins. This interface-1 forms independently of nucleotide binding. It involves helix α6 (see Figure 8B) from the opposing G-domains and contains the conserved residue Trp238, which is buried in a

hydrophobic pocket of the opposing molecule. Mutation of this residue render the protein insoluble (Daumke et al., 2007).

A recent cryo-EM structure of membrane-bound EHD4 oligomer (Melo et al., 2021) revealed two additional assembly interfaces in the EHD dimer. Interface-2 is formed between the helical domain of one protomer and the G-domain of the adjacent protomer along the filament: It involves the KPF-loop which moves into the hydrophobic pocket of the GTPase domain thereby creating a new assembly interface with the helical domain of the adjacent dimer. Interface-3 corresponds to the G-interface and is formed between the G-domains of the two adjacent dimers across the filament (Figure 9).

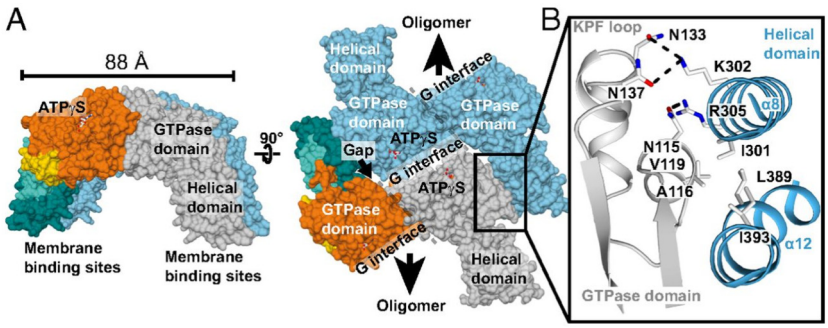

Figure 9: EHD oligomerization in N-terminal deleted EHD4 mouse construct. Oligomerization occurs via a new interface between KPF loop and the helical domain from the adjacent EHD molecule. (A) Two views of the EHD4 oligomer represented by the two dimers. One dimer is colored in blue whereas the other dimer is colored based on the molecules (first molecule: G-domain in orange, helical domain in blue, KPF loop in yellow and the second molecule in grey). The EH domains were not resolved in the crystal structure (B) Inset shows the details of the oligomerization surface involving the KPF loop and the helical domain of the opposing dimer. Figure taken from (Melo et al., 2017).

A comparison of the closed EHD2 (Daumke et al., 2007) and open EHD4 crystal structures (Melo et al., 2017) revealed a large-scale rotation of the helical domain around the conserved Pro289 (Melo et al., 2017). This rotation dislodges the linker from the EH domain, which was disordered in the open EHD4 crystal structure. It was therefore suggested that the released EH domain would be free to interact with binding partners having NPF motifs e.g. syndapins/PACSINs (Melo et al., 2017). However, in

the recent cryo-EM structure (Melo et al., 2021), the EH domain was still found on top of the G-domain, but appeared to be shifted towards the periphery of the filament.

3.4.3. ATPase activity

EHDs bind to the membrane and oligomerizes into ring-like structures and tubulate liposomes *in vitro* (Daumke et al., 2007; Melo et al., 2017; Moren et al., 2012; Shah et al., 2014). The oligomerization of EHD2 on membranes is ATP-dependent, which is likely due to the involvement of the G-interface that mediates ATP-dependent contacts (Melo et al., 2017). It was suggested that oligomerization leads to the reordering of residues in the switch regions (switch I and II), which stimulates ATPase activity 8-fold compared to the slow intrinsic ATPase activity in the absence of binding to the liposome (Daumke et al., 2007). Thus, mutations in residue from the switch region render EHD2 either deficient or slow in liposome-stimulated ATP hydrolysis (Daumke et al., 2007).

3.4.4. Cellular function of EHD proteins

Receptor internalization is a crucial step for many cellular processes, such as nutrient uptake, control of ion channels or the retrieval of synaptic vesicles (Naslavsky & Caplan, 2005). Some internalized receptors are destined for degradation, but a subset are returned to the plasma membrane by a process known as endocytic recycling where they can partake in additional rounds of internalization. During recycling, receptors are sorted at the early endosome (EE) and transported either directly to the plasma membrane (fast recycling), or through a transitory organelle (slow recycling) known as the endocytic recycling compartment (ERC) (see Figure 1) (Grant & Donaldson, 2009; Naslavsky & Caplan, 2011).

The four mammalian EHDs have been shown to regulate specific endocytic pathways including internalization and recycling of receptors (see Figure 1). EHD proteins with its C-terminus EH domain binds to proteins containing NPF motifs, such as the divalent rab4/5 effector rabenosyn 5, the cell fate determinant Numb, EH-binding protein 1 (EHBP1) and PACSIN2 and 1. (Naslavsky & Caplan, 2005, 2011).

Initially, a role of RME-1 (receptor-mediated endocytosis, EH domain containing protein in *C. elegans*) in regulating the recycling of the transferrin receptor from the

endocytic compartment to the plasma membrane was identified (Lin et al., 2001). Later on, mammalian EHD1 was also shown to be involved in the recycling of many other receptors, such as major histocompatibility complex (MHC) class I proteins (Caplan et al., 2002), β1 integrins (Jović et al., 2007) and cystic fibrosis transmembrane conductance regulator (Picciano et al., 2003), the insulin-regulated GLUT4 glucose transporter (Guilherme et al., 2004) and AMPA type glutamate receptor (Park et al., 2004). EHD1 also regulates the internalization of low density lipoprotein (LDL) (Naslavsky et al., 2007). Furthermore, EHD1 acts as a gatekeeper to promote ERC to plasma membrane recycling of multiple receptors. In addition, it also has specialized endocytic functions for selected receptors in specialized cells such as neurons (Naslavsky & Caplan, 2011; Yap. et al., 2010).

EHD2 localizes to caveolar neck and supposedly forms a ring around it, thereby maintaining caveolae stability and regulating cellular fatty acid uptake (Matthaeus et al., 2020; Moren et al., 2012). It also functions in myogenesis and muscle repair (Marg et al., 2012) and may be involved in myoblast fusion (Doherty et al., 2008). EHD2 was described to interact with actin-binding protein EHBP1 (EH-domain-binding protein 1), and this complex has been linked to the internalization of cell surface receptors such as transferrin and GLUT4, potentially linking clathrin-dependent endocytosis to actin filament (Guilherme. et al., 2004).

EHD3 depletion in Hela cells resulted in impaired transport during endocytic recycling, with receptor accumulating in peripheral EE and in failing to reach the perinuclear ERC region (Naslavsky et al., 2006). It has been implicated in stabilizing tubular recycling endosomes (TRE) (Bahl et al., 2016).

EHD4 also known as Pincher was identified in neuronal cells as a chaperone involved in the internalization of TrkA and TrkB nerve growth receptor factors (Shao et al., 2002; Valdez et al., 2005) and an active fragment of Nogo-A, a highly potent inhibitor of axonal growth (Joset et al., 2010). EHD4 localizes to a subset of EEs and has been implicated in the regulation of receptor transport from EEs to the ERC, as well as from EEs to the lysosomal degradation pathway (George et al., 2007; Sharma et al., 2008). EHD4 also interacts with the adaptor protein NUMB, which is responsible for the cell fate specification of *Drosophila* cells in the nervous system (Naslavsky & Caplan, 2011; Smith et al., 2004).

The focus in this study has been on regulating EHD2 functional activity. The subsequent section further elucidates the physiological function of EHD2 in caveolae.

3.5. Functional role of EHD2 at caveolae

A mass spectrometry-based screening had suggested that endogenous EHD2 is associated with caveolae (Aboulaich et al., 2004). Later on, co-localization and immunoprecipitation studies showed that EHD2 specifically binds and localizes to the surface of caveolae (Ludwig et al., 2013; Moren et al., 2012; Stoeber et al., 2012). Concomitantly, EHD2 is highly expressed in lungs and adipose tissues which have abundant caveolae (Moren et al., 2012).

Nucleotide binding is required for EHD2 caveolar localization, and ATP-dependent oligomerization is required to stabilize caveolae (Matthaeus et al., 2020; Moren et al., 2012). Mutational studies have shown that nucleotide binding is also required for oligomerization *in vivo*, as a nucleotide-binding deficient mutant showed a cytoplasmic distribution (Daumke et al., 2007). Caveolae surface association was decreased and an increase in mobility was observed in various cell lines when EHD2 was absent or down regulated. In contrast, EHD2 overexpression led to stabilization of caveolae at the plasma membrane (Matthaeus et al., 2020; Mohan et al., 2015; Moren et al., 2012; Shvets et al., 2015; Stoeber et al., 2012). Immuno-electron microscopy studies have shown that EHD2 is found at the caveolar neck (Ludwig. et al., 2013). In addition, EHD2 assembles in an ATP dependent fashion around membranes into ring-like oligomers with a diameter of 20 nm to 80 nm, indicating that it could form a ring around the caveolar neck (Daumke et al., 2007; Matthaeus & Taraska, 2021). All these data led to the hypothesis that EHD2 forms a ring at the caveolar neck to stabilize caveolae at the plasma membrane.

Caveolae have been implicated in cellular fatty acid uptake (Pilch & Liu, 2011). Previous studies have shown that the fatty acid translocase (FAT/CD36) is also involved in caveolae-dependent fatty acid uptake (Aboulaich et al., 2004; Eyre et al., 2007; Ring et al., 2006). CD36 was found partially co-localized with Cav-1 indicating its presence in caveolae (Matthaeus et al., 2020). However, CD36 was also observed

in non-caveolar plasma membrane domains (Matthaeus et al., 2020). Cell-based studies have shown that CD36 along with caveolae plays a role in EHD2-dependent lipid uptake pathway (Matthaeus et al., 2020).

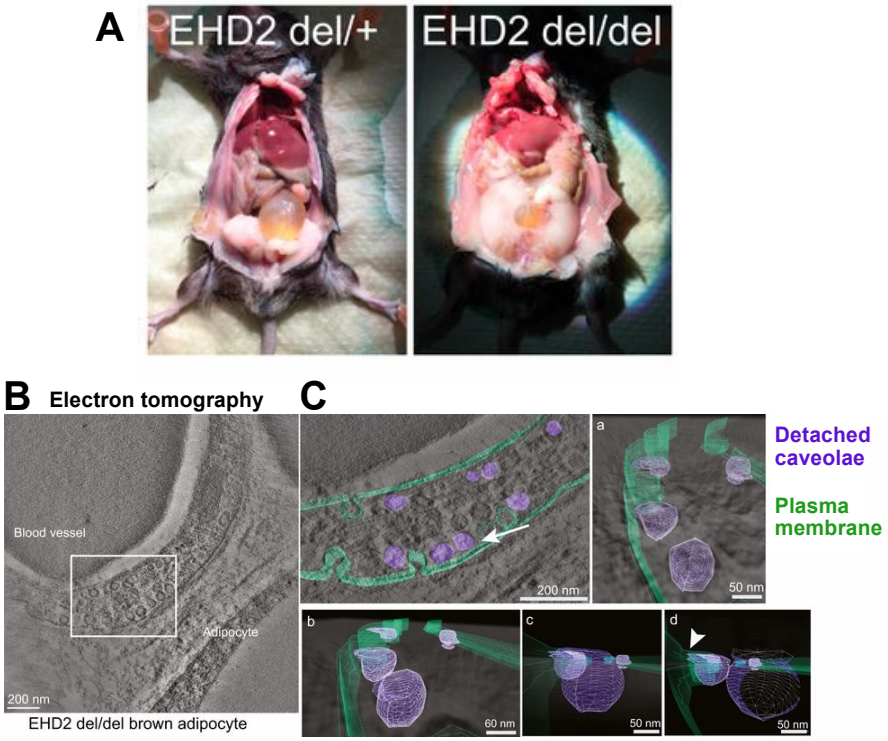

Figure 10: Physiological implication of EHD2 KO. (A) Increase fat tissue deposition around the organs in EHD2 KO mice compared to the control. (B) White box indicates the segment of EHD2 KO mice brown adipocyte (BAT), which was visualized by electron tomograms (ET) in C. (C) 3D model of ET showing detached caveolae from the plasma membrane in EHD2 KO BAT. Panel a-d, shows detached caveolae at different viewing angles (marked by white arrow) (Matthaeus et al., 2020).

The generation of an EHD2 KO mouse model helped in understanding the role of EHD2 at caveolae *in vivo* (Matthaeus et al., 2020). Experiments on EHD2 KO mouse model suggests that EHD2 acts as a negative regulator of caveolae-dependent lipid uptake. These KO mice showed an increased fat tissue deposition around the organs (see Figure 10A). Furthermore, an increase in fatty acid uptake in EHD2 KO adipocytes cells was observed in cellular assays and also in mouse embryonic fibroblasts (Matthaeus et al., 2020). Similarly, increased lipid droplet size was shown earlier in hepatocytes lacking EHD2 (Li et al., 2016). ATPase mutant expressed in EHD2 KO MEFs failed to rescue the large lipid droplets (Matthaeus et al., 2020).

Electron microscopy and electron tomography (Figure 10B and C) studies have shown that EHD2 KO mice harbor an increased number of detached caveolae in brown and white adipocyte cells compared to heterozygous controls (Matthaeus et al., 2020). Additional to the role of cellular fatty acid uptake, it was also shown that EHD2 KO results in reduced calcium entry, lack of activated eNOS and NO generation in endothelial cells. This leads to the reduced endurance in running wheel efficiency in mice and reduced blood vessel relaxation (Matthaeus et al., 2019).

Considering these *in vivo* data, it can be argued that ATP-dependent EHD2 oligomerization around the neck of caveolae is essential for regulating caveolae's physiological functions.

3.6. EHDs role in human disease

Marked advances have been made in understanding the functions of EHD proteins at the cellular level. EHDs regulate biological pathways by coordinating with other EH-domain binding proteins. This interaction network is involved in cellular functions as diverse as endocytosis, nucleo-cytosolic export and in cell proliferation (Santolini et al., 1999). Conditions resulting from dysregulation of EHD function are summarized in the following table.

Table 1: Relationship of EHD proteins to human disease. Modified from (Naslavsky & Caplan, 2011).

EHD protein	Disease or condition	Phenotype	Reference
EHD1	Pseudoexfoliation glaucoma	enhanced level of serum antibodies	(Dervan et al., 2010)
EHD1	*Apergillus fumigatus* infection	enhanced EHD1 expression in monocytes	(Cortez et al., 2006)

EHD protein	Disease or condition	Phenotype	Reference
EHD1	Metastatic ability of well-differentiated pancreatic endocrine neoplasms	decreased expression	(Hansel et al., 2004)
EHD1	Sickle cell disease	decreased expression	(Ammann & Goodman, 2009)
EHD1	*Aeromonas hydrophila* cytotoxic enterotoxin induced-gene	increased expression in macrophages	(Galindo et al., 2003)
EHD1	*Plasmodium falciparum* infected erythrocytes	increased expression in erythrocytes	(Tripathi et al., 2009)
EHD1	Prostate cancer	secreted from exosomes of prostate cancer cells	(Jansen et al., 2009)
EHD1	Cutaneous T cell lymphoma	increased expression in lesion	(Shin et al., 2007)
EHD1-4	Glioma	gene loss proposed	(Maher et al., 2001)
EHD2	Diabetes mellitus-associated bladder dysfunction	Decreased EHD2 expression	(Yohannes et al., 2008)
EHD2	Primary pigmented nodular adrenocortical disease	increased EHD2 expression	(Horvath et al., 2006)
EHD2	Increased fat tissue deposition around organ in mice	loss of EHD2	(Matthaeus et al., 2020)

EHD protein	Disease or condition	Phenotype	Reference
EHD3	Oral squamous cell carcinoma	decreased EHD3 expression	(Chen et al., 2008)
EHD3	Small-cell lung cancer	increased EHD3 expression	(Taniwaki et al., 2006)
EHD3	Acute myeloid leukemia	gene methylation	(Desmond et al., 2007)
EHD4	Systemic onset juvenile idiopathic arthritis	increased EHD4 expression	(Allantaz et al., 2007)

Dysregulation of EHD functional activity has been implicated in various human diseases. Therefore, finding chemical compounds that could regulate and restore EHD function could be of potential therapeutic importance.

3.7. Objective of this study

EHDs were described to function in endocytosis, neurotransmission, actin polymerization and cell proliferation. EHD2 in particular localizes to caveolae and regulates the uptake of lipids via caveolae, while EHD4 is located on early endosomes and mediates the trafficking of neuronal receptors. The lack of small molecule inhibitors which acutely target individual EHD members has hampered progress in understanding the detailed cellular function of EHDs in the past and explore the membrane trafficking pathways they are involved in. Furthermore, dysregulation of EHD function is implicated in various diseases, including cancer, sickle cell disease and juvenile idiopathic arthritis. Small molecules that interfere with or restore EHD functions could therefore be beneficial to ameliorate disease in the affected patients.

In my dissertation, I therefore aimed to identify chemical modulators that affect the activity of EHD4 and EHD2. To this end, I optimized an enzymatic ATPase assay to make it compatible for high throughput drug screening in the presence of liposomes. I then targeted the liposome-stimulated ATPase activity of EHD4 and EHD2. After extensive validation of the identified compounds and analyzing their specificity, I aimed to characterize their role in regulating cellular lipid uptake.

4. Materials and Methods

4.1. Materials

4.1.1. Instruments

Instruments	Manufacturer
Agarose Gel Electrophoresis System	Biometra Göttingen, DE
Äkta FPLC	GE Healthcare Life Sciences, Chicago, IL, USA
Äkta Prime Plus	GE Healthcare Life Sciences, Chicago, IL, USA
Äkta Purifier	GE Healthcare Life Sciences, Chicago, IL, USA
Amicon centrifugal filter devices	Millipore, Billersica, USA
Binocular Microscope MZ 7.5	Leica, Wetzlar, D
Benchtop Centrifuge 5415 D	Eppendorf, Hamburg, DE
Benchtop Centrifuge 5415 R	Thermofisher Scientific, Dreiech, DE
Benchtop Centrifuge 5804 R	Eppendorf, Hamburg, DE
Thermal shift assay	Bio-Rad CFX96 Real Time PCR
Cell culture flasks	Sarstedt, DE
C1000 Touch™ Thermal Cycler	Bio-Rad Laboratories, Inc., Hercules, CA, USA
CFX96 Touch Real-Time PCR	Bio-Rad Laboratories, Inc., Hercules, CA, USA
Cell counting chamber	LUNA-FL™
Centrifuge Avanti J-26 XP	Pneumatic Microfluidics, Newton, USA
Chromotography column Ni Sepharose HP	GE Healthcare, Piscataway, USA
Chromotography column Superdex 200 16/60,10/300 and 26/600	GE Healthcare, Piscataway, USA
Desiccator DURAN®	DWK Life Sciences (Wertheim,DE)

Instruments	Manufacturer
Fluidizer M-110L	Microfluidics, Newton, MA, USA
Heracell 150 cell culture incubator	GE Healthcare, Piscataway, USA
HPLC Infinity	Ismatec, Glattbrug, CH
ImageQuant™ LAS 4000 imaging system	GE Healthcare Life Sciences, Chicago, IL, USA
Pipetting robot for screening	Freedom EVO, Tecan
Plate reader for screening	Perkin Elmer
Peristaltic Pump Reglo Analog ISM827B	GE Healthcare, Piscataway, USA
pH-Meter	Mettler-Toledo, Gießen, DE
Photometer NanoDrop 2000	Agilent Technologies, Santa Clara, USA
PowerPac™ 300 Basic Power Supply	Bio-Rad Laboratories, Inc., Hercules, CA, USA
mircoflex™ LRF MALDI-TOF MS MSP 96 target ground steel BC plate	Bruker Corporation, Billerica, MA, USA
NanoDrop 2000 Spectrophotometer	Thermo Fisher Scientific Inc., Waltham, MA, USA
Reversed-phase ODS-2 Hypersil HLPC column	Thermo Fisher Scientific, Dreiech, DE
RALS Viscotec RImax	Malvern, Malvern, UK
Rotavapor	Rotavapor® R-300, I-300 and B-300, Buchi, DE
Scales	Sartorius, Göttingen, DE
SDS PAGE System Xcell sure Lock	Sartorius, Göttingen, DE
Shaker incubator Innova44	New Brunswick Scientific, Edison, USA
Ultracentrifuge Optima L-100K	Beckman Coulter, Krefeld, DE
Ultracentrifuge Optima TLX	Beckman Coulter, Krefeld, DE
Infinite® M1000 Pro Microplate reader	Tecan Group Ltd., Männedorf, Switzerland
ZEISS LSM 700 Confocal Laser Scanning Microscope	Carl Zeiss, Oberkochen, DE

4.1.2. Chemicals

Chemicals	Manufacturer
Acetic acid, 100%	Carl Roth GmbH + Co. KG, Karlsruhe, Germany
4-(2-Aminoethyl)-benzol-sulfonylfluorid (AEBSF) - Hydro-chlorid BioChemica	AppliChem GmbH, Darmstadt, Germany
Agar-Agar, Kobe I	Carl Roth GmbH + Co. KG, Karlsruhe, Germany
Agarose for DNA Electrophoresis	SERVA Electrophoresis GmbH, Heidel-berg, Germany
Ammonium molybdate (09878-25G)	Sigma-Aldrich, Inc. St. Louis, MO, USA
Ammonium chloride, ≥99.5 %	Sigma-Aldrich, Inc. St. Louis, MO, USA
Ammonium iodide, ≥99.0%, Honey-well™ Fluka™	Thermo Fisher Scientific, Waltham, MA, USA
BODIPY (D3922)	Molecular Probes
Brain Extract from bovine brain,Type I, Folch Fraction I (B1502)	Sigma-Aldrich, Inc. St. Louis, MO, USA
Boric acid, ≥99.8 %	Carl Roth GmbH + Co. KG, Karlsruhe, Germany
Bromophenol blue sodium salt, for electrophoresis	Carl Roth GmbH + Co. KG, Karlsruhe, Germany
Calcium chloride dihydrate, ≥99.5%	Sigma-Aldrich, Inc. St. Louis, MO, USA
Cobalt(II)-chloride hexahydrate, ≥99 %	Carl Roth GmbH + Co. KG, Karlsruhe, Germany
Chloroform (contains 100-200 ppm amylenes) (C2432-500ML)	Fischer Scientific
Coomassie® Brilliant Blue G 250	Carl Roth GmbH + Co. KG, Karlsruhe, Germany
Copper(II) sulfate pentahydrate, puriss.	Sigma-Aldrich, Inc. St. Louis, MO, USA
DOPS (synthetic liposomes) 840035C-500mg	Avanti Polar lipids

Chemicals	Manufacturer
DAPI (D9542)	Sigma-Aldrich, Inc. St. Louis, MO, USA
DMEM, high glucose, GlutaMAX Supplement, pyruvate-500mL	PAA laboratories, Pasching, A
1,4-Dithiothreitol (DTT), ≥99 %	Carl Roth GmbH + Co. KG, Karlsruhe, Germany
Dimethyl sulfoxide (DMSO)	New England Biolabs Inc., Ipswich, MA, USA
Ethylenediamine tetraacetic acid (EDTA) disodium salt dihydrate, ≥99 %	Carl Roth GmbH + Co. KG, Karlsruhe, Germany
Ethylene glycol, for analysis EMSURE®	Sigma-Aldrich, Inc. St. Louis, MO, USA
Formaldehyde, 16% (w/v), methanol-free, Pierce™	Thermo Fisher Scientific, Waltham, MA, USA
Fetal Bovine serum	PAA laboratories, Pasching, A
Glycerol, ≥99.5 % anhydrous	Carl Roth GmbH + Co. KG, Karlsruhe, Germany
Glycine, ≥99 %, for synthesis	Carl Roth GmbH + Co. KG, Karlsruhe, Germany
Guanidine hydrochloride, ≥99.5 %	Carl Roth GmbH + Co. KG, Karlsruhe, Germany
Insulin solution from bovine pancreas	Merck chemicals GMBH
Imidazole, PUFFERAN® ≥99 %	Carl Roth GmbH + Co. KG, Karlsruhe, Germany
Isopropyl-β-D-thiogalactopyranoside (IPTG), ≥99 %	Carl Roth GmbH + Co. KG, Karlsruhe, Germany
4-(2-hydroxyethyl)-1-piperazineethanesulfonic acid (HEPES), ≥99.5%	Carl Roth GmbH + Co. KG, Karlsruhe, Germany
Hydrochloric acid, 32%, extra pure	Carl Roth GmbH + Co. KG, Karlsruhe, Germany

Chemicals	Manufacturer
Kanamycin sulfate ≥750 I.U./mg, for biochemistry	Carl Roth GmbH + Co. KG, Karlsruhe, Germany
Malachite green (M9015)	Sigma-Aldrich, Inc. St. Louis, MO, USA
Magnesium sulfate, anhydrous	Merck KGaA, Darmstadt, Germany
Magnesium chloride, hexahydrate, ≥99.0%	Sigma-Aldrich, Inc. St. Louis, MO, USA
Manganese(II) chloride, tetrahydrate, ≥99.0%	Sigma-Aldrich, Inc. St. Louis, MO, USA
2-Mercaptoethanol, ≥99.0%	Carl Roth GmbH + Co. KG, Karlsruhe, Germany
Methanol, ≥ 99.8 %	Th. Geyer GmbH & Co. KG, Renningen, Germany
Oleic acid (cell culture grade)	Sigma-Aldrich, Inc. St. Louis, MO, USA
Potassium dihydrogen phosphate, ≥99 %	Carl Roth GmbH + Co. KG, Karlsruhe, Germany
RESAZURIN SODIUM SALT	Merck chemicals GMBH
Silver nitrate solution 5% (w/v)	Carl Roth GmbH + Co. KG, Karlsruhe, Germany
Skim milk powder	Sigma-Aldrich, Inc. St. Louis, MO, USA
Sodium carbonate, anhydrous, ≥98 %	Carl Roth GmbH + Co. KG, Karlsruhe, Germany
Sodium chloride, ≥99.8 %	Carl Roth GmbH + Co. KG, Karlsruhe, Germany
Sodium hydroxide, ≥98 %	Carl Roth GmbH + Co. KG, Karlsruhe, Germany
Sodium phosphate monobasic dihydrate, ≥99 %	Carl Roth GmbH + Co. KG, Karlsruhe, Germany
Sodium phosphate dibasic, ≥99 %	Carl Roth GmbH + Co. KG, Karlsruhe, Germany
Terrific broth, modified	Melford Laboratories Ltd., Chelsworth, UK

Chemicals	Manufacturer
Trypsin-EDTA (0.25%), phenol red-100 mL	PAA laboratories, Pasching, A
Trifluoroacetic acid (TFA), ≥99 %	Sigma-Aldrich, Inc. St. Louis, MO, USA
Tris-(hydroxymethyl)-aminomethan (TRIS), ≥99.9 %	Carl Roth GmbH + Co. KG, Karlsruhe, Germany
Tween® 20, Ph. Eur.	Carl Roth GmbH + Co. KG, Karlsruhe, Germany
Zinc sulfate, heptahydrate, ≥99.5 %	Carl Roth GmbH + Co. KG, Karlsruhe, Germany

4.1.3. Kits and consumables

Specified items	Manufacturer
Cell culture plates (24wells)	Sarstedt, DE
Cell culture plates (96wells)	Sarstedt, DE
ADP-Glo™ Kinase Assay, 1000 assays	Promega GmbH
D-Tube™ Dialyzer Midi, MWCO 6-8 kDa	Sigma-Aldrich, Inc. St. Louis, MO, USA
Extruder (mini)	Sigma-Aldrich, Inc. St. Louis, MO, USA
FILTER SUPPORT 10MM (100/PK)	Merck chemicals GMBH
Imaging chamber (µ-Slide 8 well high) (80806)	ibidi - cells in focus, GMBH
innuPREP Plasmid Mini Kit 2.0	Analytik Jena AG, Jena, Germany
Monarch® PCR & DNA Cleanup Kit	New England Biolabs Inc., Ipswich, MA, USA
QIAquick gel extraction kit	Qiagen, Hilden, DE
Whatman™ ME24 ST Sterile Cellulose Ester Membrane Filter, Pore Size: 0.2 µm, d= 4.7 cm	GE Healthcare Life Sciences, Chicago, IL, USA
96 Well plates (781186)	Greiner Bio-One International GmbH, Kremsmünster, Austria
NuPAGE™ 4-12% Bis-Tris Protein Gel NuPAGE™ 12% Bis-Tris Protein Gel NuPAGE™ MES SDS Running Buffer (20X) NuPAGE™ MOPS SDS Running Buffer (20X)	Thermo Fisher Scientific Inc., Waltham, MA, USA
PageRuler™ Plus Prestained Protein Ladder (10 to 250 kDa)	Thermo Fisher Scientific Inc., Waltham, MA, USA
Unstained Protein Molecular Weight Marker (14.4 to 116 kDa)	Thermo Fisher Scientific Inc., Waltham, MA, USA

Specified items	Manufacturer
GSTrap™ HP Column	Thermo Fisher Scientific Inc., Waltham, MA, USA
Ni Sepharose High Performance	GE Healthcare Life Sciences, Chicago, IL, USA
Amicon® Ultra-15 Centrifugal Filter Unit (50 kDa MWCO)	Merck KGaA, Darmstadt, Germany
Amersham™ Protran™ 0.45 µm nitrocellulose membrane	GE Healthcare Life Sciences, Chicago, IL, USA
Extra Thick Blot Filter Paper, Precut, 14 x 16 cm	Bio-Rad Laboratories, Inc., Hercules, CA, USA
Protein Thermal Shift Dye Kit-2,000 reactions	Thermo Fisher Scientific Inc., Waltham, MA, USA
ProteoMass™ Peptide and Protein MALDI-MS Calibration Kit	Sigma-Aldrich, Inc. St. Louis, MO, USA
40ML EPA screw vials (548-0156)	VWR International, DE
Screw cap, N-24 closed (218-1146)	VWR International, DE
X100 CLR screw cap flat (11999197)	Fischer Scientific
Syringes	Hamilton, USA

4.1.4. Buffers

Buffers	Composition
Resuspension buffer	50 mM Hepes (pH 7.5), 500 mM NaCl, 25 mM Imidazole, 2.5 mM β-mercaptoethanol, 2 mM $MgCl_2$
Equilibration buffer	50 mM Hepes (pH 7.5), 500 mM NaCl, 25 mM Imidazole, 2.5 mM β-mercaptoethanol, 2 mM $MgCl_2$
Wash buffer	50 mM Hepes (pH 7.5), 700 mM NaCl, 30 mM Imidazole, 2.5 mM β-mercaptoethanol, 1 mM ATP, 10 mM KCl
Elution buffer I	50 mM Hepes (pH 7.5), 500 mM NaCl, 300 mM Imidazole, 2.5 mM β-mercaptoethanol
Elution buffer II	50 mM Hepes (pH 7.5), 500 mM NaCl, 40 mM Imidazole, 2.5 mM β-mercaptoethanol,
Dialysis buffer	20 mM Hepes (pH 7.5), 500 mM NaCl, 2.5 mM β-mercaptoethanol, 2 mM $MgCl_2$
SEC buffer	20 mM Hepes (pH 7.5), 500 mM NaCl, 2.5 mM β-mercaptoethanol, 2 mM $MgCl_2$
Liposome buffer	20 mM Hepes (pH 7.5), 300 mM NaCl
HPLC buffer	100 mM potassium phosphate buffer (pH 6.5), 10 mM tetrabutylammonium bromide, 7.5% acetonitrile
EM buffer	10 mM Hepes (pH 7.5), 150 mM NaCl, 2.5 mM DTT, 1 mM $MgCl_2$
ATPase assay buffer or Assay buffer	20 mM Hepes (pH 7.5), 150 mM KCl, 0.5 mM $MgCl_2$

4.1.5. Media and antibiotics

Media/antibiotic	Manufacturer
Terrific broth	Roth, Karlsruhe, D
Luria broth	10 g/l tryptone/peptone, 10 g/l NaCl, 5 g/l yeast extract, pH 7 (NaOH) for LB Agar plates: mix LB medium and 15 g/l agar agar
DMEM	Gibco/Thermofisher Scientific, Dreiech, DE
DPBS	Gibco/Thermofisher Scientific, Dreiech, DE
Ampicillin	100 mg/ml in ddH_2O, working solution 100 µg/ml
Carbenicillin	100 mg/ml in ddH_2O, working solution 100 µg/ml
Kanamycin	100 mg/ml in ddH_2O, working solution 100 µg/ml

4.1.6. Enzymes

Enzymes	Manufacturer
Taq DNA polymerase with Thermo-Pol® Buffer	New England Biolabs Inc., Ipswich, MA, USA
Phusion® High-Fidelity DNA polymerase (2000 U/mL) with Phusion® HF Buffer	New England Biolabs Inc., Ipswich, MA, USA
CIP (Alkaline Phosphatase)	New England Biolabs Inc., Ipswich, MA, USA
Shrimp alkaline phosphatase (rSAP)	New England Biolabs Inc., Ipswich, MA, USA
T4 DNA Ligase with T4 DNA ligase Buffer	New England Biolabs Inc., Ipswich, MA, USA
Restriction Enzymes: BamHI-HF, MfeI-HF, NdeI, NotI, PvuI-HF, XhoI,	New England Biolabs Inc., Ipswich, MA, USA
PreScission protease for His-tag removal	Produced in-house
Benzonase® endonuclease, >90%, 25 U/µL	Merck KGaA, Darmstadt, Germany
DpnI	New England Biolabs Inc. (Ipswich, USA)
T4 Polynucleotide Kinase	New England Biolabs Inc. (Ipswich, USA)
Pfu DNA polymerase	Roboklon (Berlin, Germany)
DNase I, grade II, from bovine pancreas	Roche Diagnostics GmbH, Mannheim, Germany

4.1.7. Constructs

protein	boundaries	mutation	vector	comment
hsDrp1	fl (isoform-2, UniProtID: O00429-3, residues, 1-710)	wt	pSKB_LNB	(Frohlich et al., 2013)
	fl	A395D	pSKB_LNB	
	fl	R403C	pSKB_LNB	
	fl	G362D	pSKB_LNB	
mmEHD2	fl	wt	pSKB_LNB	(Daumke et al., 2007)
mmEHD2 ΔN	19-543	wt	pSKB_LNB	(Daumke et al., 2007)
mmEHD4	22-541	wt	pSKB_LNB	(Melo et al., 2017)

4.1.8. Softwares

Software	Manufacturer
flexAnalysis3.4 flexControl3.4	Bruker Corporation, Billerica, MA, USA
Rock maker	Formulatrix, Bedford, MA, USA
PyMOL, Version 2.3.1	Schrödinger, LLC.
ImageJ, Version 1.52a	(Schindelin et al., 2012; Schneider et al., 2012))
Graphpad Prism (version 7.05)	GraphPad Software, San Diego, California USA, www.graphpad.com
Coot/WinCoot, Version 0.8.9.1	(Emsley et al., 2010)

4.1.9. Cell lines

Wild type (WT) and EHD2 knockout MEFs (KO) have been used from (Matthaeus et al., 2020). For all experiments, MEFs between passage number 15-25 were used. For lipid droplet growth, MEFs were treated with 10 µg/ml insulin and 5 µM oleic acid diluted in serum-free DMEM.

4.1.10. Bacterial strains

Table 2: bacterial strains used

Bacterial strain	Source	Application
E.coli DH5α	Competent cells produced in-house (Novagen)	Molecular cloning
Giga cells	Competent cells produced in-house (Novagen)	Molecular cloning
E. coli BL21(DE3)	Competent cells produced in-house (gift from Stephen Marino)	Protein expression
E. coli Rosetta2(DE3)	Competent cells produced in-house (Novagen)	Protein expression

4.1.11. Plasmid

pSKB_LNB is a modified pET28a(+) vector carrying a Kanamycin resistance box (Novagen, Merck KGaA, Darmstadt, Germany). The modified expression cassette includes an N-terminal His_6-tag, an HRV-3C protease cleavage site and a multiple cloning site with recognition sequences for: *ApaI, NdeI, BamHI, EcoRI, SacI, SalI, HindIII, NotI, XhoI*. Modifications were introduced by D. Kühlmann, MPI Dortmund.

4.2. Methods

4.2.1. Molecular biology methods

4.2.1.1. Site-directed mutagenesis

To generate point mutations, KOD polymerase was used as per the manufacturer's instructions. Reaction mixture and PCR details are mentioned in Table 2.

Table 3: Master mix for quick mutagenesis change using KOD polymerase

Component	Volume	Final concentration
KOD-buffer	2.5 µl	1X
2 mM dNTPs	2.5 µl	0.25 mM
25 mM $MgSO_4$	1.5 µL	1.875 µM
5' primer (10 µM)	0.75 µL	0.375 µM
3' primer (10 µM)	0.75 µL	0.375 µM
DNA template	0.5 µL	(50-100 ng)/20 µl
KOD Polymerase	0.5 µL	
ddH2O	16 µL	

Table 4: Protocol for quick change mutagenesis using KOD polymerase

Process	Temperature	Time	Cycle(s)
Initialization	95 °C	5 min	1X
Denaturation	95 °C	20 s	
Annealing	55-68 °C	15 s	30X
Extension	68 °C	20 s/1000 bp	
Extension	68 °C	7 min	1X

PCR product was treated with *DpnI* at 37°C for 1 h.

4.2.1.2. Preparation of chemically competent *E. coli* cells

Chemically competent *E. coli* cells (Giga, DH5α, BL21(DE3) and Rosetta2(DE3)) cells were prepared for use in plasmid transformation. 100 mL of Lysogeny Broth medium

(LB) was inoculated with 1 mL of the overnight culture and grown at 37 °C and 250 rpm on a rotary shaker. After the cells reached an OD_{600} of 0.6 to 0.8, they were transferred into two 50 mL falcon tubes and incubated on ice for 10 min, followed by centrifugation for 10 min (2600 x *g* at 4 °C). The resultant pellet was resuspended in 5 ml ice cold 0.1 M $CaCl_2$,10% glycerol for 15 min on ice. Cells were centrifuged again as mentioned before. Pellet was resuspended in 1 ml of 0.1 M $CaCl_2$+10% glycerol. 50 µl of each aliquot were flash frozen in liquid nitrogen and stored in -80 °C.

4.2.1.3. Transformation

E.coli DH5α and Giga cells were transformed for plasmid propagation. For protein expression, transformation was done in *E. coli* Rosetta2(DE3) or *E. coli* BL21(DE3). 1 µl (50-100 ng) of the plasmid was mixed with 25 µl of chemically competent cells on ice and incubated for 5 min. A heat shock was applied at 42 °C for 30 s and the cells were quickly transferred to ice for another 5 min. 500 µl of LB medium was added and kept on a shaker at 37 °C for 1 h at 800 rpm. 60-100 µl of the LB media was plated on agar plate containing the required antibiotic. In case of site directed mutagenesis, cells were pelleted and resuspended in 25 µl of LB media. This entire reaction was applied to LB agar plates containing a specific antibiotic.

4.2.1.4. Isolation of plasmid DNA

Isolation of plasmid DNA was performed by using innuPREP plasmid mini Kit 2.0 (Analytik Jena GmbH) according to the manufacturer's protocol.

4.2.1.5. DNA sequencing

DNA sequencing was done by means of sanger sequencing at LGC Genomics GmbH (Berlin) or Source BioScience (Berlin). To analyze the results, DNA sequences were aligned using Clustal Omega (Sievers et al., 2011)

4.2.1.6. Bacterial storage and glycerol preparation

Bacteria were grown in LB media for around 8 h. 600 µl of this culture media was mixed with an equal amount of sterile 80% glycerol, frozen in liquid nitrogen and stored at -80 °C.

4.2.1.7. Constructs

The constructs used in this work have been listed in 4.1.7. All constructs were cloned in pSKB_LNB vector with an N-terminal HRV-3C protease cleavable His_6-tag.

4.2.2. Biochemical methods

4.2.2.1. Sequence alignment

To analyze sequence similarity and domain conservation, sequences were aligned with Clustal Omega (Sievers et al., 2011). For representation of alignments, the program GeneDoc was used (Nicholas, 1997).

4.2.2.2. SDS-PAGE

SDS-PAGE (Sodium dodecyl sulfate polyacrylamide gel electrophoresis) was used to separate and visualize the proteins depending on their molecular weight (M_W). Samples were prepared by mixing the respective proteins with 4X of sample buffer (50 mM Tris-HCl pH 6.8, 2% (w/v) SDS, 10% glycerol, 1% β-mercaptoethanol, 0.02% (w/v) bromophenol blue). Samples were then heat denatured at 95 °C for 5 min and loaded on the gel, which ran at 150 V until the dye front was close to the end of the gel. Staining was done using 0.3% (w/v) Coomassie Brilliant Blue R-250 (in 45% ethanol and 10% acetic acid). Gels were de-stained overnight in water and then imaged.

4.2.2.3. Protein expression

E. coli Rosetta2(DE3) or *E. coli* BL21(DE3) were used for protein expression. Approximately 30 µl from the glycerol stock was inoculated in a 500 ml flask containing 200 ml LB media with the respective antibiotics. This pre-culture was grown overnight at 37 °C at 800 rpm. On the next day, 25 ml of the preculture was inoculated in 2 L Terrific Broth medium (TB) containing the respective antibiotics. Cells were grown to an OD_{600} of 0.8 at 37 °C at 100 rpm. Cultures were cooled down by briefly transferring them to the cold room kept at 6 °C. Protein expression was induced at 18 °C by adding 100 µM isopropyl-ß-D-1-thiogalactopyranoside (IPTG). They were grown for another 20 h at 18 °C and 80 rpm. Cells were sedimented at 4 °C by centrifugation for 20 min at 5,000 g and resuspended in 30 ml of resuspension buffer (50 mM Hepes pH 7.5, 500 mM NaCl, 25 mM imidazole, 2.5 mM β-mercaptoethanol, 2 mM $MgCl_2$), transferred to a 50 ml Falcon tube and stored at -20 °C.

4.2.2.4. Protein purification

All protein purification steps were performed either on ice or at 4 °C. His_6-tagged proteins were purified using immobilized metal ion affinity chromatography (IMAC) and size-exclusion chromatography (SEC) at 4 °C. To avoid protein from precipitating, I used 500 mM NaCl in all the buffers throughout the purification.

Full length mouse EHD2 (EHD2), N-terminal deleted mouse EHD2 (EHD2ΔN), N-terminal deleted mouse EHD4(22-541) (EHD4) and human dynamin related protein-1 (Drp1) were cloned earlier (Daumke et al., 2007; Frohlich et al., 2013; Melo et al., 2017; Shah et al., 2014). His-tagged Human Rhinovirus (HRV) 3C protease was used to cleave the His_6 tag from all the proteins studied in this work.

Expression and purification protocol were similar for all the proteins. The cell suspension was thawed at room temperature. During this process, 1 µM DNase (Roche), 500 µM of the protease inhibitor 4-(2-aminoethyl)-benzolsulfonyfluorid hydrochloride (BioChemica) and 5 U/mL benzonase (Merck) were added. Cells were disrupted by passing them through a microfluidizer (Microfluidics) at least 3 times or when the suspension became less viscous. The lysed bacterial suspension was then centrifuged at 20,000 rpm for 30 min at 4 °C. The supernatant was collected and filtered using 0.45 µm filter packs, and then applied on a Ni^{2+}-sepharose column equilibrated with equilibration buffer. This was followed by a wash step (50 mM Hepes pH 7.5,

700 mM NaCl, 30 mM imidazole, 2.5 mM β-mercaptoethanol, 1 mM ATP, 10 mM KCl and 2 mM $MgCl_2$) and then shortly with equilibration buffer (50 mM Hepes pH 7.5, 500 mM NaCl, 25 mM imidazole, 2.5 mM β-mercaptoethanol, 2 mM $MgCl_2$). Protein was eluted with 20 mM Hepes pH 7.5, 500 mM NaCl, 300 mM imidazole, 2.5 mM β-mercaptoethanol and 2 mM MgCl2. The eluted protein was incubated with 1:150 (w/w) His-tagged Human Rhinovirus (HRV) 3C protease and dialyzed overnight in a 10 kDa cutoff membrane against dialysis buffer (20 mM Hepes pH 7.5, 500 mM NaCl, 2.5 mM β-mercaptoethanol and 2 mM $MgCl_2$). To remove the protease and His_6-tag, the cleaved protein was applied to a second Ni^{2+} column equilibrated with equilibration buffer. Protein was eluted with 20 mM Hepes pH 7.5, 500 mM NaCl, 2.5 mM β-mercaptoethanol, 40 mM imidazole and 2 mM $MgCl_2$ buffer. Cleaved protein was concentrated and loaded on Superdex 200 gelfiltration column (GE) equilibrated with size exclusion buffer (20 mM Hepes pH 7.5, 500 mM NaCl, 2.5 mM β-mercaptoethanol and 2 mM $MgCl_2$). Fractions were analyzed with SDS PAGE and those containing pure protein were pooled. This protein solution was then concentrated using 10 or 30 kDa Amicon® Ultra 15 mL Centrifugal Filters (Merck Millipore). Protein concentration was determined measuring absorbance at 280 nm with a NanoDrop One or NanoDrop 2000 spectrophotometer (Thermo Scientific). Protein parameters like molecular weights, extinction coefficients were calculated with ProtParam, ExPASy Server (Gasteiger et al., 2003). Aliquots (50 µl or less) were flash frozen in liquid nitrogen and stored at -80 °C.

To have protein uniformity while screening several drug libraries, I did a large scale protein purification from 30 liters of *E.coli* culture. All the steps mentioned in the method section and the details mentioned above were up-scaled by 4X times. A total of 6 injections, each containing a maximum of 50 mgs of protein was applied to S200 26/600 SEC column and instead of 1 ml, fraction size of 1.5 ml were collected.

4.2.2.5. Mass-spectrometry

His-tag cleavage was verified by mass spectrometry. The purified protein was diluted in 0.1% trifluoroacetic acid (TFA) to a final concentration of 10 µM and mixed with an equal volume of a saturated solution of α-cyano-4-hydroxycinnamic acid in 50% acetonitrile, 0.05% TFA. 0.5 µl of this mixture was spotted on a MALDI target plate. Measurements were done using a microflex™ LRF MALDI-TOF mass spectrometer

(Bruker) applying linear, positive ion mode. Data was analyzed using the supplied software from Bruker.

4.2.2.6. Liposome preparation

A lipid extract from bovine brain, Folch fraction type I, and synthetic phosphatidylserine, also known as DOPS [1,2-dioleoyl-sn-glycero-3-phospho-L-serine (sodium salt, 840035C)], were obtained from Sigma Aldrich and had the same stock concentration of 25 mg/ml in chloroform. For small scale applications, liposomes were prepared with the conventional method as described in 4.2.2.6.1 according to (McMahon Lab, Protocols). A large-scale preparation method is described in 4.2.2.6.2.

4.2.2.6.1. Conventional method (small scale)

All the glass vials were rinsed with chloroform and dried under the hood. 20 µl from the liposome stock was mixed with 200 µl of 3:1 (v/v) chloroform/methanol mixture in a glass vial. Lipids were dried under a gentle argon stream and stored overnight under vacuum in a desiccator. Dried lipids were hydrated for 5 min by adding 250 µl liposome buffer (20 mM Hepes pH 7.5, 300 mM NaCl) to reach a final concentration of 2 mg/ml and then resuspended by sonication in an ultrasonic water bath for 2 cycles of 30 s each. The freshly prepared liposomes were left for at least half an hour at room temperature before use.

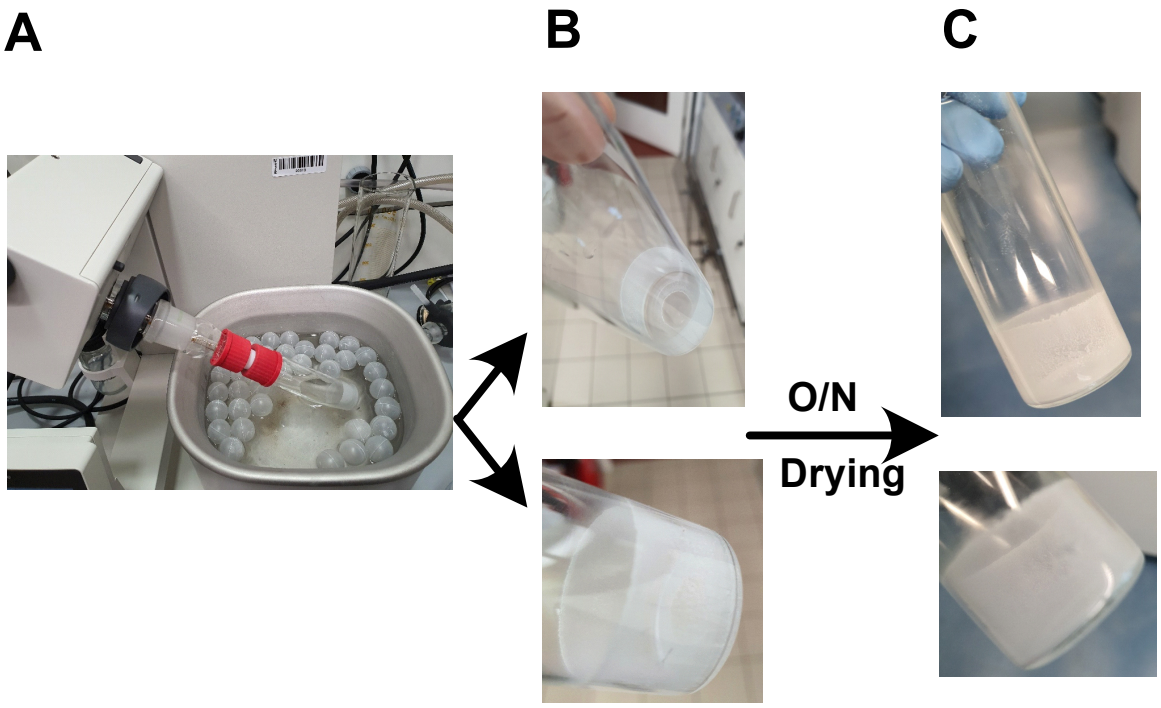

Figure 11: Schematic representation of mass scale liposome preparation. (A) Overview of the experimental setup. (B) Lipids sticking to the glass vial after removal of chloroform/methanol mixture using the Rota vapor (C) Same lipids after O/N drying. O/N- overnight.

4.2.2.6.2. Large scale preparation

A lipid monolayer was prepared with the help of a rotary evaporator (Rotavapor R-300, Buchi). Nitrogen gas instead of vacuum was used to remove the chloroform/methanol mix from the lipids. For this, the vacuum port was removed and a 50 ml serological pipette attached to a nitrogen gas tubing into the glass vial (VWR 548-0156). The process is depicted in Figure 11. 500 µl of DOPS (Avanti polar lipids) were mixed with 6 ml of the chloroform/methanol mixture (3:1 *v/v*) in the previously mentioned glass vial. This vial was attached to the rotavapor at no tilt with the bottom part of the vial dipping into heating bath kept at 25 °C (see Figure 11A). A gentle nitrogen stream was introduced into the vial and adapted by observing no ripples on the surface of the solution. The rotation was set to 175 rpm. Approximately 25 min later, lipid monolayer formation was observed (see Figure 11B). The vial was kept in a desiccator overnight for drying (see Figure 11C).

For rehydration of the lipids and formation of liposomes, 6.25 ml of liposome buffer (20 mM Hepes pH 7.5, 300 mM NaCl) was incubated for 5 min at room temperature. Vials were sonicated for two cycles (30 s each) in a water bath sonicator (Sonorex). This was followed by another incubation step of 30 min at room temperature. 5 ml aliquots were subjected to 5 cycles of freeze and thaw in liquid nitrogen. Finally, the aliquots were stored at -80 °C.

4.2.2.7. Liposome extrusion

Prior to usage, the liposomes were extruded with a mini-extruder (Avanti) using membranes of the required pore size. For extrusion, liposomes were passed 13 times through the mini-extruder.

4.2.2.8. Liposome co-sedimentation assay

5 µM or 10 µM protein was incubated with liposomes (concentration ranging from 300 µg/ml to 1 mg/ml) in a 50 µl reaction for 15 min at room temperature. Upon centrifugation at 200,000 rpm for 20 min at 20 °C, pellet and supernatant were separated and analyzed by SDS-PAGE.

4.2.2.9. Electron microscopy

To observe EHD2 oligomerization on membranes, tubulation assays were performed. 50 µM EHD2 was mixed with 2.25 mM ATP and 2 mg/ml Folch liposomes in EM buffer (10 mM Hepes pH 7.5, 150 mM NaCl, 2.5 mM DTT, 1 mM $MgCl_2$) and the reaction was incubated for 20 min at room temperature (typical sample size was 50 µL). Samples were stained with 2% uranyl acetate and spotted on carbon-coated copper grids. Grids were then imaged with a transmission electron microscope at 80 kV (Zeiss 910) and image acquisition was done with a CCD camera. The integrated imaging software from the TALOS microscope, TEM user interface, was used to collect and visualize the images.

4.2.3. Screening methods

4.2.3.1. Preparation of malachite green (MLG) dye

0.1% MLG dye (Sigma, M9015) was dissolved in 1 M HCl by vortexing. 1% ammonium molybdate (Sigma, 09878-25G) was added and vigorously vortexed until no visible precipitates were observed. The resulting solution was filtered through a 0.45 µm filter and stored in an aluminum foil-wrapped glass bottle in the dark. Every time a new dye was prepared, its absorption maxima was determined and a standard curve plotted.

4.2.3.2. Enzymatic assay

Enzymatic assays (ATPase or GTPase) were done in a 384 well plate. The assay buffer contained 20 mM Hepes, 150 mM KCl, 0.5 mM $MgCl_2$, pH 7.5. The reaction was quenched by the addition of the dye which denatures the protein. Turnover of substrate was limited to 10% for Michaelis-Menten constant determination (K_m) and was calculated by fitting initial velocities to a non-linear least fit squares to the Michaelis-Menten equation $\left(v0 = vmax[S]/(Km + [S])\right)$ using GraphPad Prism 7.05. ATPase assay and K_m determination were done in duplicates and triplicates, respectively.

4.2.3.2.1. EHD4 ATPase assay

The EHD4 ATPase assay were conducted at 25 °C. 30 µM of ATP was mixed 50 µg/ml with DOPS in assay buffer. Reaction was started by adding 200 nM EHD4. At any given time-point, 25 µl of the reaction was taken out and mixed with 75 µl of the dye in a 384 well plate. Absorbance at 650 nm was measured in a plate reader (Tecan, infinite M200).

4.2.3.2.2. EHD2 ATPase assay

EHD2 ATPase assays were conducted at 30 °C. 50 µM ATP and 500 µg/ml Folch liposomes were mixed in assay buffer. The reaction was started by adding 5 µM EHD2. At defined time points, reaction aliquots were diluted three times in reaction buffer (50 mM Tris and 150 mM NaCl pH 7.5) and quickly flash frozen in liquid nitrogen.

Samples were applied to an HPLC and nucleotides were separated with reversed phase column (C18 100 × 4.6 mm) equilibrated with running buffer containing 100 mM potassium phosphate buffer pH 6.5, 10 mM tetrabutylammonium bromide, 7.5% (vol/vol) acetonitrile. Adenine nucleotides were detected by absorption at 254 nm and quantified by integrating the corresponding nucleotide peaks and determining the ADP/ATP ratios.

4.2.3.2.3. Drp1 GTPase assay

Drp1 GTPase assays were conducted at 25 °C. 40 µM GTP and 200 µg/ml DOPS liposomes were mixed in assay buffer. Reactions were started by adding 300 nM Drp1. At defined time points, 25 µl of the reaction was taken out and mixed with 75 µl of the dye in a 384 well plate. Absorbance at 650 nm was measured in a plate reader (Tecan, Infinite M200).

Validation assays parameters for Drp1 were the same as its GTPase assay whereas the HPLC-based protocol was as described in section 4.2.3.22 except that guanine detection was done by measuring absorption at 259 nm.

4.2.3.3. Z-factor (Z´) determination

Z´ was determined as mentioned in (Zhang et al., 1999). ATPase assays for the target protein were done with 16 replicates. 1.5% DMSO was included to simulate screening conditions. The positive control was measured after an incubation time of 15 min (EHD4) and 20 min (Drp1).

4.2.3.4. High throughput screening (HTS)

Screening was done in the screening unit of the Leibniz Institute for Molecular Pharmacology (FMP) using the kinase drug library and the ‘diversity set’. 16,000 compounds were tested as singlets in 384 well plate format.

Master mix (MM) of ATP and DOPS and the protein dilution in assay buffer was prepared. 15 µl of the MM was pipetted with the help of multi-drop dispensing cassette. 0.2 µl of the compounds at a final concentration of 10 µM were pipetted from the drug

library plate using the Tecan-Evo workstation (pipetting robot). To remove any air bubble, the plates were centrifuged for 3 min at 1200 rpm.

10 µl of EHD4 was pipetted using multi-drop dispensing cassette. To have homogenous enzymatic activity, the plates were vortexed using a microplate mixer at 2000 rpm for 10 s. The plates were incubated for 15 min at room temperature and 75 µl of MLG dye with the cassette. The plates were measured in Perkin Elmer Envision plate reader.

Data was analyzed with an automated pipeline (Martin Neuenschwander) (Hinderlich et al., 2017) using Knime software (Berthold et al., 2009). Individual plates Z´ value and SNR was calculated. Compared to the control´s absorbance at 650 nm (Abs_{650}), compounds were classified as inhibitors (%Abs650 ≤ 25%) and activators (%Abs_{650} ≥ 25%), collectively known as hits. These hits at 10 mM were picked from the drug library in another 384 well plate. This plate was called as the hit plate and used further in validation and counter screening. The compounds from the hit plate were diluted 10 times in another plate to have a final 1 mM concentration. This served as the working hit plate and from here, 0.25 µl was pipetted in validation assay to have a final compound concentration of 10 µM.

Hits were validated in duplicates. The validated hits were then counter-screened to eliminate false positive and IC_{50} determined.

4.2.3.5. IC_{50} determination

IC_{50} values were determined in the same setup with varying inhibitor concentrations from 0.125 µM to 50 µM. The validated hits were picked up from the drug library into a different plate. Each plate had 32 compounds, pipetted in column 1 and 12 at a concentration of 10 mM and a volume of 5 µl. These plates serve as IC_{50} hit plate. For calculating IC_{50}, we prepared the working IC_{50} hit plate by serial dilution with the help of Tecan-Evo workstation. 5 µl DMSO was added in all the wells. Then from column 1 (5 mM) after mixing, 5 µl was taken and added to the adjacent wells in column 2 and mixed. This was repeated until column 11. In a similar manner from column 12 to column 22 serial dilution was done. Column 23 and 24 were for control and background respectively. From this plate, 0.25 µl was added in the assay for IC_{50} determination. For serial dilution and final concentrations, see Table 5. Data was processed and IC_{50}

determined in the same way as done in preliminary screening by the automated pipeline.

Table 5: compound dilutions in different columns of IC_{50} plate and their respective final concentration in the assay.

Column	IC_{50} hit plate (mM)	IC_{50} working hit plate (mM)	Assay concentration (µM)
1	5	5	50
2	5	2.5	25
3	5	1.25	12.5
4	5	0.625	6.25
5	5	0.3125	3.125
6	5	0.156	1.5625
7	5	0.08	0.8
8	5	0.04	0.4
9	5	0.02	0.2
10	5	0.01	0.1
11	5	0.005	0.05

4.2.3.6. Compound solubility

All the compounds came as lyophilized powder and were initially dissolved as 100 mM stocks in DMSO. If the compound was not soluble at 100 mM, gradually the concentration was reduced by adding more DMSO until no visible precipitate was seen after spin down. Like this, stock concentrations ranging from 5 mM to 100 mM were obtained. The final amount of DMSO in the assay plays an important role in compound solubility. All of the compounds are soluble in DMSO but they precipitate out when diluted because the final DMSO is very less. Similar observation were also noticed while doing ITC experiments. All the compounds required a minimum of 1% DMSO for their solubility in the solution.

4.2.3.7. Thermal shift assay (TSA)

TSA were done in a CFX96 touch-real time PCR using a fluorescent dye from ThermoFisher Scientific (catalogue number 4461146). Reactions were prepared on ice as mentioned in Table 6, to a final volume of 50 µl and transferred to a 96 well PCR plate and then sealed with a plastic film. CFX96 was precooled to 4 °C and the PCR plate was inserted. The fluorescence was measured from 4 °C to 80 °C with 0.5 °C

temperature steps. Protein melting temperatures were calculated with the provided software (Bio-Rad) and plotted as bar diagram using GraphPad Prism 7.05.

Table 6: Thermal shift assay sample preparation

Component	Final concentration
protein	5 µM
8x dye	1x
Inhibitor/substrate	50 µM
assay buffer	add to 50 µl

4.2.4. Cell biology methods

4.2.4.1. Cell culture

Mouse embryonic fibroblasts (MEFs) derived from C57 black six mice (C57BL/6) or backcrossed EHD2 KO mice (Matthaeus et al., 2020) were grown in DMEM with 10% fetal bovine serum (FBS) and 1% penicillin/streptomycin (P/S) in 5% CO_2 at 37 °C. Medium was changed every two days. Cells were kept in culture by splitting them when they reached 80% confluency. MEFs with a passage number from 15-25 were used for the experiments.

4.2.4.2. Cytotoxicity assay

This assay was done in a 96 well cell culture plate. A stock solution of 0.4 mM resazurin dye (Sigma Aldrich, R7017-5G, CAS number 62758-13-8) was prepared. 5 mg of the dye was dissolved in 50 ml of DPBS under constant heating and steering. It was filtered and stored in a Falcon tube wrapped in aluminum foil in the dark. The dye was pre-warmed before use.

5,000 MEFs per well were seeded in a 96 well plate and grown to 90% confluency along with the desired concentration (10 µM or 50 µM) of the inhibitor. Dye was added in a 1:10 (v/v) dilution and further incubated with the cell for several hours in such a way that the total incubation time was 24 h. Resultant fluorescence was measured in a plate reader (Tecan, Infinite M200, excitation: 570 nm and emission: 585 nm). 1%

Triton X-100 (*v/v*) was used as a positive control, whereas MEFs grown with DMSO and without any treatment were the negative control. The corresponding fluorescence was plotted as a bar diagram for the respective inhibitors and the cell lines using GraphPad Prism 7.05.

4.2.4.3. Lipid droplet assay

The lipid droplet assay was done in an imaging chamber (µ-Slide, 8 well high). 7,000 MEF cells per well were seeded and grown until 60-70% confluency. During this time, inhibitors were added for the required incubation time (either 20 h or 25 h). For lipid droplet (LD) growth, MEFs were supplemented with 10 µg/ml insulin and 5 µM oleic acid diluted in serum-free DMEM for 5 h. After incubation, cells were washed with PBS and fixed using 4% paraformaldehyde (PFA). Nucleus and lipid droplet (LD) staining was done using DAPI and BODIPY, respectively, diluted 1:1000 in 1X PBS after application for 10 min.

4.2.4.4. Microscopy

Cells were imaged in the MDC Advanced Light Microscopy facility (ALM). Zeiss LSM 700 confocal microscope with 10X (air) and 63X (oil) objectives was used. 12 to 15 images from each well and from different areas were collected to have a general overview. The obtained images were visualized by ZEN software (Zeiss) and later analyzed and processed by Fiji (Schindelin et al., 2012).

4.2.4.5. Lipid droplet (LD) area

Approximately 20-30 randomly chosen cells were processed by a semi-automated script (9.3. Appendix C) using Fiji (Schindelin et al., 2012). Individual LD area was determined for all LDs in a single cell. These areas were then summed up to obtain the total LD area per cell. Obtained values were plotted using Graph pad prism version 7.05. All experiments were done in quadruplets.

4.2.4.6. Statistical analysis

Statistical calculations were done using Graph pad prism version 7.05. Normality distribution test was done using D'Agostino-Pearson test. If the two sets of data were normally distributed, then unpaired t test (parametric) was applied else Mann-Whitney test (non-parametric). Mann-Whitney test was also applied in the case, if one data set was normally distributed whereas the other not. Differences of $p \leq 0.05$ were considered significant ($p \leq 0.05$*, $p \leq 0.01$**, $p \leq 0.001$***, $p \leq 0.0001$****).

5. Results

5.1. Development of an activity assay for EHD proteins

A plethora of available kinase assays is described in the literature to measure enzymatic kinase activity (Ma et al., 2008). Classical biochemical methods use the quantification of released inorganic phosphate, which is then converted into a detectable compound.

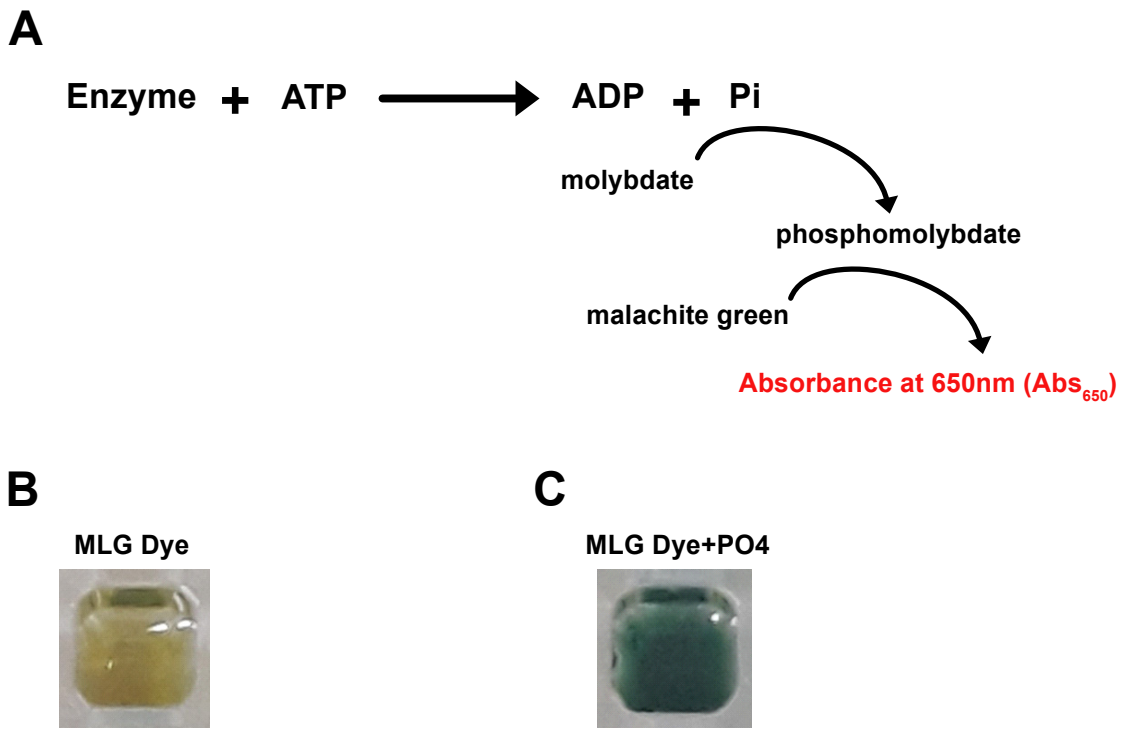

Figure 12: Malachite green assay. (A) Schematic representation of malachite green assay. (B) & (C) The dye changes color from yellow to green in the presence of orthophosphate.

.

For the high throughput screening, targeting the ATPase activity of EHD proteins, I chose the Malachite green assay (MLG) (Feng et al., 2011; Itaya & Ui, 1966). It is a simple, cost-efficient and non-radioactive approach of determining released inorganic phosphate from ATP hydrolysis. It does not include cumbersome washing or detection steps or radioactive waste problems. This assay is based on a green colorimetric complex formed between the yellow dye malachite green, molybdate and free orthophosphate, which shows absorption maxima around 650 nm (see Figure 12).

Various absorption maxima of the colorimetric complex have been reported, starting from 620 nm to 650 nm (Biswas et al., 2009; Feng et al., 2011; Itaya & Ui, 1966; Yang & Wang, 2016). The MLG dye that I prepared showed an absorption maxima between 640 nm and 650 nm (see Figure 13A). Orthophosphate detection was linear (R^2 = 0.9954) for increasing concentrations until 100 µM phosphate (see Figure 13B), while the lower detection limit was about 10 µM phosphate. The linearity of the standard curve guarantees accuracy of measurement to 1.5 absorption units at 650 nm (Au).

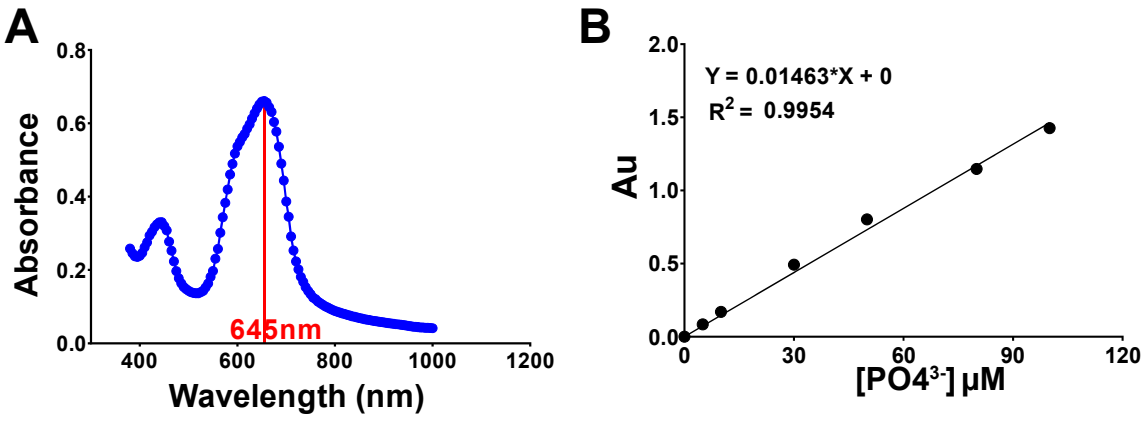

Figure 13: Malachite green assay parameters. (A) Absorption maxima of the colorimetric complex formed between the dye, molybdate and orthophosphate. (B) Standard curve of orthophosphate at dilutions 5, 10, 30, 50, 80 and 100 µM generated by the malachite green assay. Equation for the curve and coefficient of determination has been mentioned on the top left. Au (absorption unit) in B refers to absorption at 645 nm. Data points in B represent the mean of three independent experiments and the error bar signifies the standard deviation. When the standard deviation is smaller than the size of the data point, error bar is not displayed.

5.1.1. Interference from assay components

An important aspect to address before proceeding to the ATPase assay was the interference from assay components, which can lead to a high background noise. Checking the individual components in the assay led me to observe that no major background signal was observed for the buffer components, whereas Folch lipids showed a large contribution to the blank signal (see Figure 14). Therefore, the use of Folch lipids in the malachite green assay was excluded. In seek of alternatives,

phosphatidyl serine (PS) lipids which showed the least absorption was chosen for the assay development (see Figure 14A).

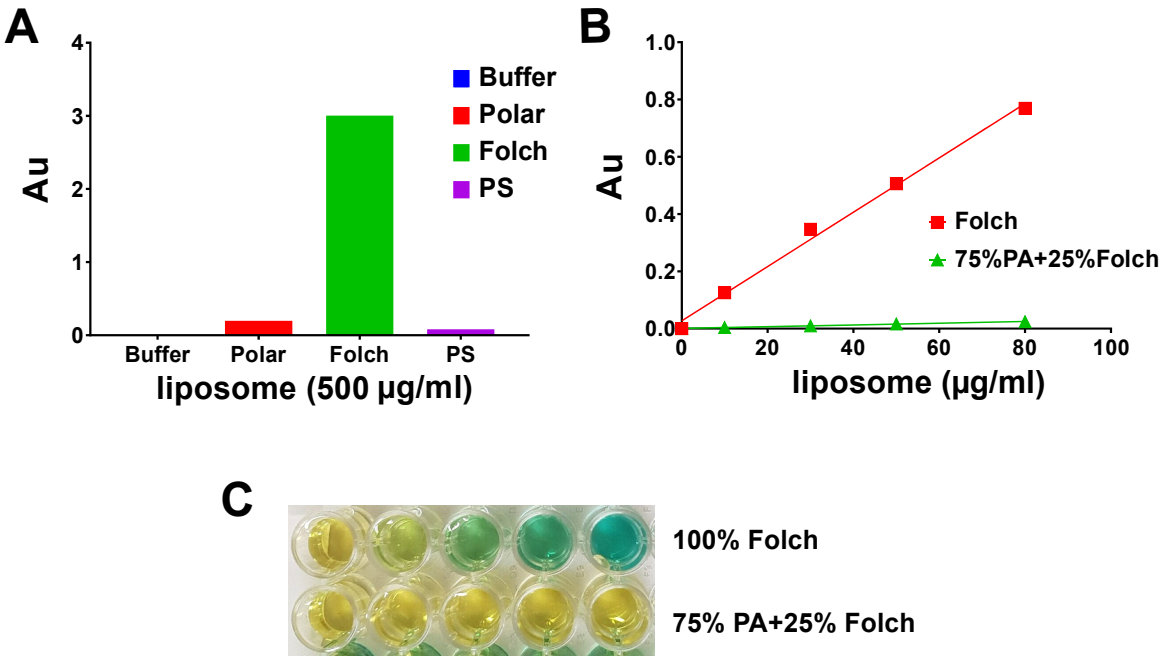

Figure 14: Interference of liposome in the assay. (A) Background signal from different kinds of liposome (Folch, PS and polar lipids) at 500 µg/ml. Folch liposomes showed an exceptionally high background signal. (B) Background signal is directly proportional to the concentration of the liposomes. (C) Visual representation of the graph in B. The color developed in case of increasing concentration of Folch liposome is so strong that it resembles an enzymatic reaction. The background signal visibly seen by color change is mostly due to Folch as substituting 75% phosphatidic acid in it results in drastically reduced background.

Similarly, ATP also led to an increase in background signal with increasing concentration (see Figure 15A). This could be attributed due to the phosphate impurities present in ATP. Furthermore, I observed that ATP was slowly hydrolyzed in the acidic environment of the MLG dye (see Figure 15B). This background hydrolysis was also directly proportional to the initial ATP concentration.

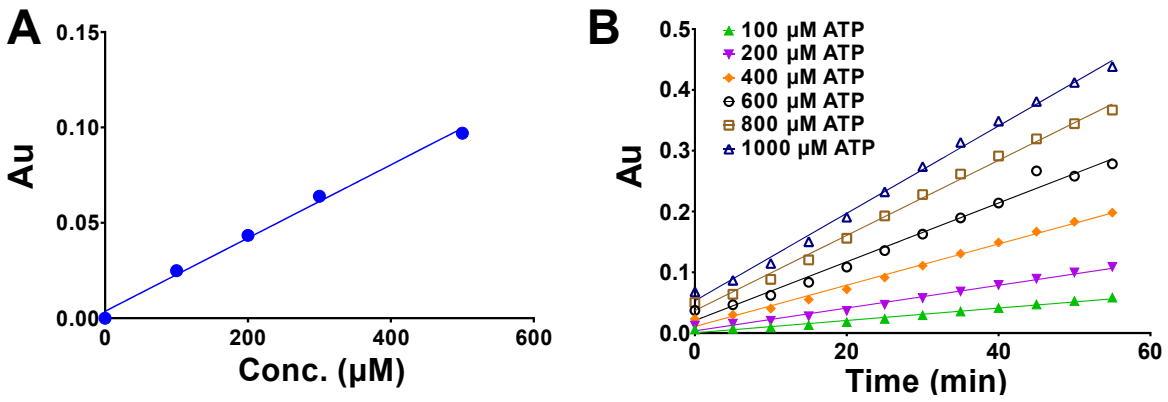

Figure 15: ATP interference in MLG assay. (A) Background signal from ATP is directly proportional to the ATP concentration in the assay. The background signal is possibly derived from the phosphate contaminants present in the ATP. (B) ATP hydrolyses in the acidic environment of the MLG dye. The higher initial concentration of ATP the more was the background signal during the elapsed time.

The amount of ATP used in the assay was decided based on the Michaelis-Menten constant (K_m). To keep the possibility of finding all types of inhibitors (competitive, non-competitive and un-competitive), I kept the substrate concentration close to the K_m (see 6.1.3).

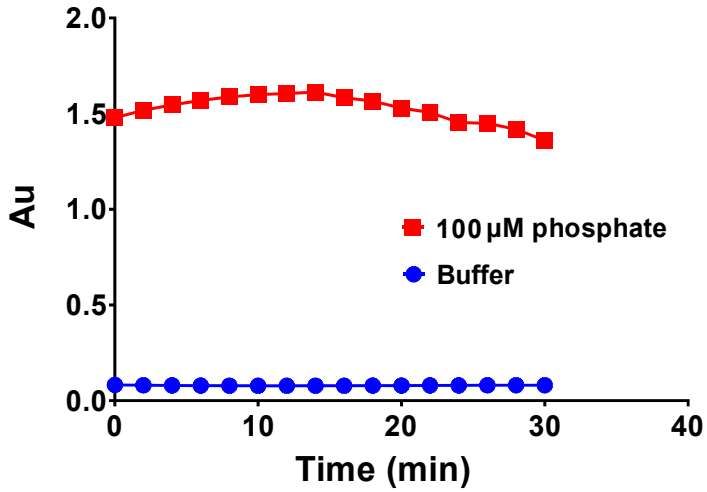

Figure 16: Colorimetric complex stability. The colorimetric complex formed between molybdate, 100 µM phosphate and MLG dye formed instantly and remained stable over 30 min. The buffer control showed no relevant signal.

The green color colorimetric complex formed instantly and remained stable over a period of 30 min (see Figure 16). Though, at lower concentrations of ATP, the background signal due to ATP hydrolysis was greatly reduced (see Figure 15B) but to still avoid any false reading, I took the measurement instantly after the addition of MLG dye.

5.1.2. Optimizing protein expression and large-scale purification

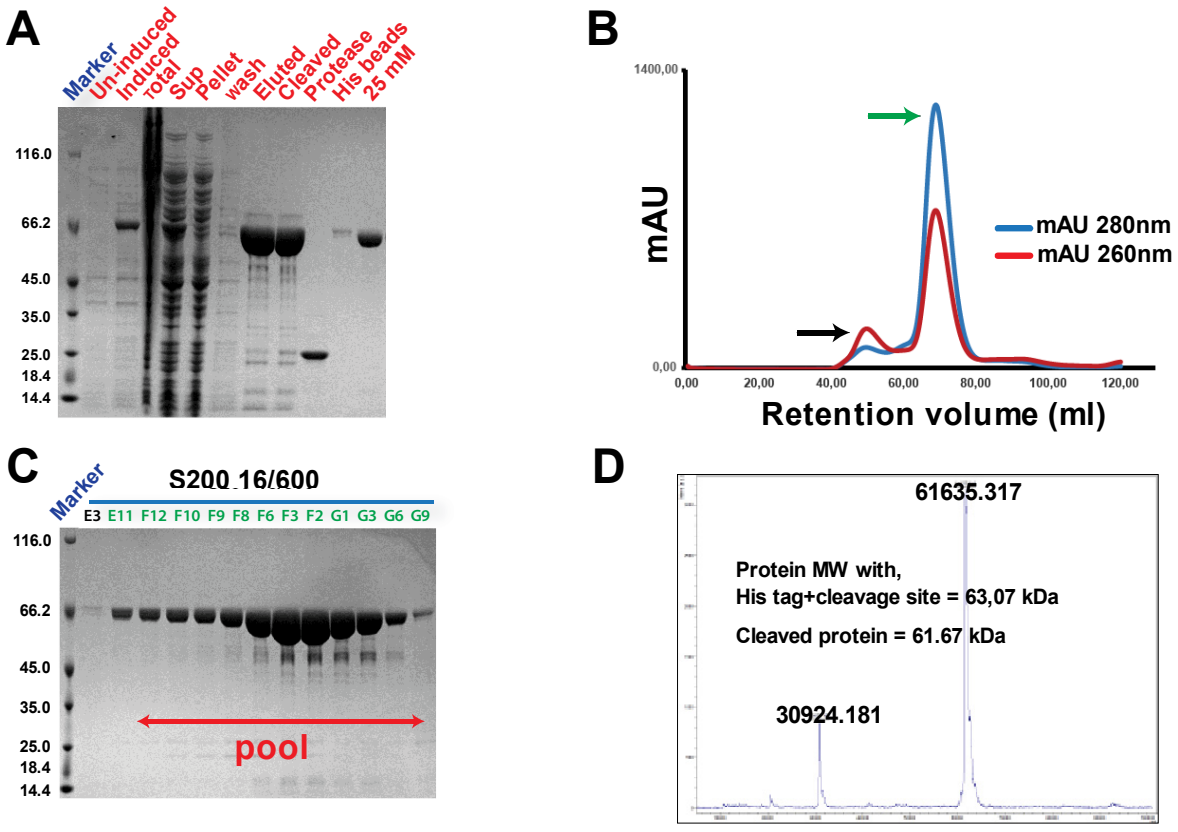

Figure 17: EHD2 expression and purification. (A) A distinct EHD2 protein band upon protein induction shows successful protein expression. Most of the protein is soluble, as evident by the corresponding band in supernatant (Sup) fraction and its absence in the pellet fraction. To remove the cleaved His_6-tag and non-cleaved EHD2, protein was applied to a reverse nickel affinity chromatography column. Cleaved protein bound to the beads in the absence of imidazole but could be eluted by low imidazole concentrations (25 mM). (B) SEC elution profile from a S200 16/600 gelfiltration column. The protein elutes mostly as a single peak with a small shoulder. (C) Coomassie-stained SDS-PAGE gel corresponding to the SEC run. (D) MALDI-TOF to confirm the protein identity and to check the His_6-tag cleavage.

High throughput inhibitor screening requires a highly purified protein that can be repeatedly prepared in a reproducible manner. To study and develop the enzymatic activity of the dynamin proteins under investigation, I purified them accordingly to previously established protocols (described in detail in 4.2.2.4).

In short, proteins were recombinantly expressed in *E. coli* with a cleavable N-terminal His_6-tag and purified by affinity chromatography (Figure 17A). Following elution from the affinity column, the tag was cleaved and removed by a second affinity chromatography step. Proteins were further purified by gelfiltration, where they eluted as a single peak (Figure 17B and C). For their mass validation, the exact mass of each protein was confirmed by MALDI TOF. A representative purification of EHD2 is illustrated in Figure 17. Large-scale purification is mentioned in 4.2.2.4.

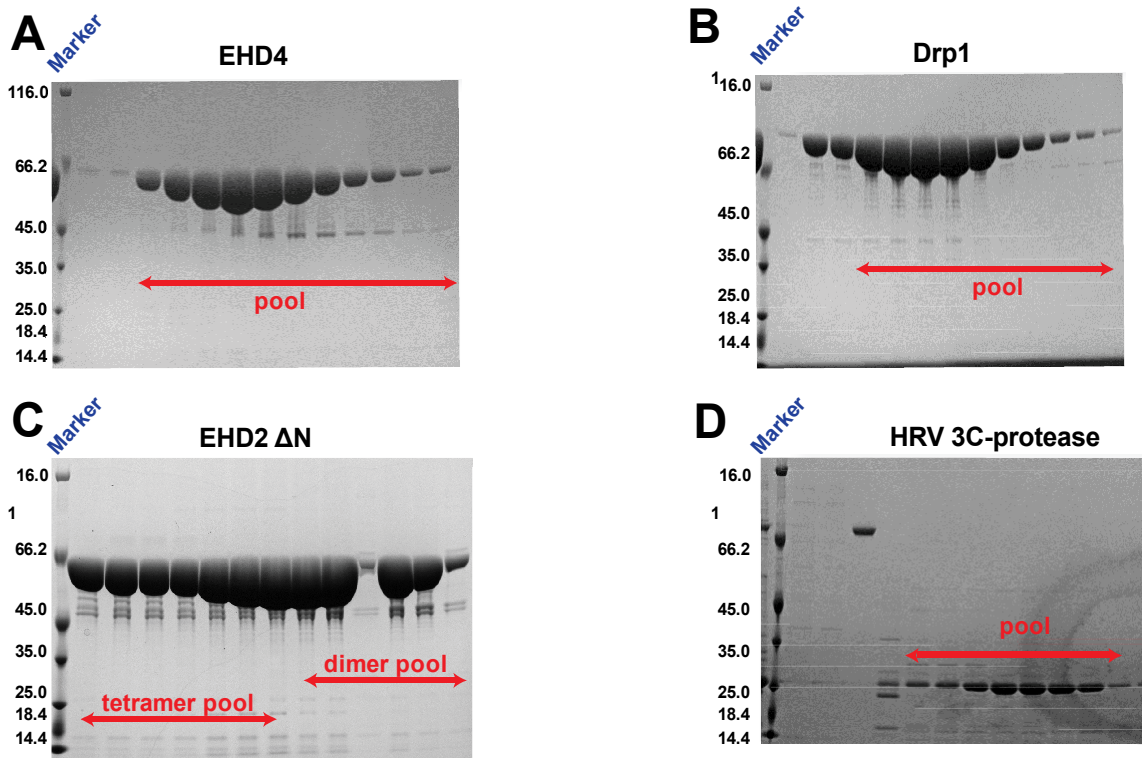

Figure 18: Representative SEC gel images for other protein purification. Coomassie-stained SDS-PAGE gels for the purification of EHD4 (A), Drp1 (B) and EHD2ΔN (C). Note that EHD2ΔN eluted in two separate peaks, both of which showed the correct molecular mass in MALDI-TOF. Further biochemical assays indicated that this construct exists in a dimer-tetramer equilibrium in solution. (D) SEC SDS gel image for Human Rhinovirus (HRV) 3C protease. I used precision protease in a 1:150 ratio to cleave the N-terminal His_6-tag of the proteins purified during my PhD.

The protein purifications for EHD4, EHD2ΔN and Drp1 and Human Rhinovirus (HRV) 3C protease were similar and are represented by their individual final SEC gel images respectively (see Figure 18).

5.1.3. EHD2 oligomerization *in vitro*

EHD proteins bind to liposomes in the presence of ATP. The induced oligomerization results in a stimulated ATPase activity (Daumke et al., 2007). EHD2 oligomerization and ring formation on tubulated liposomes was analyzed by transmission electron microscopy. Reconstituted EHD2 samples with liposomes oligomerize showing rings *in vitro* (see Figure 19). This indicates that the purified protein was functional in membrane remodeling.

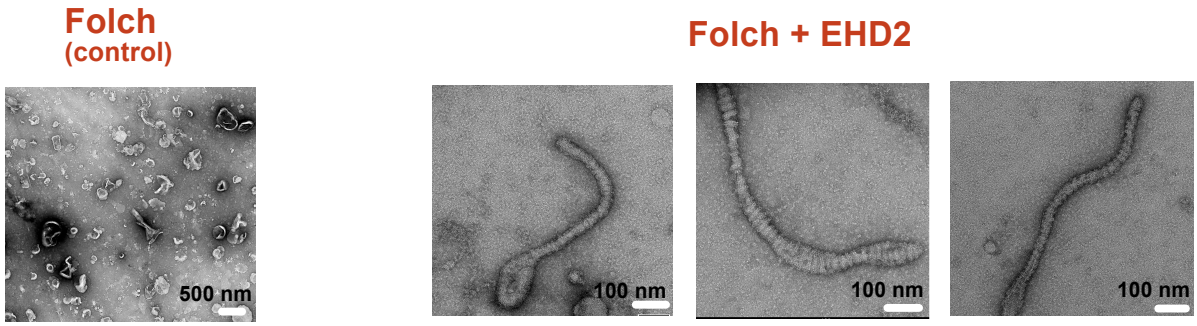

Figure 19: EHD2 ring formation. Representative micrographs of negatively stained (2% uranyl acetate) EHD2 oligomer formation on Folch liposomes in presence of nucleotide. Right panel shows micrograph of Folch lipid as a control and left panel shows 3X representative micrographs of EHD2 oligomer formation *in vitro*. Data was collected on a TALOS L120 (Thermofisher) at 92,000x magnification.

5.1.4. EHD2 ATPase assay

Having minimized the background signal in the MLG assay and purified the protein, I went ahead to analyze the ATPase activity of EHD2. At concentrations of 5 µM EHD2, 100 µM ATP and 200 µg/ml PS liposomes at 30°C, I could not detect ATPase activity by the MLG assay (Figure 20A). Changing the enzymatic conditions by varying the assay parameters did not lead to any improvement. Previously reported EHD2 ATPase activity was performed in the presence of Folch liposome (Daumke et al., 2007). To

test whether EHD2 binds at all to PS liposomes under my assay conditions, I did a co-sedimentation assay. EHD2 showed efficient binding to the PS liposomes, as evident by its appearance in the pellet fraction (Figure 20B).

I conclude that the stimulated ATPase activity is too low to be detected by the malachite green assay, in line with the reported rates (k_{obs}) of the intrinsic and stimulated ATPase of 0.7 h^{-1} and 5.6 h^{-1}, respectively (Daumke et al., 2007). A possible further explanation could be the amount of liposomes used. Previously reported activity for EHD2 proteins have mentioned the use of 1 mg/ml Folch liposomes (Daumke et al., 2007). However, such high concentration of Folch or PS liposomes cannot be used because of strong background signal in the MLG assay.

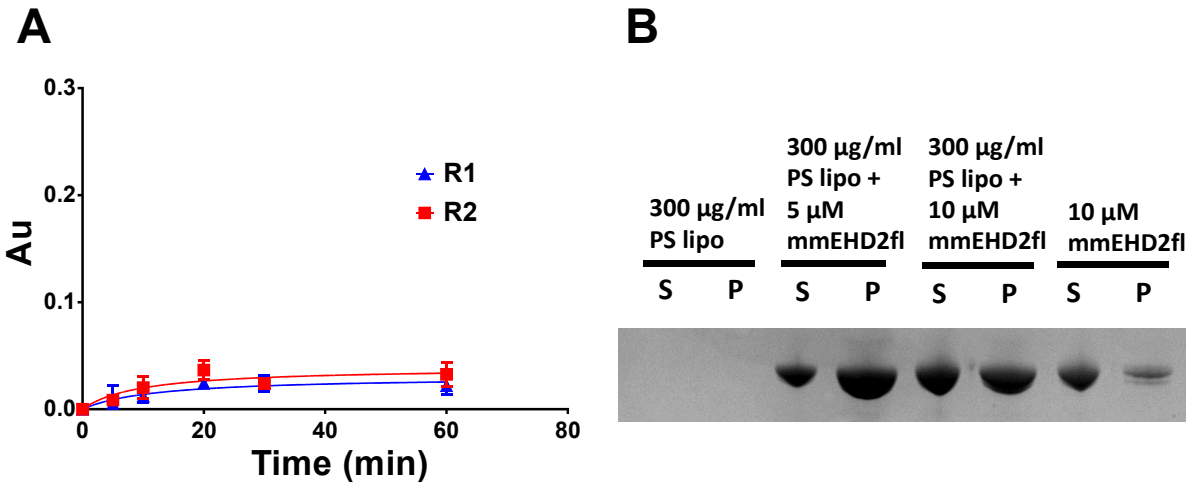

Figure 20: EHD2 ATPase activity. (A) Detecting EHD2 ATPase activity by the MLG assay. (B) Co-sedimentation assay to check EHD2 binding to the PS liposomes. Liposome binding can be detected by co-sedimentation of the protein in the pellet (P) fraction, while otherwise, most of the protein stays in the supernatant (S). R1 and R2 represents technical duplicates where data points represents the mean of two independent experiments and the error bar signifies the standard deviation. When the standard deviation is smaller than the size of the data point, it is not displayed.

I then checked the ATPase activity with other commercially available assays, ADP-Glo assay, kinase assay and its variant, kinase plus assay. ADP-Glo was described to be the most sensitive, with ADP detection limits as low as 0.1 pmol (Zegzouti et al., 2009). It also has a high signal to background luminescent readout.

However, also with these assays, I could not detect ATPase activity of EHD2 (data not shown). Increasing the protein concentration to 10 µM also did not result in detectable enzymatic activity. Re-calibration of the ADP-Glo assay standards did not lead to any improvement.

I then attempted to detect the ATPase activity by high performance liquid chromatography (HPLC), which allows quantitative analysis of the individual nucleotides in a sample (see 4.2.3.2.2). Indeed, stimulated ATPase activity was detected for EHD2 in this setup (Figure 21). Here, I used Folch lipids, as they do not interfere with the HPLC-based setup.

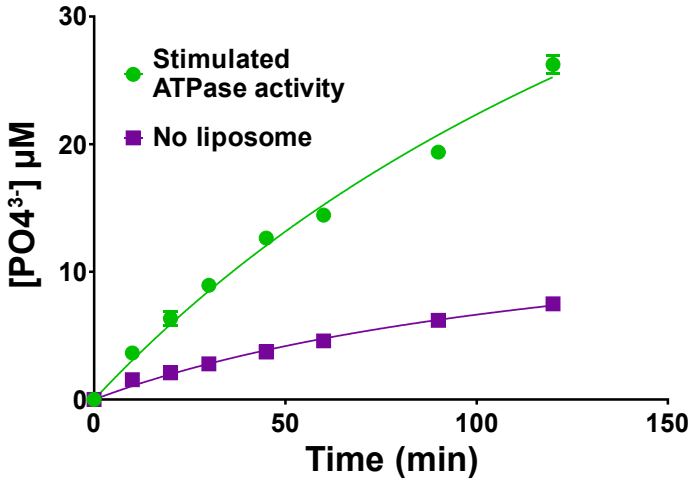

Figure 21: EHD2 ATPase assay with HPLC setup. Detecting EHD2 ATPase activity by an HPLC-based method. Assay conditions were 5 µM EHD2, 50 µM ATP and 1 mg/ml Folch liposomes at 30 °C. Data points represents the mean of two independent experiments and the error bar signifies the standard deviation. When the standard deviation is smaller than the size of the data point, it is not displayed.

Thus, by HPLC analysis, I could successfully detect an ATPase activity of EHD2 but the process was very slow. Furthermore, HPLC is a manual and time-intensive method that is not suited for high throughput screening.

5.1.5. Adapting the screening strategy

Since malachite green and other commercially available kinase assays could not be used to measure the ATPase activity of EHD2 and HPLC is not suited for a HTS, I turned my attention towards other EHDs. Sequence alignment of the four EHDs in mouse indicated that the catalytic active sites are highly conserved (see Figure 22).

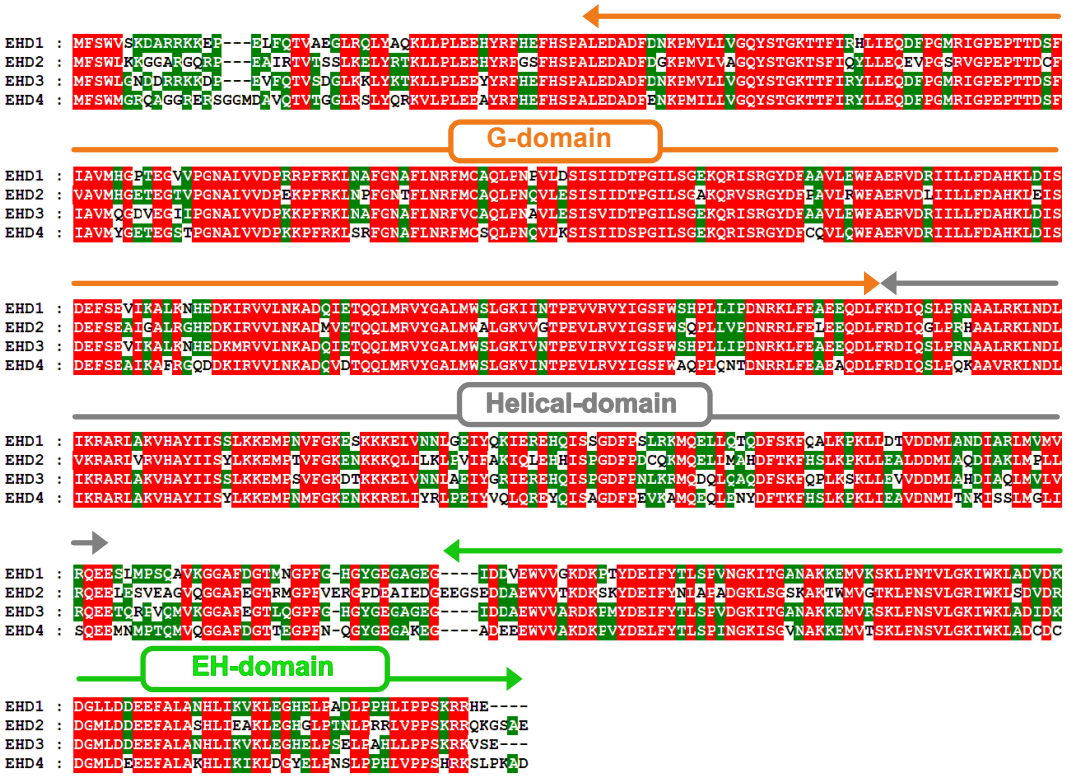

Figure 22: Sequence alignment of the four mouse EHD sequences. G-domain, helical and EH domains have been mentioned.

I chose EHD4 for further analysis, as it was enzymatically more active compared to EHD2 and the crystal structure was published previously (Melo et al., 2017). Since, I was still interested in finding EHD2 inhibitors, I designed a new strategy and workflow (Figure 23).

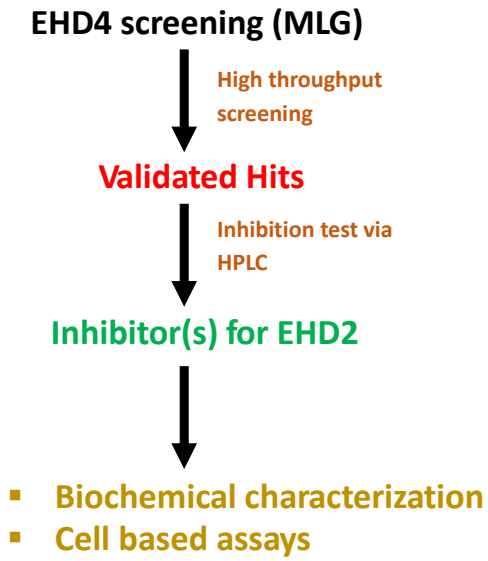

Figure 23: Workflow adopted in this project. EHD4 was chosen for high throughput screening since its ATPase activity was high enough for HTS. The final validated hits from EHD4 would then be tested in an HPLC-based setup for inhibition against EHD2 and in cellular assays to observe potential effects on lipid uptake.

5.1.6. Optimizing EHD4 ATPase assay for screening

In initial experiments with 5 µM EHD4, 200 µM ATP and 300 µg/ml PS liposome, ATPase activity could be detected in the MLG assay, but it was highly irreproducible (Figure 24).

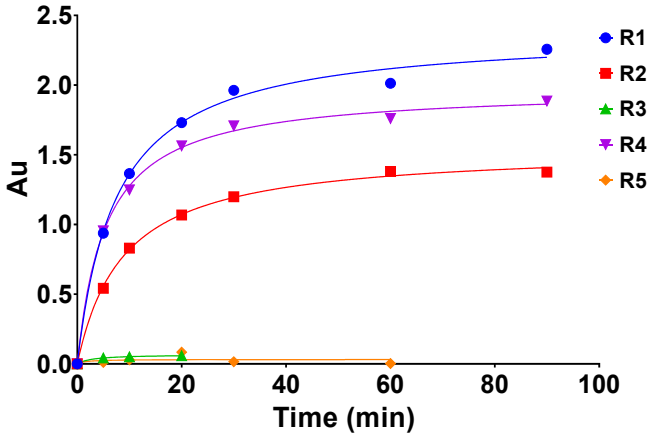

Figure 24: Variability in EHD4 ATPase activity by MLG assay. ATPase activity of EHD4 was detected by a MLG assay but it was not reproducible. R1-R5 represent different repetitions of the EHD4 assay under supposedly identical conditions. Data points represents the mean of two independent experiments and the error bar signifies the standard deviation. When the standard deviation is smaller than the size of the data point, error bar is not displayed.

5.1.6.1. Use of synthetic lipid

Due to its variability, the assay in this form was not suited for HTS. To remove batch-to-batch variation of the PS lipids extracted from a natural source, I tested two different synthetic PS lipids, 18:1 PS (also known as DOPS) and 18:0-18:1 PS. Strikingly, the ATPase activity of EHD4 was highly reproducible when done with different batches of synthetic lipids (Figure 25A). I also mixed the two synthetic lipids in a ratio to mimic closely the naturally occurring brain PS lipid but the activity remained same (Figure 25B). I finally decided to use DOPS (1,2-dioleoyl-sn-glycerol-3-phospho-L-serine). It is an excellent substitute for the naturally occurring brain PS (Avanti Lipids Merck). It has similar physical properties and is more stable to oxidation. These synthetic liposomes had hardly any background signal in the MLG assay (Figure 25C).

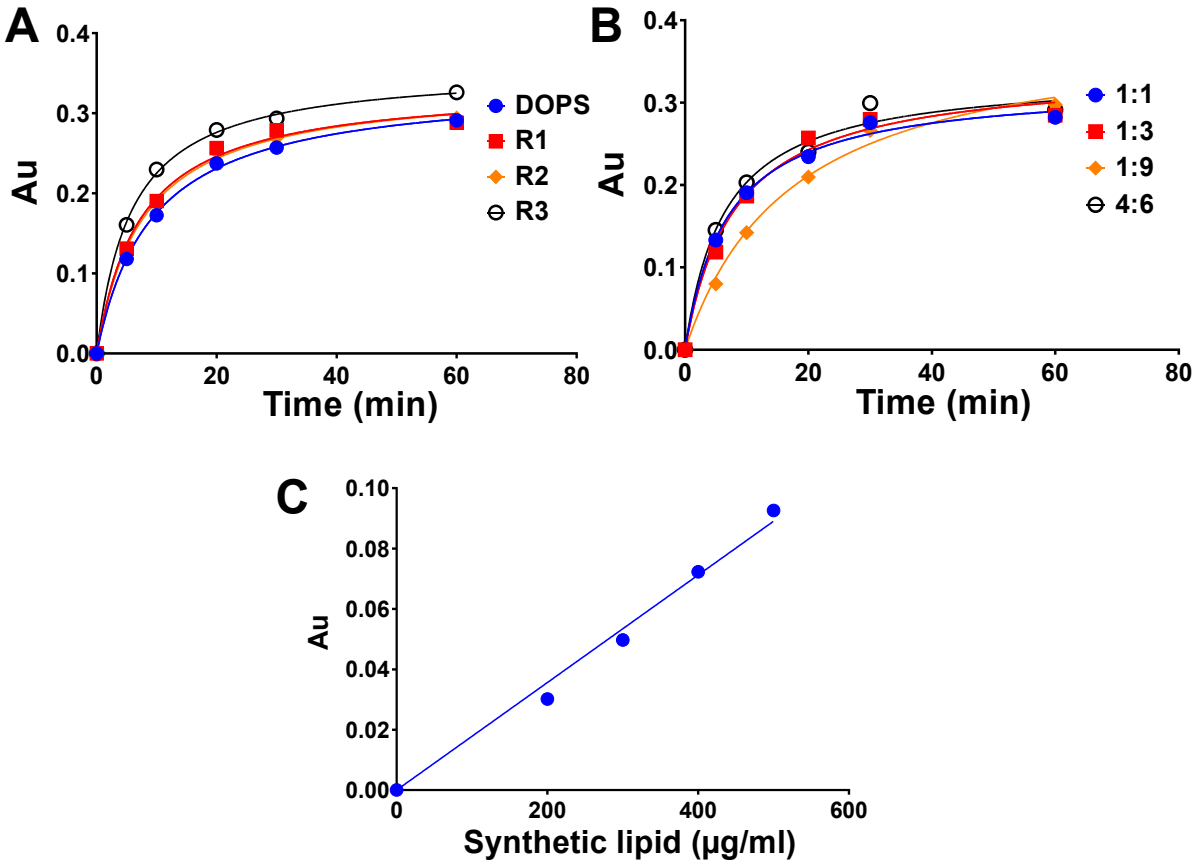

Figure 25: Use of synthetic lipid in Malachite green assay. (A) ATPase assay with synthetic lipid DOPS (18:1 PS) and 18:0-18:1 PS lipid was done. R1, R2 and R3 represent three independent preparations of 18:0-18:1 PS and they all showed the same activity. (B) The two different synthetic lipids (18:1 PS and 18:0-18:1 PS) were mixed in different ratios to check if there was an increase in ATPase activity. (C) Background signal from DOPS at different concentrations.

5.1.6.2. MLG assay precision

To evaluate the accuracy of the MLG assay, I compared it to the HPLC-based method which is considered to be more accurate (da Costa Cesar et al., 2008; Gackowski et al., 2019). Assays were carried out in parallel under identical conditions and yielded comparable results (Figure 26).

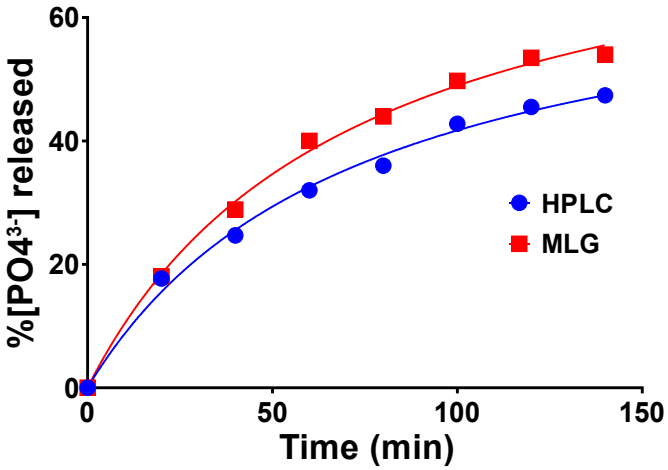

Figure 26: Comparison between the malachite green assay (MLG) and HPLC method. 5 µM EHD4, 50 µM ATP and 250 µg/ml PS lipids were used in the ATPase assay.

5.1.6.3. Temperature dependence of enzymatic activity

I next optimized the assay temperature. Initially, I wanted to do the ATPase assay at 37 °C so as to have a physiological relevance regarding the inhibition, but at 37 °C EHD4 showed lower activity (Figure 27A) which was increased by decreasing the temperature (Figure 27B). In the HTS setup, incubation at higher temperature e.g. 30 °C or more was not easily feasible. Keeping this in mind, I kept my assay temperature to 25 °C.

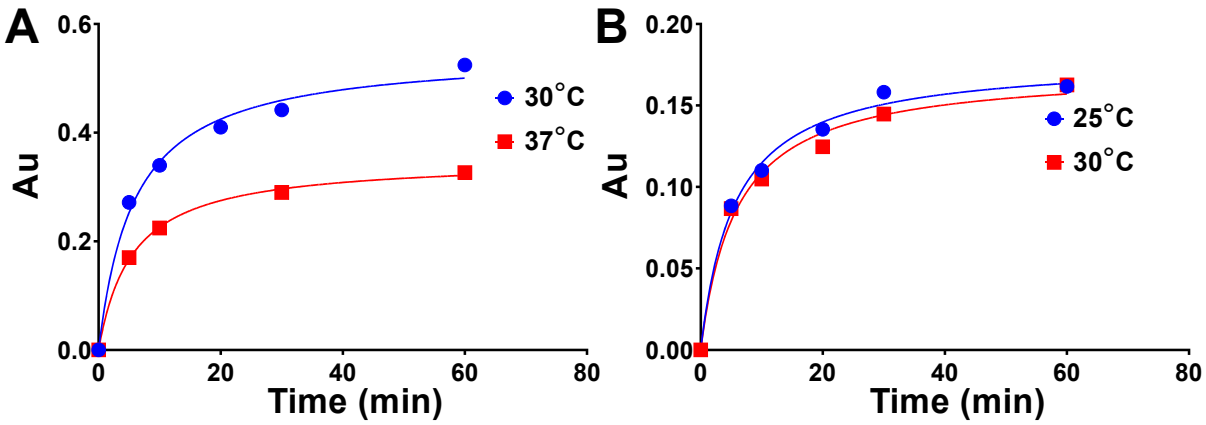

Figure 27: Role of temperature in EHD4 activity. (A) ATPase assay were done at 37 °C and at 30 °C in the presence of 50 µM ATP. (B) ATPase assay comparison at 30 °C and at 25 °C at a concentration of 20 µM ATP. For HTS, reactions were carried out at 25 °C.

5.1.6.4. Liposome size preference

Previous studies have shown that membrane-binding proteins have curvature dependence (Jin et al., 2022) and a liposome size-dependent ATPase activity has been reported for EHD2 (Daumke et al., 2007).

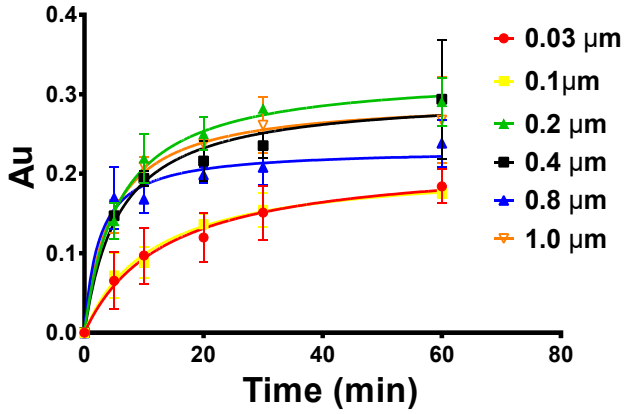

Figure 28: EHD4 ATPase activity in dependence on liposomes size. (A) 4 µM EHD4, 30 µM ATP and 500 µg/ml DOPS were used in the ATPase assay done at 25 °C. Results from 0.2 µm and 1.0 µm were similar therefore 0.4 µm was chosen. Data points are means of two independent experiments and the error bar signifies the standard deviation. When the standard deviation is smaller than the size of the data point, error bar is not displayed.

To analyze liposome size dependency of EHD4, I used liposomes extruded through different pore sizes (see 4.2.2.7) and tested their effect on ATPase activity. Liposomes extruded through a 0.4 µm filter showed the highest reproducible ATPase activity (Figure 28), and was therefore chosen for HTS.

5.1.6.5. Cations influencing enzymatic activity

Potassium and magnesium ions can influence ATPase activities, as demonstrated already in 1988 for plant ATPase (Varanini, 1988). Role of potassium ions have also been demonstrated for dynamin (Chappie et al., 2010). In line with these observations, addition of 1.5 mM potassium chloride in the assay buffer increased the ATPase activity of EHD4 approximately by 3-fold (Figure 29A). Testing three different concentrations, 150 mM potassium chloride in the assay led to the maximal activity (Figure 29B). Removing all sodium ions from the buffer led to a slight further increase in ATPase activity (Figure 29B, only 150 mM).

Similarly, I also checked the influence of magnesium ions. The ATPase activity of EHD4 and EHD2 was not influenced by the addition of lower $MgCl_2$ concentrations (0.5 mM) (Figure 29C) while higher concentration (4 mM) inhibited the enzymatic activity (data not shown).

From here on, the final optimized buffer conditions were 20 mM Hepes (pH 7.5), 150 mM KCl, 0.5 mM $MgCl_2$. Both EHD4 and EHD2 were stable in this buffer. A representative reaction regarding potassium ions for EHD4 and magnesium ions for EHD2 is shown in Figure 29.

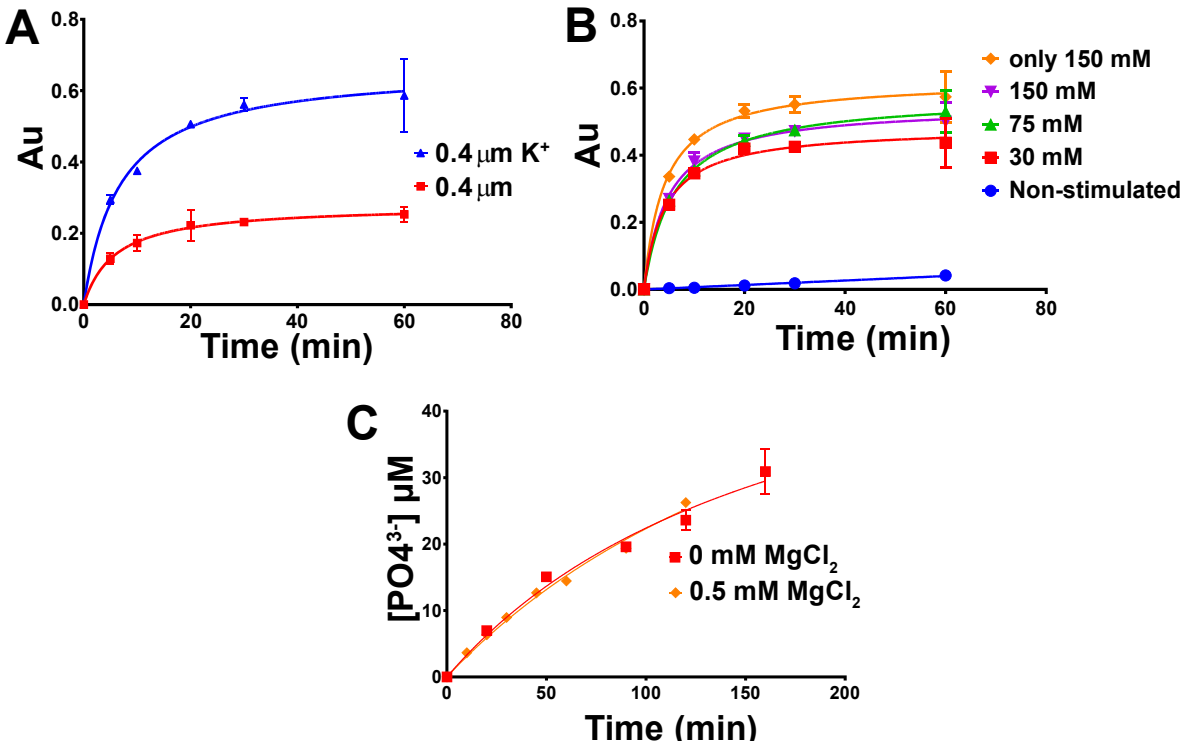

Figure 29: Role of potassium and magnesium ions for EHD4 enzymatic activity (A) Addition of 1.5 mM potassium chloride (indicated by K^+) increases the enzymatic activity by three folds. 4 µM EHD4, 30 µM ATP and 500 µg/ml DOPS were used in the ATPase assay done at 25 °C (B) Different concentration of potassium ions were analyzed. Removal of sodium ions in the presence of 150 mM KCl even slightly increased ATPase activity. 1 µM EHD4, 30 µM ATP and 500 µg/ml DOPS were used in the ATPase assay done at 25 °C. (C) Addition of 0.5 mM magnesium ions did not influence liposome-stimulated ATPase activity for EHD2. 5 µM EHD2, 50 µM ATP and 1000 µg/ml Folch were used in the ATPase assay done at 25 °C. EHD4 ATPase was done with malachite green assay whereas EHD2 ATPase was done in an HPLC based setup. The data points represent the mean of two independent experiments and error bar (standard deviation). Error bars are not displayed when it is smaller than the size of data point.

Under these optimized buffer condition, EHD4 ATPase assay appeared as shown in Figure 30.

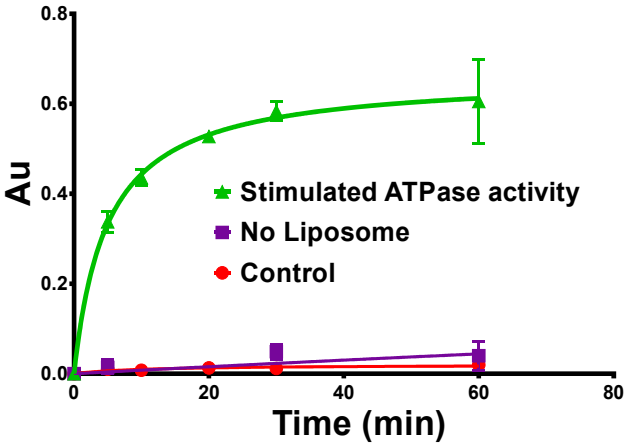

Figure 30:EHD4 ATPase assay. 4 µM EHD4, 500 µg/ml DOPS and 30 µM ATP in the optimized assay buffer was used to detect enzymatic activity at 25 °C. Data points represents the mean of two independent experiments and the error bar signifies the standard deviation. When the standard deviation is smaller than the size of the data point, it is not displayed.

5.1.6.6. Optimizing the protein concentration

I previously used 4 µM EHD4 which is a high protein concentration to screen against an inhibitor concentration of 10 µM. I therefore performed an EHD4 titration. As can be seen in Figure 31, EHD4 was also active at lower concentrations.

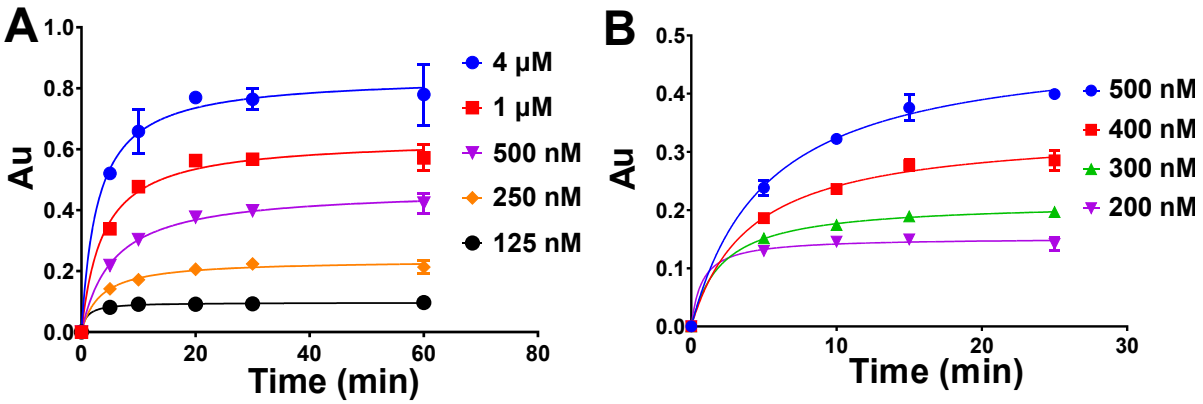

Figure 31: Protein titration. (A) EHD4 ATPase activity was screened at different protein concentrations, as indicated. (B) Fine tuning of the protein concentrations. Assay conditions were, 30 µM ATP and 500 µg/ml DOPS at 25 °C. Data points represent the mean of two independent experiments and the error bar signifies the standard deviation.

5.1.6.7. Optimizing the lipid concentration

Next, I analyzed the liposome concentration dependency on ATPase activity while keeping EHD4 concentration at 400 nM. Surprisingly, at lower DOPS concentrations, an increase in enzymatic activity was observed, with a maximal activity between 75 µg/ml and 50 µg/ml (Figure 32). 50 µg/ml DOPS liposomes were used from here onwards keeping in mind the cost of synthetic lipids.

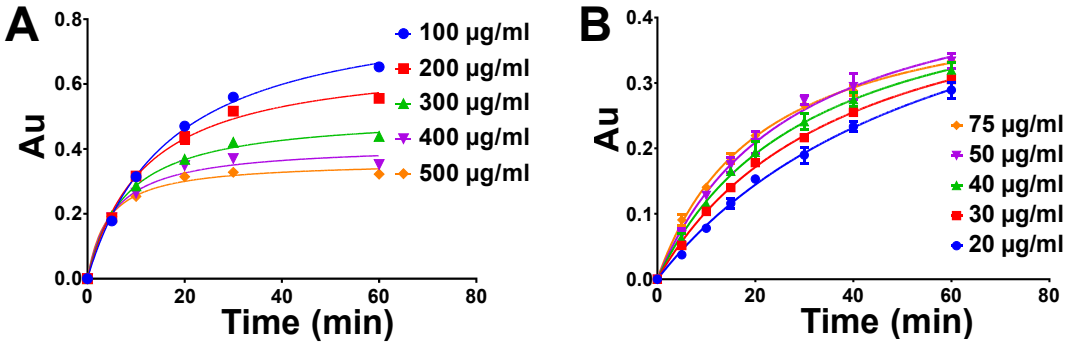

Figure 32: Enzymatic activity depends on liposome concentration. (A DOPS concentration dependent ATPase activity of EHD4. (B) Fine-tuning of the DOPS concentration. Assay conditions were, 400 nm EHD4, 50 µM ATP and 500 µg/ml DOPS at 25 °C. Data points represents the mean of two independent experiments and the error bar signifies the standard deviation. When the standard deviation is smaller than the size of the data point, it is not displayed.

5.1.6.8. Protein titration at lower lipid concentration

As the protein and liposome concentrations are intertwined, I re-analyzed the enzymatic activity dependence on EHD4 concentrations by keeping the liposome concentration at 50 µg/ml. A protein dependent increase in ATP activity was observed (Figure 33). To obtain a signal to noise ratio (SNR) of at least 2 (Bisswanger, 2014; Brooks, 2012) while at the same time using a low protein concentration, I chose 200 nM EHD4 and 50 µg/ml liposomes for the subsequent enzymatic assays.

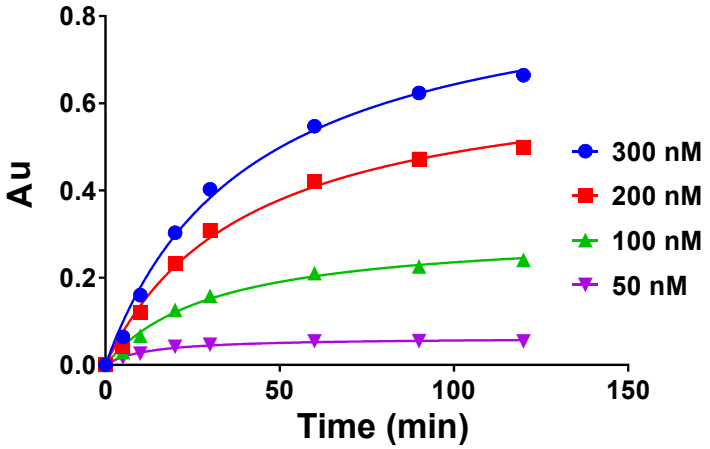

Figure 33: Protein titration at fixed liposome concentration. Different EHD4 concentrations were tested at 50 µg/ml DOPS liposome. Assay conditions were 50 µM ATP and 50 µg/ml DOPS at 25 °C. The data points represents the mean of two independent experiments and the error bar signifies the standard deviation. When the standard deviation is smaller than the size of the data point, it is not displayed.

5.1.6.9. Effect of DMSO in the assay

In the drug library, compounds are stored in DMSO so I tested the influence of DMSO on the liposome-stimulated ATPase activity of EHD4. By compound dilution, a minimum of 1% DMSO would be expected in the assay. As shown in Figure 34, the presence of even 1.5% DMSO at two different protein concentrations (200 and 300 nM) had no effect on the enzymatic activity of EHD4. Therefore, the enzymatic assay was compatible with the HTS setup.

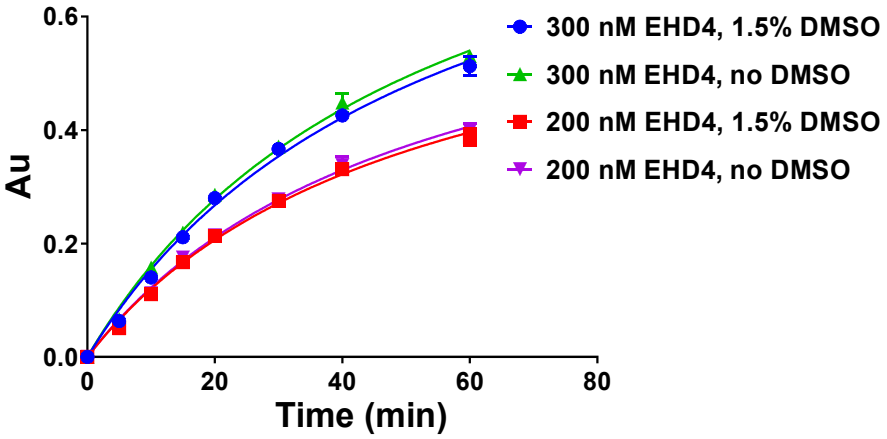

Figure 34: Effect of DMSO on the enzymatic activity of EHD4. Assay conditions were 50 µM ATP and 50 µg/ml DOPS at 25 °C. The data points represents the mean of two independent experiments and the error bar signifies the standard deviation. When the standard deviation is smaller than the size of the data point, it is not displayed.

5.1.6.10. K_m determination

In the newly optimized assay conditions, the enzymatic activity could easily be detected and was reproducible. Under these assay conditions, I determined the K_m of the reaction. Initial velocities of the reaction were obtained at different substrate concentrations (Figure 35A) and then plotted against the substrate concentration. In this way, a K_m of 20 (±3) µM was obtained for EHD4 (Figure 35B) (see 4.2.3.2 for details).

For inhibitor screening, I aimed to have a substrate concentration as close as possible to the K_m to be able to target competitive and non-competitive inhibitors (for detailed discussion see 6.1.3). At an ATP concentration of 30 µM, the signal to noise (SNR) was 2.1 (Figure 35C), whereas it was only 1.6 at 20 µM ATP. To maintain an SNR>2, I chose 30 µM ATP as substrate concentration for HTS, which was still close to the K_m.

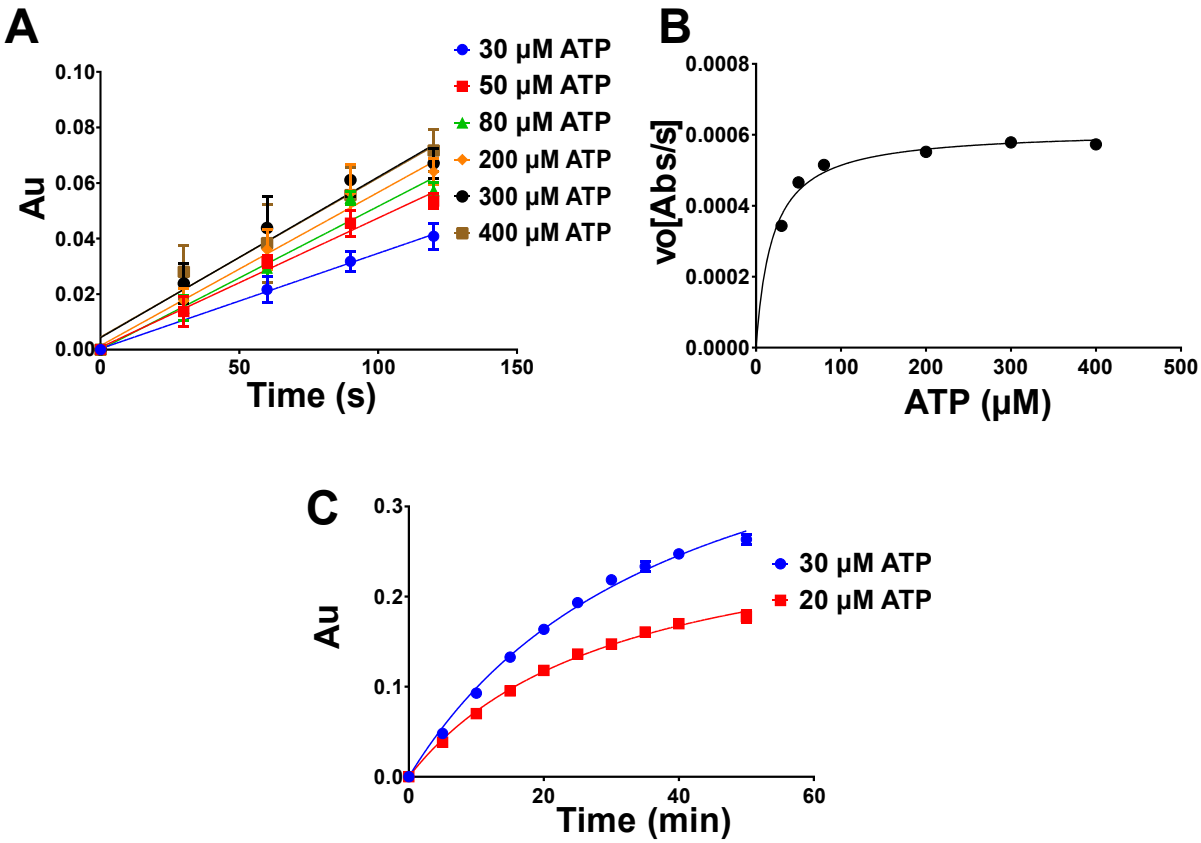

Figure 35: K_m determination of EHD4 and choosing the ATP concentration. (A) Initial velocity at different ATP concentrations were determined by calculating the slope of the linear reaction. (B) K_m was determined by plotting the initial rates of the reactions vs. the substrate concentration. The kinetic parameters for EHD4 are K_m = (20 ± 3) µM, k_{cat} = (0.001 ± 3.6e-0.05) 1/s, v_{max} = 0.000613 µmoles ATP/s. (C) ATPase activity at different ATP concentrations. The signal to noise ratio was 1.6 for 20 µM ATP whereas it was 2.1 with 30 µM ATP. The data points in A and C represent the mean of two independent experiments and the error bar signifies the standard deviation. When the standard deviation is smaller than the size of the data point, it is not displayed.

5.1.6.11. Z-factor (Z´) calculation

After optimizing the different parameters, the final assay conditions for the EHD4 ATPase assay were 200 nM EHD4, 30 µM ATP, 50 µg/ml 0.4 µm-sized DOPS liposomes at 25 °C in 20 mM Hepes (pH 7.5), 150 mM KCl, 0.5 mM $MgCl_2$. In these final conditions, the subsequent ATPase assays were performed (Figure 36).

In the optimized assay conditions, Z´ was calculated at 15 min in 16 replicates as mentioned in (Zhang et al., 1999). Z´ is a statistical parameter, which describes the

separation between the positive and negative control. Its assessment provides the likelihood of getting false positive and false negative. Z´ values between 0.5 and 1.0 are considered to be excellent for HTS (Zhang et al., 1999).

The Z´ value for my optimized assay was 0.895. In every of the subsequent experiments, the Z´ value was in between 0.8 – 0.9.

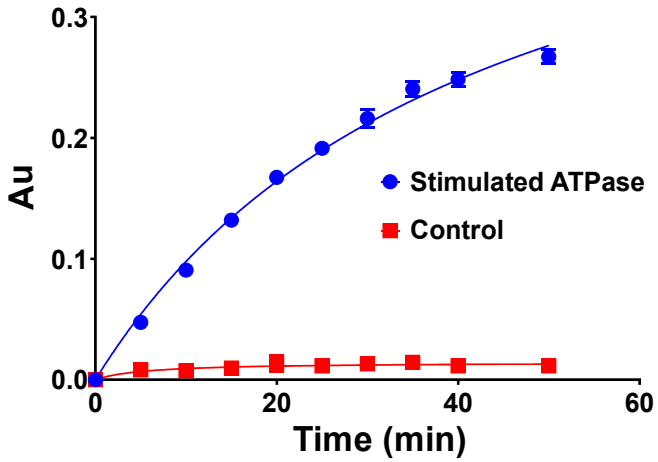

Figure 36: EHD4 ATPase assay done in the final optimized assay parameters. EHD4 ATPase assay was done with 200 nM EHD4, 30 µM ATP, 50 µg/ml 0.4 µm filtered DOPS liposomes at 25 °C in 20 mM Hepes (pH 7.5), 150 mM KCl, 0.5 mM $MgCl_2$. Data points represent the mean of four independent experiment and the error bar signifies the standard deviation. When the standard deviation is smaller than the size of the data point, error bar is not displayed.

5.1.6.12. Drp1 enzymatic activity

Similar to EHD4, also Drp1 showed stimulated GTPase activity by using almost identical assay parameters. I further fine-tuned these parameters for Drp1. The optimized assay conditions were 300 nM Drp1, 60 µM GTP, 200 µg/ml DOPS at 25 °C in 20 mM Hepes (pH 7.5), 150 mM KCl, 0.5 mM $MgCl_2$. K_m determination for Drp1 and a final GTPase assay in the optimized assay conditions are shown Figure 37A/B and C, respectively. K_m for Drp1 is 66 (±9) µM and K_{cat} is 0.112 s^{-1}. Z´ value for Drp1 at 20 min was 0.72.

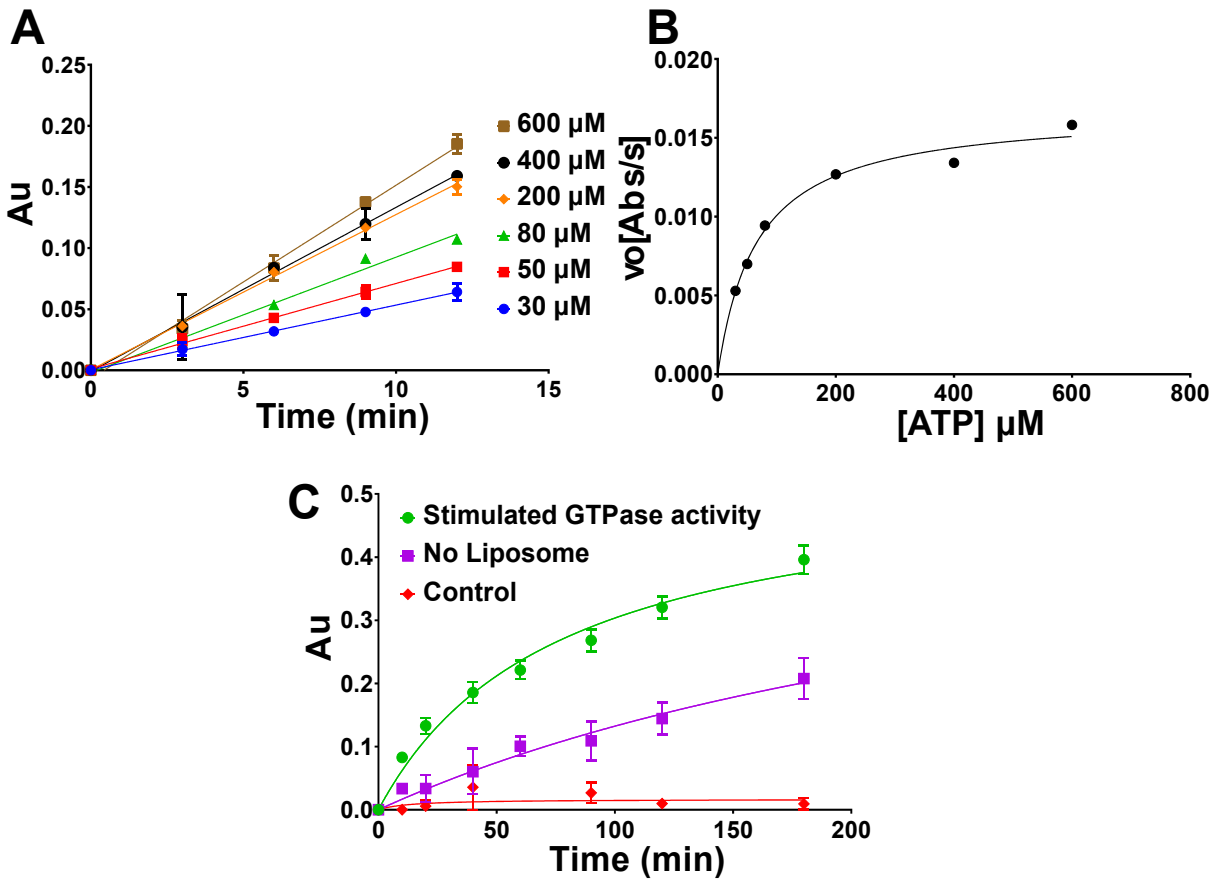

Figure 37: Enzymatic kinetics for Drp1. (A) Initial velocities at different substrate concentrations were determined by a linear fit. (B) K_m determination by plotting initial rate of the reaction vs. the substrate concentration. Enzymatic parameters for Drp1 are K_m= (66 ± 9) µM, k_{cat} = (0.112 ± 0.004) 1/s, v_{max} = 0.0167 µmoles/s. (C) GTPase assay done in the final optimized parameters. These conditions were 300 nM Drp1, 40 µM GTP, 200 µg/ml DOPS done at 25°C in 20 mM Hepes (pH 7.5), 150 mM KCl, 0.5 mM $MgCl_2$. Z´ and SNR were 0.72 and 2.1 at 20 min respectively. The data points in A and C represents the mean of two independent experiments and the error bar signifies the standard deviation. When the standard deviation is smaller than the size of the data point, error bar is not displayed.

5.1.7. Screening for EHD4 Inhibitors

A first screening attempt to screen for EHD4 inhibitors in the laboratory of Stefan Knapp, structural genomics consortium (SGC), Goethe University, Frankfurt, was not successful. A total of 1,654 compounds were analyzed for ATPase inhibition, out of which 1,114 compounds were FDA- (United States Food and Drug administration) approved drugs, 352 were clinical compounds and 188 were from kinase chemogenic

data set (KCGS). KCGS is a collection of well annotated small molecule ATP-competitive inhibitors that were produced during drug discovery programs targeting protein kinases (Wells et al., 2021). Probably because of a defect in pipetting (multi-channel pipette), results from this screen were not reproducible and not further followed up.

In a second attempt, I screened drug libraries in the Screening Facility of the Leibniz-Forschungsinstitut für Molekulare Pharmakologie (FMP). 16,000 compounds were screened: Out of these, 2,112 compounds belong to the library of pharmacological active compounds (LOPAC) (Sigma-Aldrich),1,760 compounds were donated from the lab of Prof. Stefan Laufer (University of Tübingen) and 11,264 compounds were from the diversity set library. The diversity set library contains compounds that were computationally designed to cover a maximal chemical space, and compounds from CHEMBL database which were already found for a specified target protein with an IC_{50} value of less than 5 µM (Lisurek et al., 2010).

Data was analyzed with an automated pipeline (Hinderlich et al., 2017). Compounds showing decrease in enzymatic activity by 25% were grouped as inhibitors. Similarly, compounds showing increase in enzymatic activity by 25% were grouped as activators. In this way, 99 inhibitors and 70 activators were found in the preliminary screenings.

For validation, we re-analyzed the hits from the preliminary screening in duplicates. Validation assays were done in a similar manner as to the preliminary screen. Compounds whose effect on enzymatic activity could be reproduced in duplicates were grouped as validated hits, yielding 59 inhibitors and 70 activators. These validated hits were carried forward to the counter screening assays.

5.1.7.1. Counter-screening

To eliminate those validated hits that interfere with the colorimetric assay, I counter screened them. First, I analyzed the colorimetric reaction in the presence of 30 µM PO_4^{3-} and 10 µM and 50 µM inhibitor. None of the inhibitors were found to interfere with the colorimetric reaction. This left 59 inhibitors for a more specific analysis.

I also aimed to exclude compounds that themselves induce a colorimetric reaction in the Malachite green assay. All putative activators, some of them only at 50 µM

(see Figure 38), induced a colorimetric reaction excluding them as specific EHD4 activators.

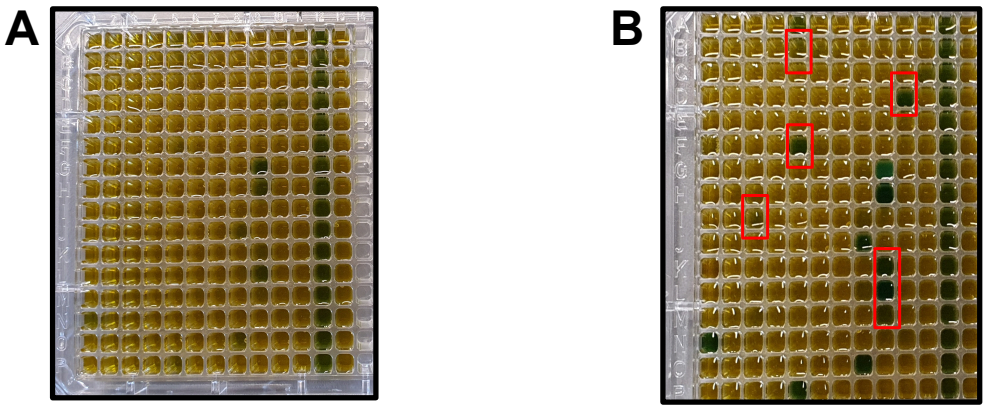

Figure 38: Intrinsic effect of compounds at a higher concentration in a counter screen. (A) counter screen for activators at 10 µM and (B) counter screen for activators at 50 µM compound concentration. Red rectangular bars represent those false hits, which were not detected at 10 µM.

5.1.7.2. IC_{50} measurement

IC_{50} was determined as mentioned in 5.1.7.2 and data processed in the same way as done in preliminary screening. 8 compounds showed no dose-dependent response, implying that they may precipitate at higher concentrations. For the remaining compounds, the IC_{50} values were in lower micromolar range (between 0.38 µM to 16 µM).

5.1.7.3. Counter screening for liposome false positive

To exclude inhibitors that interfere with liposome integrity or show unspecific inhibition of dynamin superfamily proteins, the 59 compounds were subsequently counter-screened for their effect on the stimulated GTPase activity of a distantly related dynamin superfamily member, Drp1. Since a dose-dependent response is more reliable than a measurement at a single concertation, IC_{50} values were determined.

Based on the determined IC_{50} curve and the IC_{50} value, known biological activities, redox potential and inhibitor specificity, 16 compounds called (MS1-16) with IC_{50} values as mentioned in Table 7 were selected for further evaluation (A detailed discussion on the selection criteria can be found in section 6.2). Notably, two of these inhibitors stimulated Drp1 GTPase activity (Figure 39).

Table 7: IC_{50} values for the selected compounds against EHD4 that were continued in this study

Compound	IC_{50} (µM)
MS1	0.92
MS2	0.49
MS3	13
MS4	6.5
MS5	8.2
MS6	1.8
MS7	2.4
MS8	3.8
MS9	5
MS10	2.9
MS11	0.38
MS12	3.2
MS13	3.1
MS14	0.71
MS15	6.2
MS16	1.3

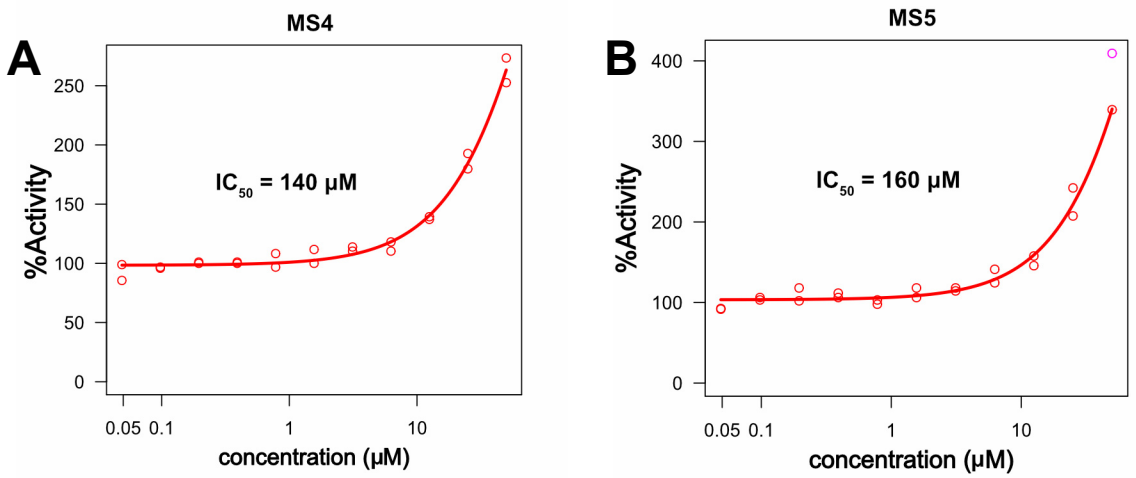

Figure 39: Activators for Drp1 found in the counter-screening. (A) and (B) Compounds MS4 and MS5 increases the stimulated GTPase activity of Drp1. Measurement was done in duplicates and all the data points plotted. Magenta dot on top right is the data point excluded from the best fit as an outlier.

The purchased 16 chosen compounds did not interfere with the malachite-green assay (Figure 40) and showed identical molecular mass compared to their parental compounds in the FMP screening library.

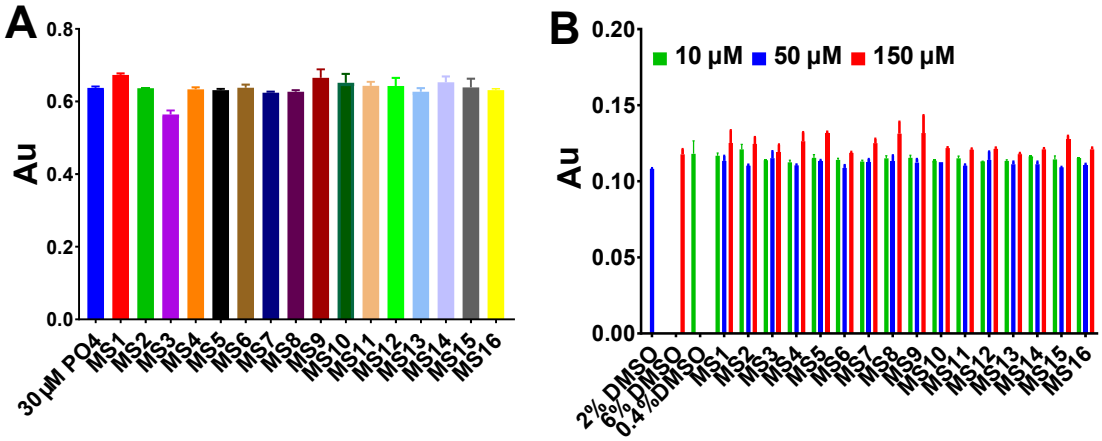

Figure 40: Counter screen for the purchased compounds. (A) False hit for inhibitor was analyzed against 30 µM phosphate as a control. Abs_{650} (Au) remains constant as the control showing inhibitor does not interfere in the complex formation. (B) False hit for activator was analyzed at three different concentrations (10 µM, 50 µM and 150 µM), control was the amount of DMSO (0.4% DMSO for 10 µM, 2% DMSO for 50 µM and 6% DMSO for 150 µM). Similar signal was observed as the respective control showing that the compounds do not form a complex with the dye. Data points are means of two independent experiments and the error bar signifies the standard deviation.

5.1.8. Validation

For the validation assays, I kept the same parameters as during HTS and performed a one-hour time course of enzyme kinetics. Compounds at 10 µM showed inhibition of the enzymatic activity (Figure 41A) and an increase in inhibition was observed at 50 µM (Figure 41B).

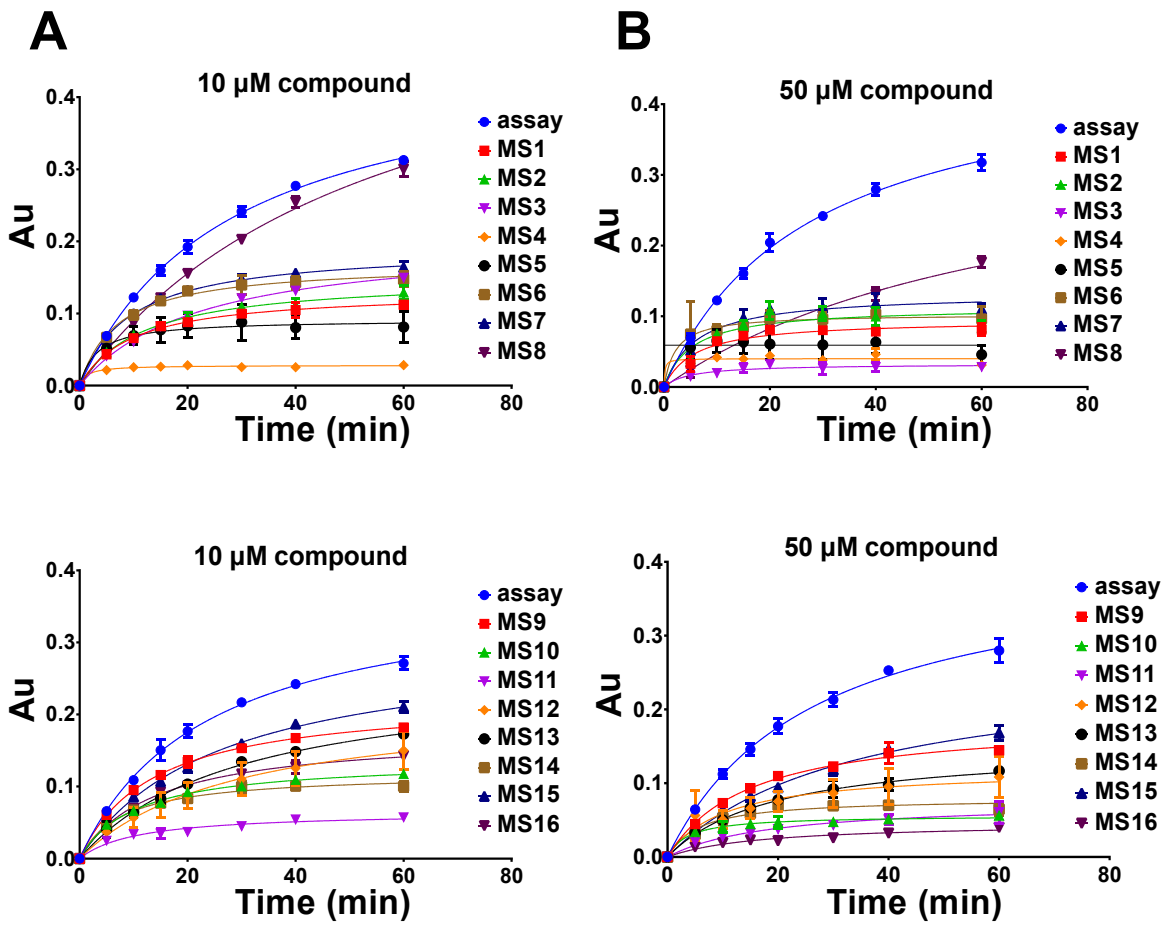

Figure 41: Validation assay by Malachite green dye. One-hour time course of enzyme kinetics was done at 10 µM (A) and 50 µM (B) compound concentrations. ATPase assay was done in the following conditions: 200 nM EHD4, 30 µM ATP, 50 µg/ml DOPS liposomes at 25 °C. Assay (blue curve) defines the positive control. Data points are means of two independent experiments and the error bar signifies the standard deviation. When the standard deviation is smaller than the size of the data point, error bar is not displayed.

To remove any assay bias, I validated the compounds in an HPLC-based assay setup using the same assay condition. In agreement with the colorimetric assay, all

compounds inhibited the enzymatic activity at 10 µM in the HPLC-based assay (Figure 42A) and increased inhibition was observed at 50 µM compound concentration (Figure 42B).

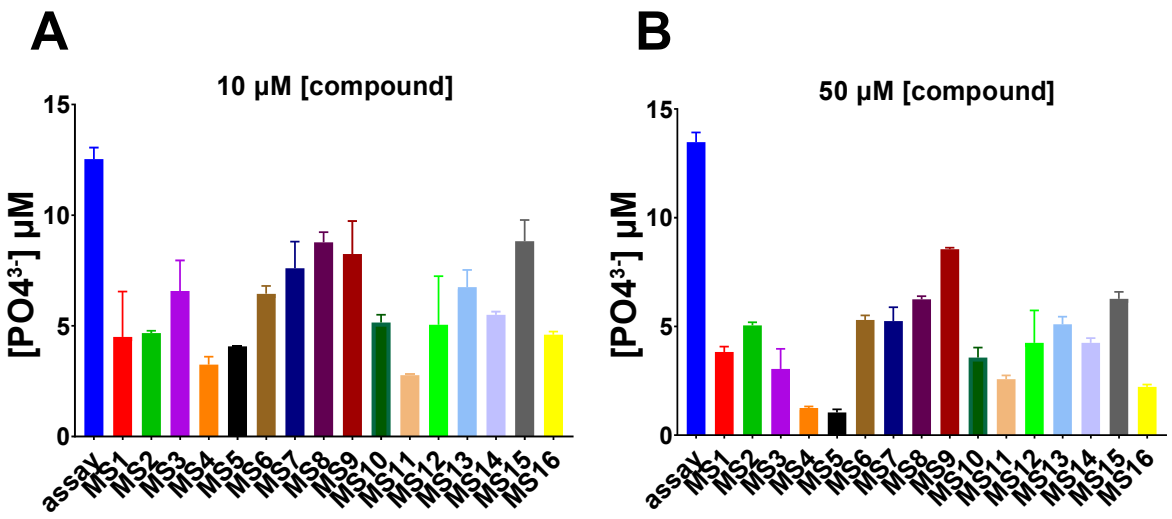

Figure 42: Validation done with a HPLC based setup. (A) Compound validation done at 10 µM. Inhibition of the enzymatic activity can be seen. (B) Compound validation done at 50 µM. ATPase assay was done in the following conditions: 200 nM EHD4, 30 µM ATP, 50 µg/ml DOPS liposomes at 25 °C. Assay (blue bar) defines the positive control. Data points are means of two independent experiments and the error bar signifies the standard deviation. When the standard deviation is smaller than the size of the data point, error bar is not displayed.

5.1.8.1. Saturation kinetics

To analyze if the inhibitors are competitive or non-competitive, I performed saturation kinetics. Increased substrate concentration leading to loss of inhibition is indicative for a competitive inhibitor which binds in the catalytic binding pocket and competes with ATP access. For saturations kinetics, I used a substrate concentration 10-fold higher than in my screen (e.g. 300 µM ATP). Compounds MS3, MS6, MS7, MS9, MS12, MS13, MS14 and MS15 showed competitive inhibition (Figure 43). In contrast, ATPase activity in the presence of inhibitors MS1, MS2, MS4, MS5, MS10, MS11 and MS16 was not accelerated by higher ATP concentrations (Figure 43). These could be classified as non-competitive inhibitors or un- competitive inhibitors.

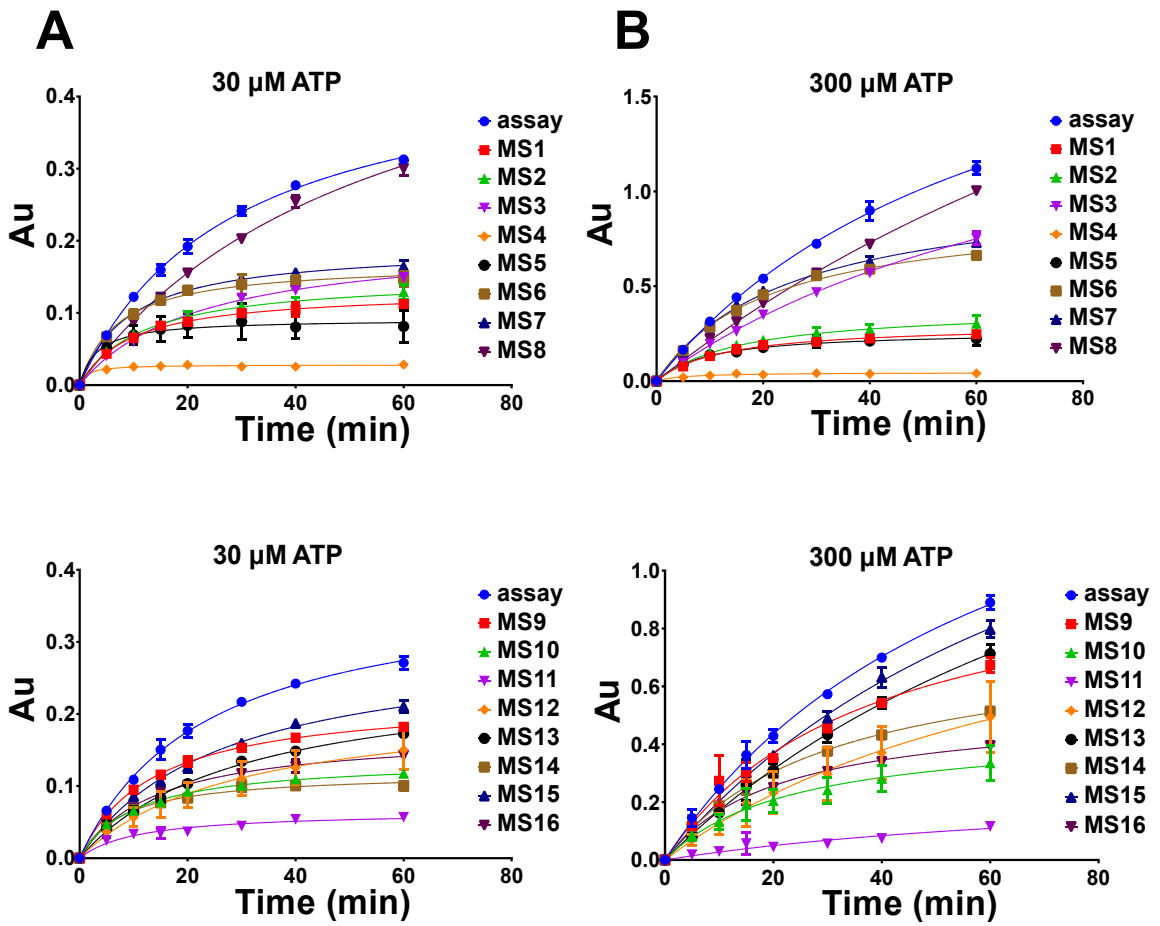

Figure 43: Saturation Kinetics. 1 h enzymatic time course at 30 µM ATP (A) and 300 µM ATP. (B). Assay conditions as described in Figure 41 done in the presence of 10 µM inhibitors. Assay (blue curve) defines the positive control. Data points are means of two independent experiments and the error bar signifies the standard deviation. When the standard deviation is smaller than the size of the data point, error bar is not displayed.

5.1.8.2. Validation of Drp1 activators

I then validated the activators of Drp1. To this end, I followed the same methodology as for EHD4 and performed first a MLG assay and then continued with a HPLC-based setup. Assay parameters for Drp1 were kept the same as for the IC_{50} determination, and a 2 h time course of enzyme kinetics (for malachite green assay) and an incubation time of 90 min (for HPLC measurements) was performed. In both assays, Drp1 showed an increased GTPase activity in the presence of MS4 and MS5 (Figure 44A and C).

Furthermore, I observed a similar increase in activity at 10-fold higher substrate concentration, e.g. at 600 µM GTP (Figure 44B).

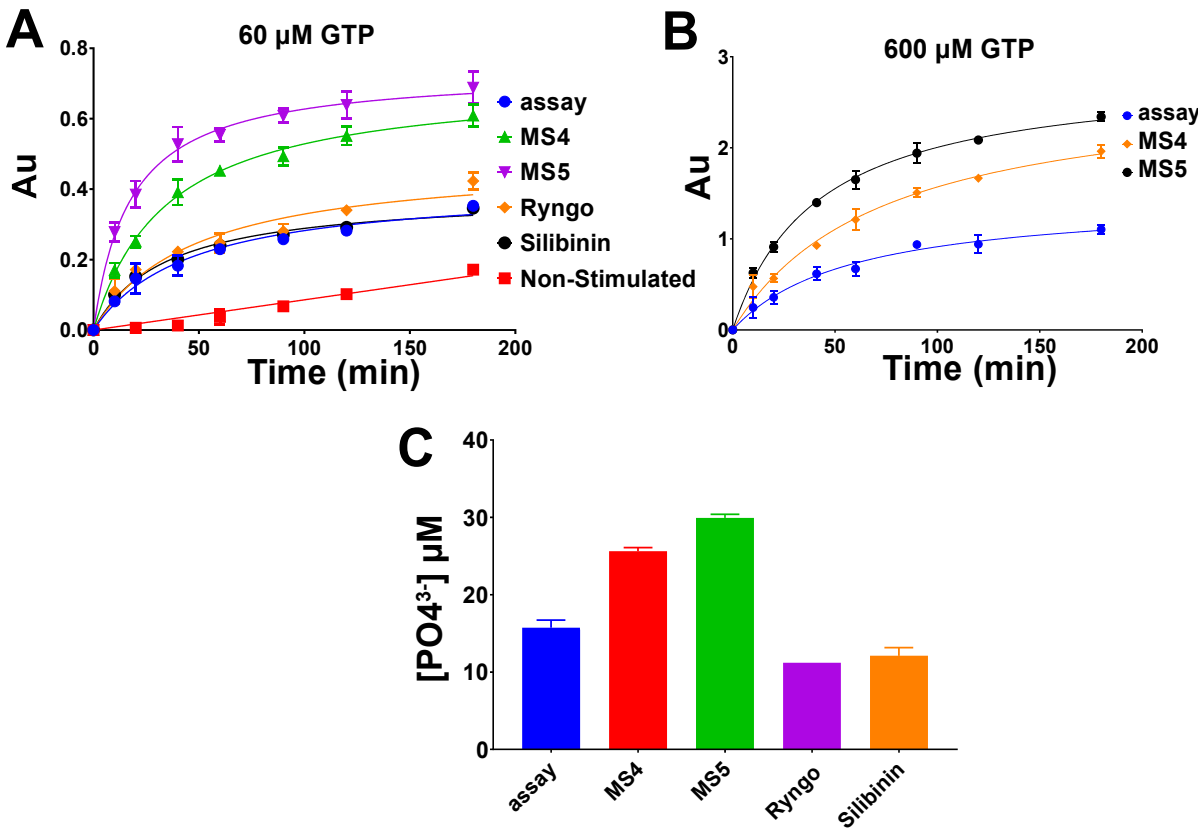

Figure 44: Validation assay for Drp1. A 2h time course of GTPase activity was done in the presence of 60 µM GTP substrate (A) or 600 µM GTP substrate (B). (C) Compounds were further validated in an HPLC-based setup. Assay (blue curve and bar) defines the positive control. The results show that MS4 and MS5 increase the stimulated GTPase activity for Drp1, while Ryngo and Silibinin do not show an effect on Drp1 stimulated GTPase activity. Assay parameters were, 300 nM Drp1, 60 µM GTP, 200 µg/ml DOPS at 25 °C. Data points are means of two independent experiments and the error bar signifies the standard deviation. When the standard deviation is smaller than the size of the data point, error bar is not displayed.

I also analyzed the effect of two described Dynamin modulators, Ryngo (or Ryngo 1-23) (Schiffer et al., 2015) and Silibinin (You et al., 2020) on the stimulated Drp1 activity. Ryngo and Silibinin however did not influence the stimulated GTPase activity for Drp1 (Figure 44A and C).

5.1.9. Analyzing the compounds for inhibition against EHD2

Having validated all the compounds as inhibitors for EHD4, I then checked them for inhibition towards the EHD2 protein. I first determined the K_m to choose the substrate concentration. The K_m for EHD2 is 99 (±8) µM (Figure 45A).

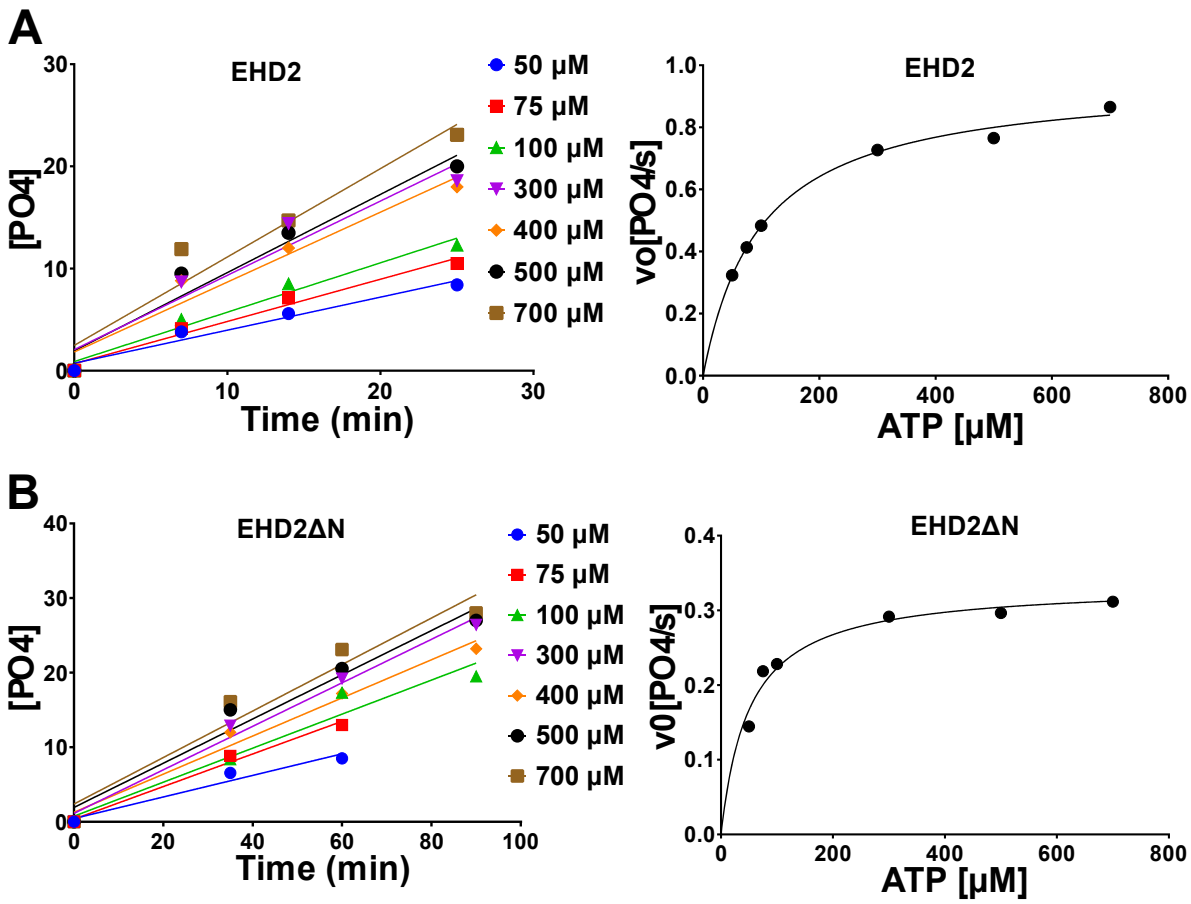

Figure 45: K_m determination for EHD2 protein. Kinetic parameters for EHD2 (A) and EHD2ΔN (B). Left panels shows the determination of initial velocities at different substrate concentrations. Right panels show K_m determination by plotting initial rate of the reaction vs. the substrate concentration. The following values were obtained: EHD2: K_m = (99±8) µM, k_{cat} = (0.096±0.003) 1/s, v_{max}-0.9579 µmoles/s. EHD2ΔN: K_m = (50±9) µM, k_{cat} = (0.034±0.001) 1/s, v_{max} = 0.3349 µmoles/s. Data points in left panel of A and B are means of two independent experiments and the error bar signifies the standard deviation. When the standard deviation is smaller than the size of the data point, error bar is not displayed.

The previously determined crystal structure of EHD2 (PDB: 4CID) showed that the N-terminus of EHD2 folds into a hydrophobic groove present in the GTPase domain. Truncation of the N-terminus led to increased membrane recruitment when expressed

in cells (Shah et al., 2014). To analyze whether a truncation of the N-terminus might result in a stronger ATPase activity, I also determined the K_m of an N-terminal truncated construct (EHD2ΔN), which is 50 (±9) µM (Figure 45B).

Comparing the catalytic efficiencies (k_{cat}/K_m) of the two constructs, I found that EHD2 is 1.5 times more active than EHD2ΔN ($9.7 * 10^{-4}$ /µM/s vs. $6.6 * 10^{-4}$ /µM/s). For this reason, I continued with EHD2 for the protein inhibition and characterization assays.

To check the inhibition for EHD2 protein, assay conditions in the HPLC-based setup were 5 µM EHD2, 50 µM ATP and 500 µg/ml Folch lipids in assay buffer. The incubation time was 100 min. As envisaged that due to the binding pocket being highly similar (see 5.1.5), eight of the inhibitors against EHD4 also inhibited the ATPase activity of EHD2 (Figure 46A/B and Figure 47). In contrast, three did not show an effect on EHD2 and can therefore be considered as specific for EHD4 (at least in relation to EHD2 and Drp1) (Figure 46B).

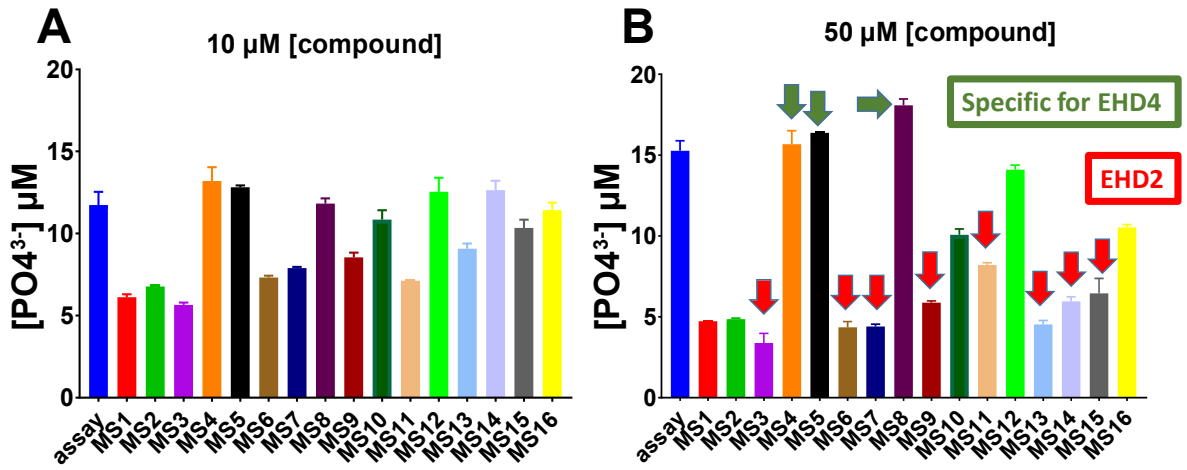

Figure 46: Identification of EHD2 inhibitors via HPLC based setup. Assay conditions were 5 µM EHD2, 50 µM ATP and 500 µg/ml Folch liposome in assay buffer. Incubation time was 100 min. Assays were done with 10 µM (A) or 50 µM (B) compounds. Compounds that showed inhibition at 10 µM also showed an increase in inhibition at 50 µM (red arrows) and were chosen for further analysis. Green arrows represents the inhibitors specific to EHD4. Data points are means of two independent experiments and the error bar signifies the standard deviation.

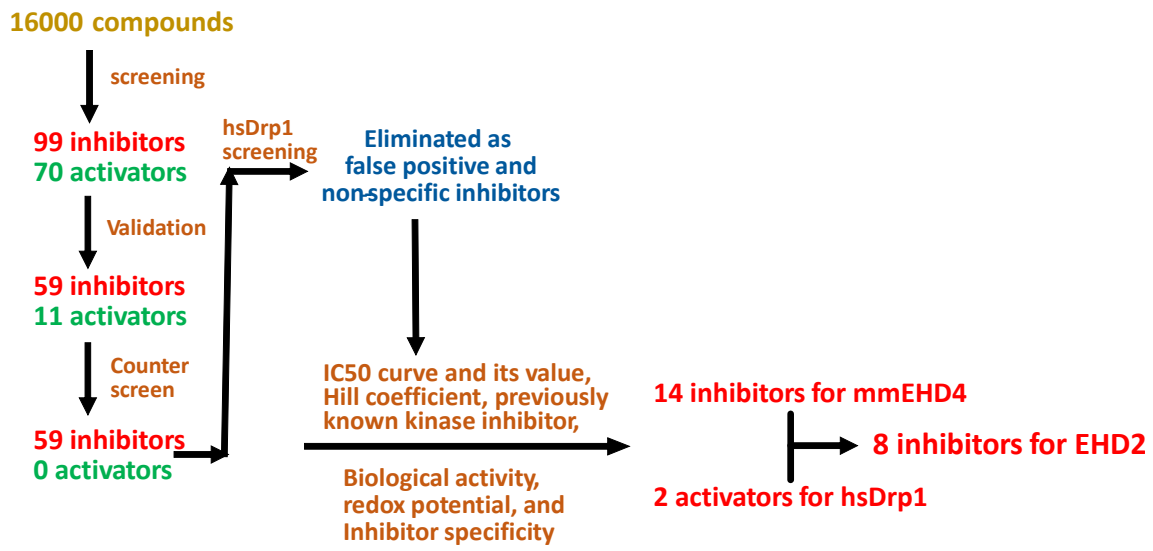

Figure 47: Final outcome of screening. A total of 8 inhibitors were found for EHD2 protein.

5.1.10. Binding assays

To biochemically characterize the interaction of the inhibitors to their respective protein; I sought to study their binding with Isothermal Titration Calorimetry (ITC). After several attempts and with all inhibitors and activators, I did not obtain any binding signal. One reason may be compound precipitation at a higher concentration in a low DMSO environment which was required for these assays. I therefore sought for alternative methods.

5.1.10.1. Thermal shift assay

Subsequently, I tested thermal shift assays (TSA) for studying the inhibitor binding. TSA results in a melting curve and provides the melting temperature (T_m) of the protein. I first tested three different protein concentrations (3 µM, 6 µM and 9 µM) to analyze the fluorescence readout and decide on an optimal protein concentration (Figure 48). Finally, 5 µM protein concentration was chosen because of the detectable fluorescence and to have a 1:10 ratio with the inhibitor at 50 µM. Liposomes could not be included in these assays, as they resulted in a high background signal. Moreover, with the gradual increase in temperature, liposomes disintegrate and EHDs would not be able to bind.

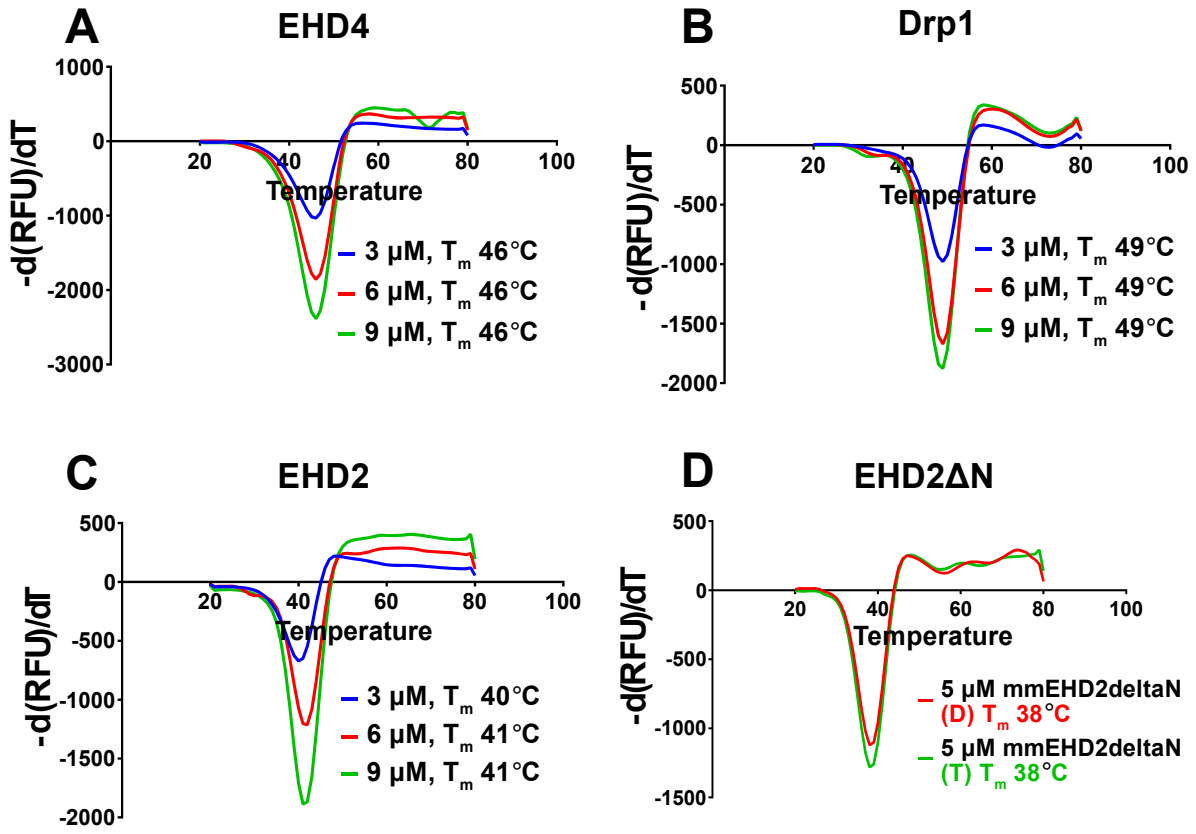

Figure 48: Melting temperature (T_m) of EHD4, Drp1, EHD2 and EHD2ΔN. (A-C) Fluorescence readout at three different protein concentrations (3 µM, 6 µM and 9 µM) were measured for the indicated proteins to determine the optimal protein concentration to be used in thermal shift assay. (A) EHD4, T_m = 46 °C. (B) Drp1, T_m = 49 °C (C) EHD2, T_m = 41 °C. (D) EHD2ΔN, T_m = 38 °C. D stands for dimeric peak whereas T stands for tetrameric peak (refer to Figure 18C).

Inhibitors MS1, MS2 and MS3 showed a large negative ΔT_m for EHD2, EHD2ΔN and Drp1 (Figure 49). It can be concluded that these three inhibitors lead to non-specific destabilization of the proteins.

Except MS4, MS8, MS14 and MS16, all inhibitors showed a reduced melting temperature for EHD4 (Figure 49A). Similar observations were made for EHD2, except for MS4 (Figure 49B). A possible explanation could be that the inhibitors are binding in the dimer interface leading to destabilization and hence reduced melting temperature is observed.

Except for the non-specific inhibitors MS1, MS2 and MS3, no other inhibitors for EHD protein had any effect on the stability of Drp1 (Figure 49C). This observation supports

the finding that inhibitors MS6-MS16 are specific towards EHD proteins. The T_m for Drp1 activators MS4 and MS5 remained the same (Figure 49C). However, close analysis of the fluorescence readout showed that there were two inflection points which may represent a second T_m of the protein (Figure 49D). It could be argued that in the presence of the activators, a conformational change induced in Drp1 may now lead to a different unfolding pathway.

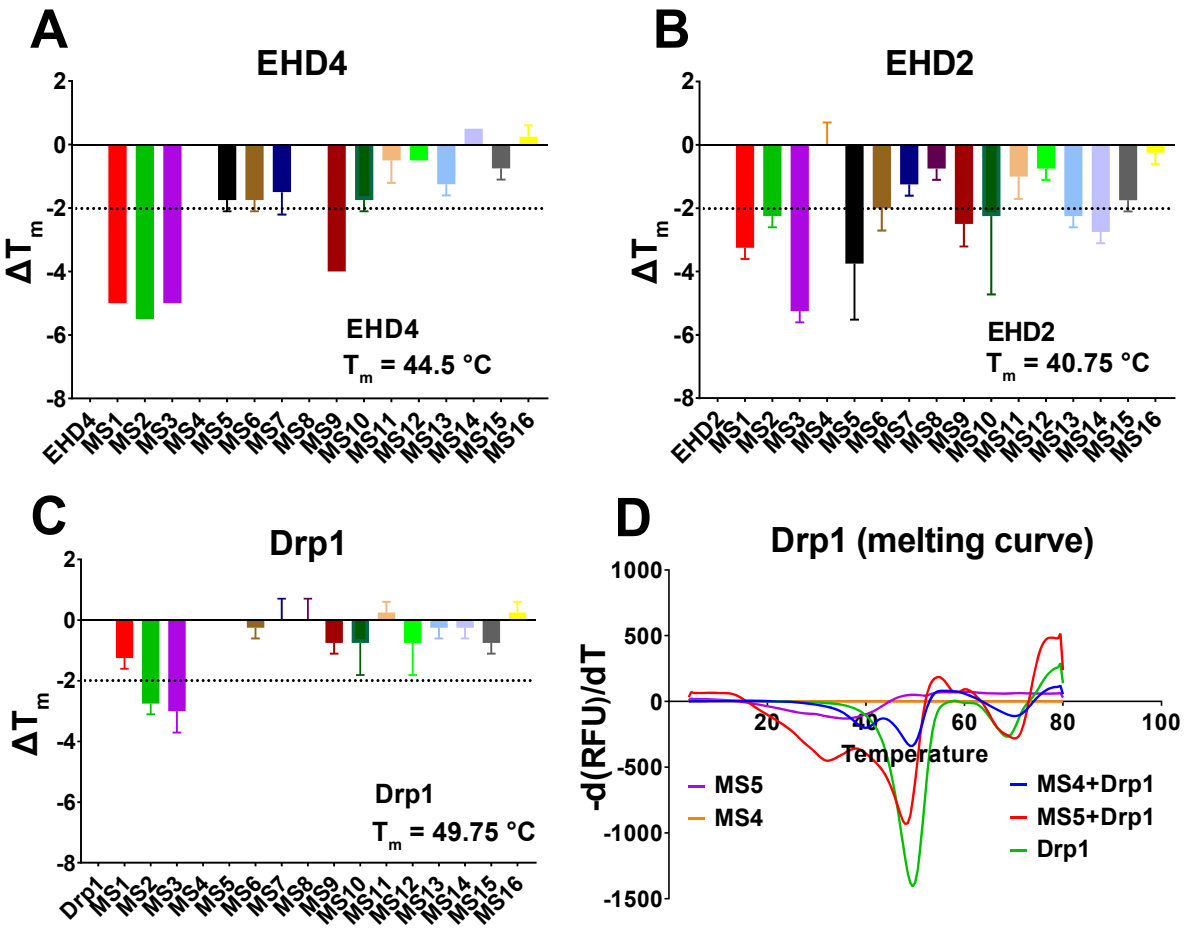

Figure 49: Thermal shift assay (TSA) for EHD4, EHD2 and Drp1. TSA of 5 µM EHD4 (A) EHD2 (B) and Drp1 (C) were studied in the presence of 50 µM compound. Changes in melting temperature (ΔT_m) were plotted against the compounds. (D) Melting curve for Drp1 in the presence of the two activators MS4 and MS5. Most of the compounds decreases the T_m of EHD2 and EHD4. Dotted line represents significant change of melting temperature (ΔT_m) ≥ 2 °C. Data points are means of two independent experiments and the error bar signifies the standard deviation. When the standard deviation is smaller than the size of the data point, error bar is not displayed.

5.1.11. *In-vivo* effect of the inhibitors in cellular lipid uptake

As EHD2 was shown to regulate cellular fatty acid uptake (Matthaeus et al., 2020), I wanted to study the effect of the EHD2 inhibitors (MS3, MS6, MS7, MS9, MS11, MS13, MS14 and MS15) for their effect on regulating fatty acid uptake. Initially, however, I addressed the cellular toxicity of the compounds, possible incubation times and the concentrations at which cell viability could be maintained.

5.1.11.1. Cytotoxicity assay

To follow my aims, I performed cytotoxicity assay. To this end, I employed the redox-sensitive dye resazurin, which is reduced by the mitochondrial respiratory chain to resorufin when it encounters a viable cell (Fields, 1996). This reduced product is detected by fluorescence readout (excitation: 570 nm and emission: 585 nm) in a plate reader, and the reading is directly proportional to the number of viable cells (McMillian et al., 2002). Resazurin itself is described to be non-toxic. It is therefore possible to add the dye and monitor cell viability over a period of time. Furthermore, it is also insensitive to interference by known drugs, serum and phenol red (Mershon et al., 1994; Page et al., 1993)

For my cellular assays, I decided to work on mouse embryonic fibroblast (MEF) from C57BL/6 mice and EHD2 KO MEFs derived from the corresponding mice (Matthaeus et al., 2020) .Two different cell lines (see 4.1.9) were used per genotype. MEF cells were grown as described in 4.2.4.1 and inhibitors were analyzed in cytotoxicity assays as described in section 4.2.4.2.

I incubated the inhibitors with the MEFs for 24 h at two different concentrations. Results in Figure 50 show that MS3 is highly toxic to the cells, whereas MS15 shows cellular toxicity only at a concentration of 50 µM (Figure 50). The remaining inhibitors did not show cellular toxicity at the given concentrations. Based on these analyses, I did not study MS3 in cell-based assays, MS15 was used at 10 µM, whereas the remaining inhibitors were used at 50 µM concentration.

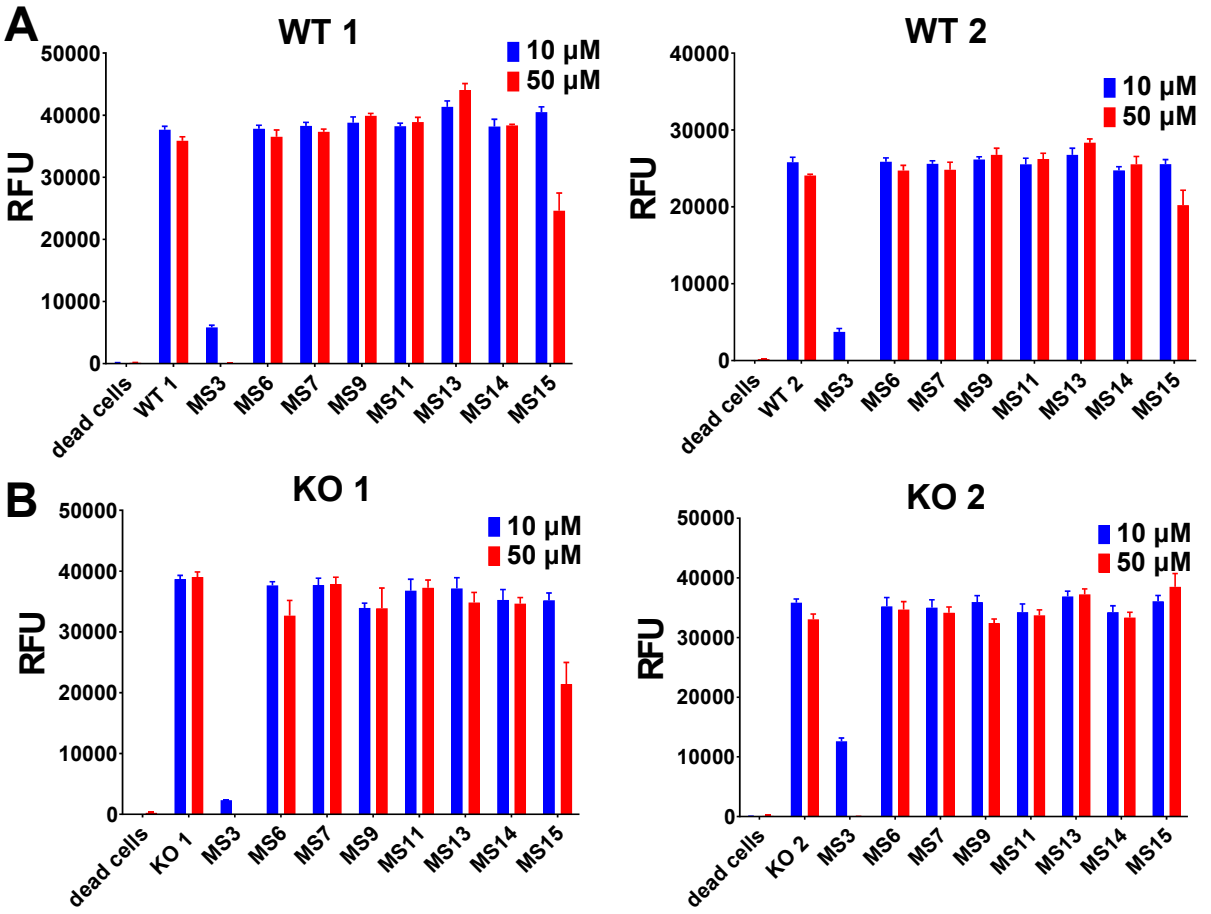

Figure 50: Cytotoxicity assay. Compounds at 10 µM and 50 µM, concentrations were incubated for 24 h with MEFs derived from two C57BL/6 WT (A) and EHD2 KO (B) mice, respectively and tested to check for their cellular cytotoxicity. As a positive control, 1% Triton X-100 was used to kill the cells (indicated as 'dead cells'). Data points are means of two independent experiments and the error bar signifies the standard deviation.

5.1.11.2. Lipid droplet assay

After identifying inhibitors for EHD2, I aimed to observe their *in-vivo* effect. For this, I analyzed lipid droplet size in two MEF cell lines (Matthaeus et al., 2020), to obtain a measure of caveolae mediated fatty acid uptake in the cell. Inhibitors having cellular effect are expected to show change in the lipid droplet size and their numbers.

After careful optimizations, I performed the lipid droplet assay in quadruplets (see 4.2.4.3 and Figure 51A), and 15-20 cells randomly chosen for every condition were quantified for statistical representation (see 4.2.4.5 and 4.2.4.6).

In control assays and as reported (Matthaeus et al., 2020), EHD2 KO MEFs showed an increased number and larger lipid droplets after oleic acid treatment compared to the WT (Figure 51B and C).

For the statistical analysis, I decided to plot the total lipid droplet area/cell (Figure 51F) to have the best comparison between the cell lines. For this analysis, individual lipid droplets were counted (Figure 51D) and their lipid droplet area was determined (Figure 51E) by a semi-automated script, which was developed together with Tim Abel (AG Sommer) (see 9.3. Appendix C). As can be seen in Figure 51F, this analysis confirmed previous data showing that EHD2 KO MEFs have an increased lipid uptake.

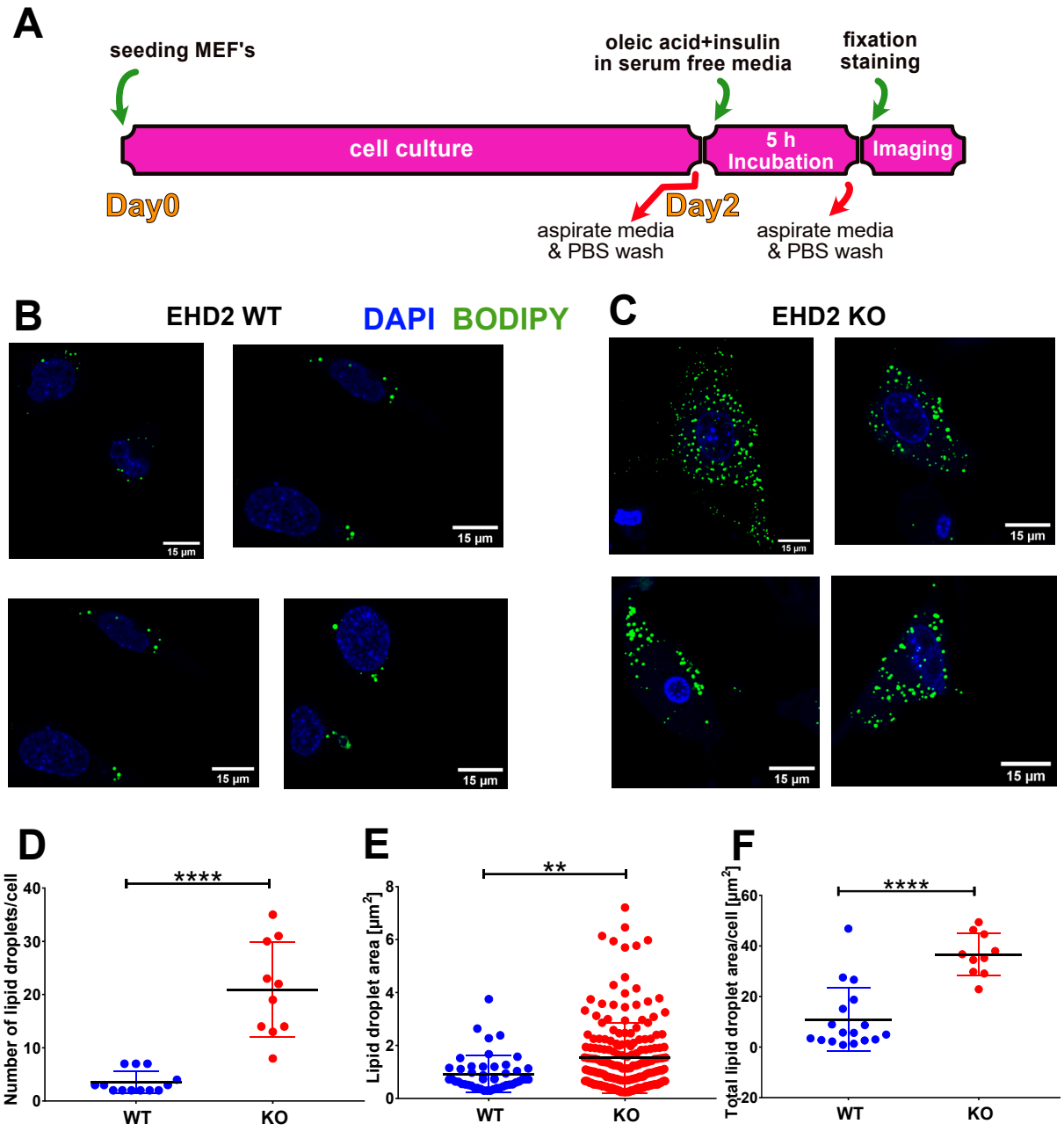

Figure 51: Lipid droplet assay. (A) Schematic representation of LPD assay protocol similar to (Matthaeus et al., 2020). (B) Representative images from WT MEF cells. (C) Representative images from EHD2 KO MEF cells. (D) The total number of lipid droplets in an individual cell was counted and plotted against the cell type. (E) Lipid droplet areas of individual lipid droplets were determined in about 20 representative cells and plotted against cell type. (F) Area of lipid droplet of an individual cell was summed up and plotted against the cell type. Nucleus and lipid droplet staining was done using DAPI and BODIPY, respectively. Statistical calculations were done using Graph pad prism version 7.05. Normality distribution test was done using D'Agostino-Pearson test. If the two sets of data were normally distributed, then unpaired t test (parametric) was applied, else Mann-Whitney test (non-parametric). Mann-Whitney test was also applied in the case, if one data set was normally distributed whereas the other not. Differences of $p \leq 0.05$ were considered significant ($p \leq 0.05$*, $p \leq 0.01$**, $p \leq 0.001$***, $p \leq 0.0001$****).

I then proceeded to analyze the effect of the EHD inhibitors in the lipid droplet assay. For this, I used the same protocol, but added the inhibitor at day 1 (Figure 52A). At day 2, during the incubation with oleic acid and insulin, the inhibitor was re-added to allow a constant exposure.

Results from the EHD2 KO MEFs show that, except for MS6 and MS7, all inhibitors had an effect on the lipid droplet size (Figure 52C). It can be concluded that the effect from these inhibitors does not depend on EHD2. Inhibitors MS6 and MS7 showed no effect on EHD2 KO MEFs whereas a marked effect was observed in WT MEFs (Figure 52B and C). MS6 showed reduced whereas MS7 an increase in total lipid droplet area in WT MEFs (Figure 52B). These results indicates that the inhibitors might indeed have an EHD2-specific effect to regulate caveolae-mediated fatty acid uptake.

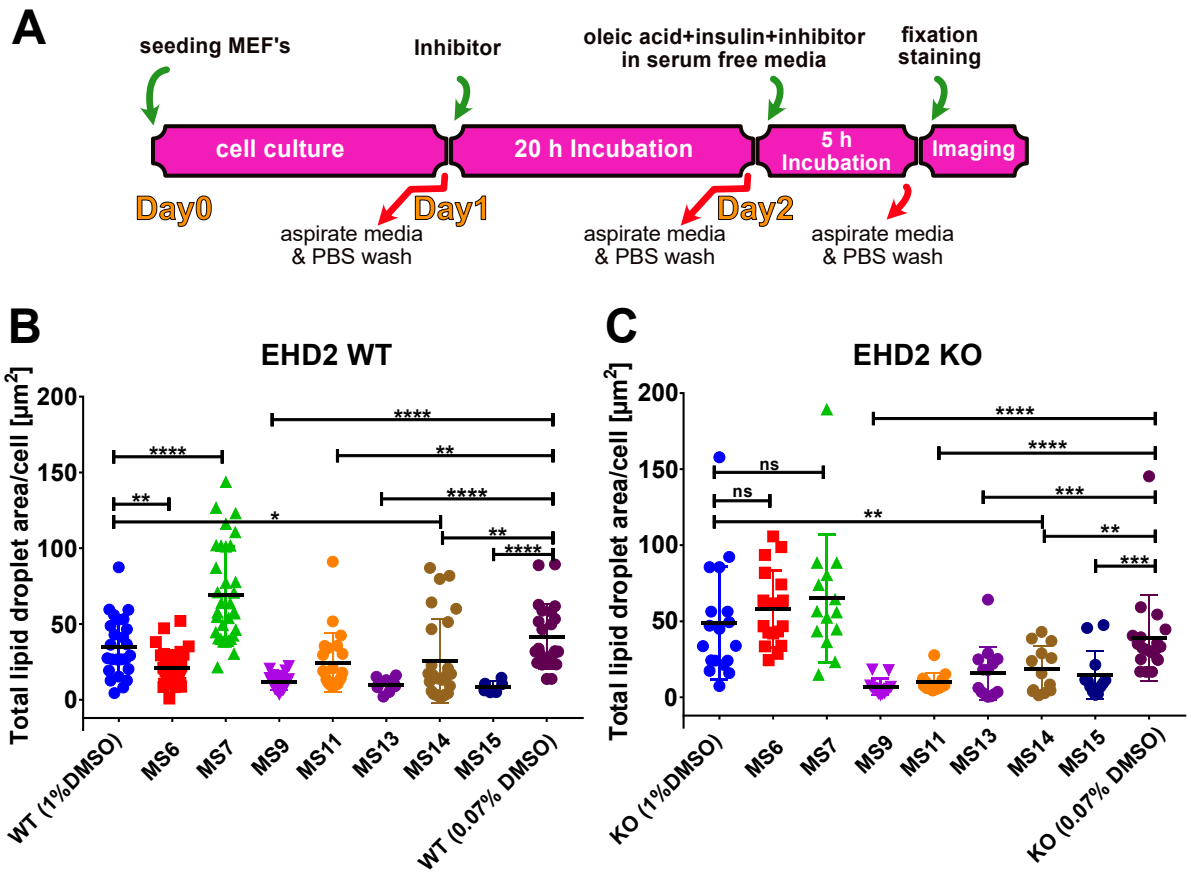

Figure 52: Lipid droplet assay with inhibitor. (A) Schematic representation of lipid droplet assay in the presence of the inhibitor. Incubation time of the inhibitor was 25 h. (B-C) Lipid droplet assay in the presence of the inhibitors in WT (B) or EHD2 KO cells (C). Statistical method and p-value representation is as in Figure 51.

To further validate the phenotypic effect of these two Inhibitors, the lipid droplet assay was done with a reduced incubation time of 20 h and the inhibitor was not added during the lipid uptake step (Figure 53A). Interestingly, under these conditions, the previously detected increased lipid droplet area in MEFs treated with MS7 was not observed any more (Figure 53B). In contrast, MS6 still showed a decreased lipid droplet area under these conditions (Figure 53B).

To substantiate the effect of inhibitor MS6, I repeated this experiment six times with different cryogenic stocks and at different passage number and analyzed around 50 cells for the experimental condition. Indeed, MS6 showed a reproducible decrease in lipid droplet area (Figure 53C).

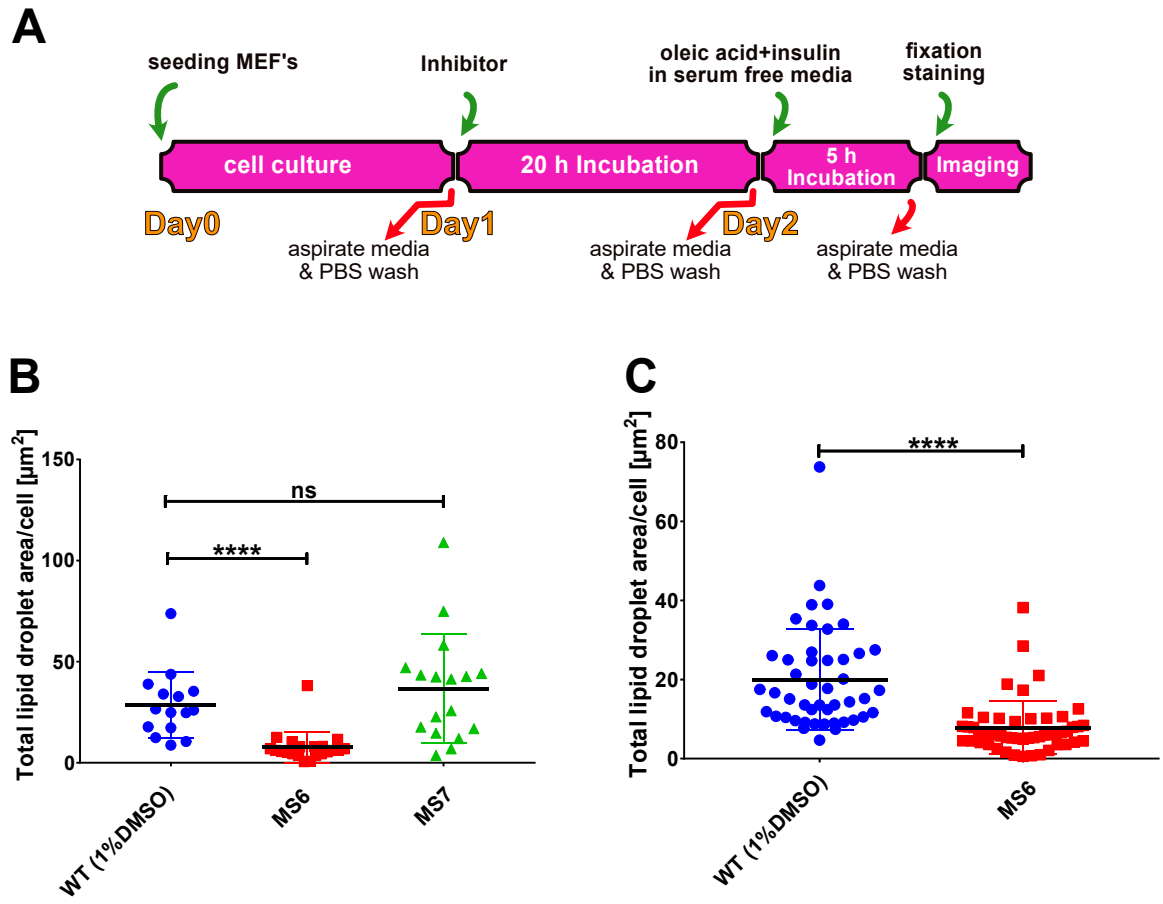

Figure 53: Lipid droplet assay with an alternative setup (A) Schematic representation of the adapted protocol. Here the inhibitor was not added during the incubation time with oleic acid and insulin. (B) Lipid droplet assay was performed with MS6 and MS7 with the modified protocol. (C) Verification of the phenotypic effect of inhibitor MS6 by repeating the experiment six times and analyzing around 50 cells in this experimental condition. Statistical method and p-value representation is as in Figure 51.

6. Discussion

Caveolae are bulb-shaped invagination of the plasma membrane shown to be involved in cellular fatty acid uptake. It is believed that EHD2 assembles into a ring-shaped oligomer around the neck of caveolae, thereby stabilizing them at the plasma membrane. Loss of EHD2 results in increased detachment of caveolae and an increase in cellular fatty acid uptake (Matthaeus et al., 2020). The same study also shows that EHD2 is important for caveolar mobility. To modulate EHD2 functional activity, I optimized a malachite green-based ATPase assay and performed a high throughput screening, targeting the ATPase activity of EHD4. In this way, I identified 59 compounds that inhibited the ATPase activity, 15 of them with IC_{50} values below 10 µM. These compounds were analyzed in detail and 8 of them also inhibited the closely related EHD2 ATPase. Furthermore, inhibitors MS6 and MS7 specifically target EHD2 in cellular assays and regulate caveolae mediated fatty acid uptake. MS6 shows a decrease whereas MS7 an increase in fatty acid uptake. Another interesting finding of this study was the identification of two GTPase activators of Drp1, a protein used as a control.

In the subsequent sections, I will discuss my findings and state important factors that played a crucial role in the development of the project.

6.1. Optimizing the enzymatic assay for EHD protein

A crucial aspect of this work was the optimization of the enzymatic assay targeting the liposome-stimulated ATPase activity of EHD4. As EHD2 ATPase activity could not be detected by the malachite-green based assay and also not by other commercially available assays, EHD4 was chosen as target. It shows at least a 10-fold increased ATPase activity compared to EHD2 and its activity could be detected in the malachite green based assay in a straight forward fashion. In order to design a robust, reproducible assay that could be taken to high throughput screening, I extensively optimized the relevant parameters, as discussed below.

6.1.1. Synthetic lipids

A crucial factor for obtaining a reproducible EHD enzymatic assay was the choice of the lipids. Assays done with different batches of natural extracts of PS resulted in highly variable ATPase activities (Figure 24). The chemical composition of a natural extract will always vary from batch to batch, and it may include trace amounts of other lipids that could affect the read out of the malachite green based assay. To avoid this variability, I explored the use of defined, chemically synthesized PS lipids.

Analysis of the chemical composition of naturally extracted brain PS by the supplier showed that 18:0 or 18:1 lipid were the main components of this mix (Figure 54A). I therefore tested these in their chemically synthesized form (Figure 54B and C). 18:1 synthetic PS, commercially known as DOPS, was further used in the assays because similar enzymatic activities were observed compared to other synthetic PS (Figure 25A) and it was 3X cheaper.

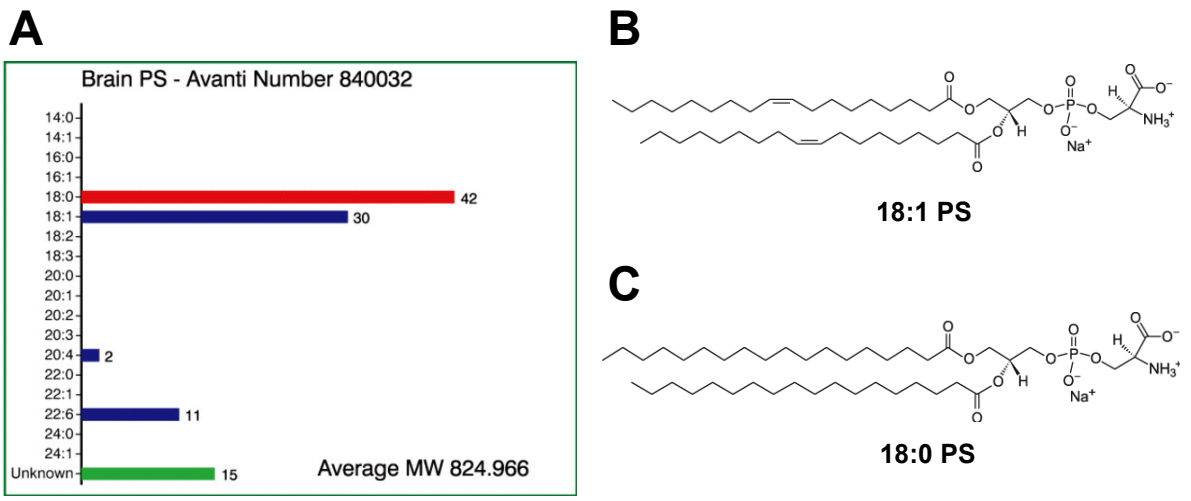

Figure 54: PS lipids (A) Percent composition of individual components from Brain PS, which is a natural extract from an animal brain. (B) Chemical structure of 18:1 synthetic PS. commercially known as DOPS. This was further used in the assay. (C) Chemical structure of 18:0 synthetic PS. 18 stands for the number of carbon atoms in each chain and the succeeding numeric digit stands for the number of saturation present in each chain. Figure adapted from (Avanti; Sigma).

DOPS, has similar properties to naturally occurring brain PS, which makes it an excellent substitute. It is also more stable to oxidation. DOPS have been used in drug

discovery studies, as a component of lipid mixtures to mimic the plasma membrane (Zhang et al., 2019), in liposome preparation for anti-tumor (Pahl et al., 2014) and amyloidosis studies (Goodchild et al., 2014). They are also used in drug delivery (Lipa-Castro et al., 2021; Zarif, 2002) and as nano complexes for gene delivery application in cancer vaccines (Beg et al., 2021). However, to the best of my knowledge, there has been no report specifically mentioning the use of synthetic lipids for dynamin superfamily drug screening. Dynasore, inhibitor for dynamin, was found through drug screening where the authors used Grb2 (an SH3 domain containing protein) to stimulate its GTPase activity (Macia et al., 2006). For the identification of other dynamin modulators, brain PS in high throughput screening (Gordon et al., 2013; Hill et al., 2005).and Phosphatidylinositol 4,5-bisphosphate lipid in comparing the previously known dynamin inhibitors on the stimulated dynamin enzymatic activity in the drug screenings were used (Mohanakrishnan et al., 2017).

6.1.2. Role of cations in nucleotide activity

Another crucial factor was the inclusion of potassium ions (K^+) in the assay. The role of K^+ and Magnesium ions (Mg^{2+}) in modifying the plasmalemma ATPase activity of grapevines was shown as early as in 1988 (Varanini, 1988). Crystallographic studies on dynamin have shown that K^+ mimics the function of an arginine finger (Chappie et al., 2010). Such arginine fingers contribute to nucleotide hydrolysis by stabilizing the transition state of GTP hydrolysis and positioning a water molecule to perform the nucleophilic attack and/or mediate nucleotide polarization (Nagy et al., 2016; Ren et al., 2007). Mutational studies have shown that replacing the arginine finger diminishes the catalytic rate while the P-loop structural integrity still remains (Ahmadian et al., 1997; Yukawa et al., 2015). Sodium ions (Na^+) can replace potassium only inefficiently in dynamin (Chappie et al., 2010). Furthermore, a serine residue at the 4^{th} position of the P loop in dynamin was shown to contact the potassium and be crucial for binding (Chappie et al., 2010). This serine is also highly conserved in the EHD family, pointing to a related function.

In my assay, inclusion of 150 mM potassium, which is physiological salt concentration led to increase of ATPase activity. The use of K^+ in stimulating enzymatic activity of dynamin proteins (Chappie et al., 2010; Frohlich et al., 2013; Warnock. et al., 1996)

(also Figure 29) including EHD proteins (Daumke et al., 2007) have been shown previously. Initial drug screening for development of dynamin inhibitors have used Na^+ (Hill et al., 2005) whereas later drug screenings leading to the identification of dynasore and new lead compounds have used K^+ (Macia et al., 2006; Mohanakrishnan et al., 2017). Other monovalent cations from the alkali metal series were also tested in previous biochemical studies (Chappie et al., 2010). However it is clear that potassium had the most efficient effect on the stimulated enzymatic activity (Figure 29).

Mg^{2+} coordinates ATP and water molecules and nucleotide binding in EHD proteins is dependent on Mg^{2+} (Daumke et al., 2007). In dynamins, the bound Mg^{2+} forms a hydrogen bond to the β-phosphate and stabilizes the developing charge during the transition state of GTP hydrolysis (Chappie et al., 2010). In Ras GTPases, Mg^{2+} provides a temporary storage of the electrons from the triphosphate and/or surroundings. The electron shift is reversed after bond cleavage and the release of inorganic phosphate (Rudack et al., 2012). Including Mg^{2+} (0.5 mM) in my assay, however, did not increase the enzymatic activity of EHD2 (Figure 29C). Possibly, the inclusion of 2 mM $MgCl_2$ in the final protein purification buffer, corresponding to ~50 µM $MgCl_2$ in the reaction is sufficient to reach the maximal ATP activity. However, higher concentration of Mg^{2+} (4 mM) resulted in a decrease of the enzymatic activity (data not shown). Mg^{2+} is well known to lead to the clustering of the negatively charged lipid head groups such as that of PS (Bradley et al., 2020; Laudadio et al., 2018) and may thus interfere with liposome integrity.

Among other divalent cations, manganese ions (Mn^{2+}) though at a lower level compared to Mg^{2+}, showed an increase in ATPase activity of plasmalemma ATPase whereas Zn^{2+} and Ca^{2+} were almost without any effect (Varanini, 1988). Mn^{2+} are also crucial in enzymatic activity of metal dependent protein phosphatases. Mn^{2+} could have been possibly explored for its role in stimulated EHD ATPase activity but the three-fold increased rate in the presence of K^+ was sufficient for a higher readout. Moreover, Mg^{2+} has been used in almost all the enzymatic assay for dynamin superfamily of proteins previously reported (Chappie et al., 2010; Daumke et al., 2007; Melo et al., 2017). as well as in dynamin drug screening (Hill et al., 2005; Hill et al., 2004; Macia et al., 2006; Mohanakrishnan et al., 2017). Therefore, the role of Mn^{2+} was not explored in the EHD ATPase activity.

6.1.3. Substrate concentration for HTS

I chose the substrate concentration depending on the K_m of EHD4 for the high throughput screening. Competitive inhibitors target the substrate binding pocket (Figure 55A). The sensitivity to find a competitive inhibitor increases when the substrate concentration is lower. Thus, at a high substrate concentration, low affinity competitive inhibitors may be missed during the screening. Non-competitive inhibitors bind to the enzyme, usually in a pocket different from the catalytic site, irrespective of whether the enzyme has substrate bound or not (Figure 55B). Potency of inhibition in this case is independent of the substrate concentration. Uncompetitive inhibitors bind to the enzyme-substrate complex (Figure 55C). Potency of inhibition increases as the substrate concentration increases. Therefore, keeping the substrate concentration higher maximizes the sensitivity for finding weak, uncompetitive inhibitor (Copeland, 2005).

To keep a balance for finding all three types of inhibitors, I kept the substrate concentration near the K_m.

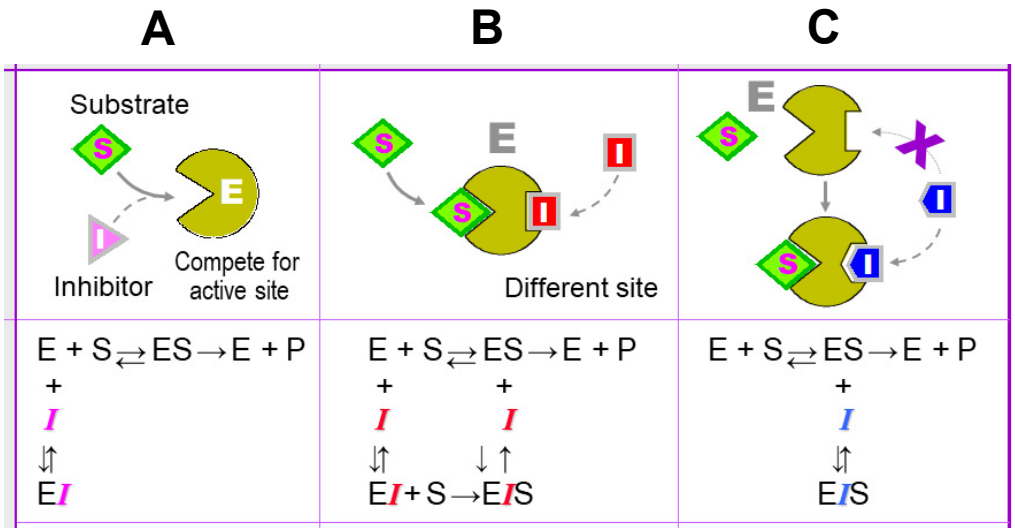

Figure 55: Schematic representation of different types of inhibitors. Upper panel shows cartoon representation and the lower panel shows a representative equation. (A) Competitive inhibitor (B) Non-competitive. (C) Uncompetitive. E: enzyme, I: inhibitor, S: substrate, P: product, ES: enzyme-substrate complex. Figure taken from (Juang, 2004).

Lower substrate concentration compared to K_m have been used in drug screening to find highly selective inhibitors for the Ser/Thr metal dependent phosphatase PPM1F (K_m= 1.32 mM, substrate concentration= 1 mM) (Grimm et al., 2020; Grimm et al., 2022) and DNA methyltransferase enzyme, DNMT1 (K_m= 0.3-1.3 µM, substrate concentration = 0.2 µM) (Pappalardi et al., 2021; Pradhan et al., 1999).

However, in different dynamin drug screenings, substrate concentrations a few fold higher (200-300 µM) compared to the K_m (50 µM) have been used (Gordon et al., 2013; Hill et al., 2005; Hill et al., 2009; Macia et al., 2006) (Macia et al., 2006). Likely, for a higher readout (SNR ≥ 2), more substrate was required. Similarly, in my case, I had to use a slightly higher substrate concentration (30 µM) than the K_m (20 µM) to have SNR ≥ 2. This, however, may not be too detrimental for my screen, unless the substrate concentration is multiple folds higher leading to inhibitors being dislodged from the binding pocket (as done in saturation kinetics Figure 43).

6.1.4. Incubation time for ATP hydrolysis in HTS

Typical enzymatic reactions are linear in the initial phases and inhibition is best observed during this time. As the reaction progresses and reaches saturation, differences in catalytic activity may be vanishing.

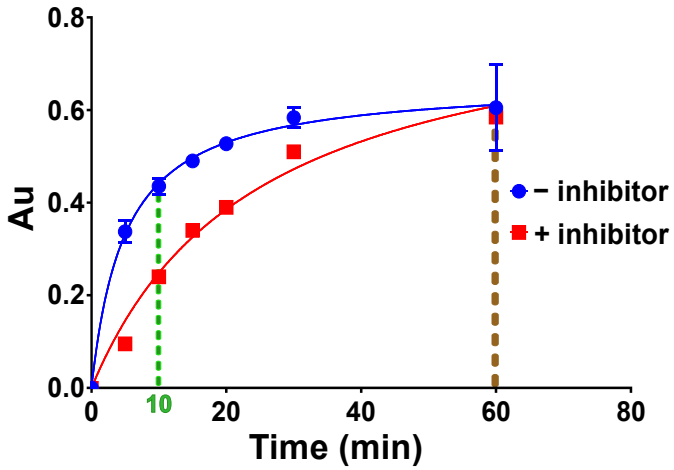

Figure 56: Finding the best incubation time. Enzymatic activity in the absence and presence of inhibitors. While at earlier time points (e.g. 10 min), a marked difference in catalytic activity can be observed in the presence of an inhibitor, but the difference reduces and finally vanishes at later time points (e.g. 60 min).

This is best explained by comparing the reaction without an inhibitor in Figure 56 to the inhibited reaction at the 10 and 60 min time point. Even potent inhibitors eventually reach the saturation point.

For my screens with EHD2 and EHD4, I thus adapted the reactions to measure inhibition for the early time points of the reaction when the substrate was not limiting.

Incubation time within linear enzymatic range is a conventional rule followed mostly in drug screening. All the different dynamin drug screening was done at 30 min incubation time (Gordon et al., 2013; Hill et al., 2005; Hill et al., 2009; Macia et al., 2006). Some recent discoveries of inhibitors having a similar approach are, the compound GSK3685032 (40 min) (Pappalardi et al., 2021) and the compound Lockdown (30 min) (Grimm et al., 2022) against their target proteins.

6.2. Selection criteria for compounds

The following criteria were applied to further select validated hits:

1) Compounds that showed inhibition to EHD4 and Drp1 were excluded. An example of such a compound's IC_{50} curve is shown in Figure 57A.

2) Compounds having less than 25% inhibition between the left and the right asymptote in the IC_{50} curves were eliminated as weak inhibitors (Figure 57B).

3) A sudden and steep drop in IC_{50} curve (Figure 57C) would likely represent the compound forming aggregates and sequestering the enzyme. This can happen when the enzyme associates with the surface of the aggregates (McGovern et al., 2002; McGovern et al., 2003).

4) Mass spectrometry-based data had suggested that some compounds had degraded over time. Similarly, spiro compounds (bi- or polycyclic organic compounds with the rings connected through one common atom) (Acosta-Quiroga et al., 2021) were excluded from further analysis as they have a higher propensity of degradation.

5) For the identified compound structures, an Extended-Connectivity Finger Print (ECFP) was generated (Rogers & Hahn, 2010). ECFP are circular topological

fingerprints designed for molecular characterizations, similarity searches and structure activity modeling. These fingerprints among the compounds were compared by Tanimoto similarity coefficients (T=1 highest similarity, T=0 no similarity). Compounds showing Tanimoto similarity > 0,6 were grouped as similar (Bajusz et al., 2015). The most active compounds from such group were selected depending on the IC_{50} values.

6) Thiol-containing compounds were not considered as they are prone to oxidation.

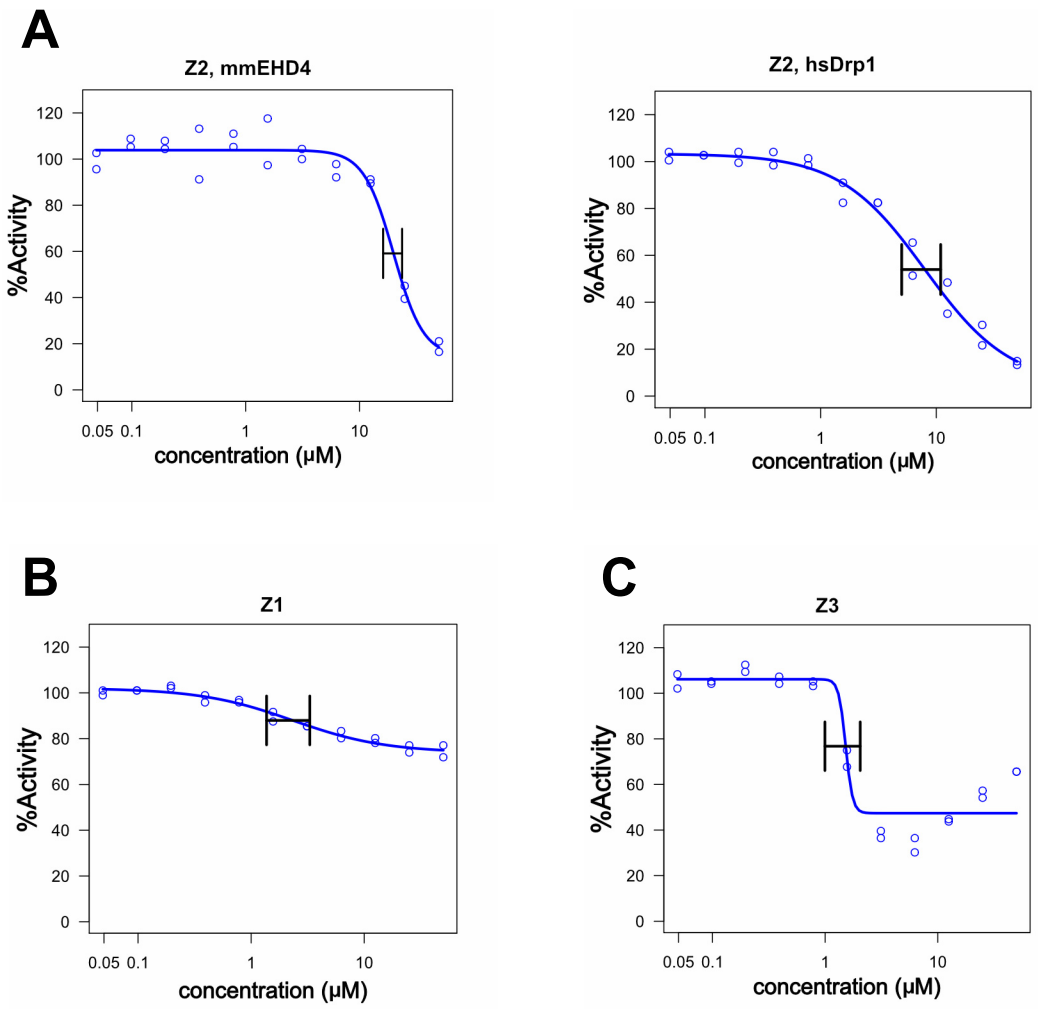

Figure 57: Compound selection based on analyzing their IC_{50} curves. (A) Compounds showing inhibition towards EHD4 and Drp1 were not further pursued. Left panel shows compound Z2 inhibiting EHD4 and right panel shows the same compound inhibiting Drp1. (B) Compound Z1 inhibiting EHD4 does not show a strong maximal inhibition although the IC_{50} value is in the low µM range. (C) A sudden and steep slope in the IC_{50} curves point to compound aggregation that may precipitate the protein along with it. This results in inhibition of the enzymatic activity but rather in an unspecific fashion.

7) Compounds that can form covalent bonds (Michael acceptors) usually have broad spectrum bio-activities (Baell & Walters, 2014; Baell & Holloway, 2010), as they bind non-specifically to proteins inside the cell. For this non-desired trait, they were also not selected for further evaluation.

8) A substructure filter search for identifying Pan Assay Interference Compounds (PAINS) was performed (Baell & Holloway, 2010; Dahlin & Walters, 2016; Yang et al., 2016). The identified structures elucidate potentially unfavorable structural properties that may render the compound to be a frequent hitter. Such compounds were not considered as well.

9) Compounds showing a high number of reported biological activities in the ChEMBL database (Gaulton et al., 2012) were also not followed up.

Keeping these criteria in mind, we chose 16 inhibitors for EHD4.

Work done from Shoichet lab (University of California, San Francisco) on colloidal aggregation in drug discovery and drug information (Duan et al., 2017; Irwin et al., 2015; McGovern et al., 2002; McGovern et al., 2003) has shown similar approach regarding eliminating false positives from IC_{50} curves and also helped me in eliminating non-specific inhibitors. PAINS analysis is a common method adopted in many drug screenings, e.g. (Grimm et al., 2022; Mohanakrishnan et al., 2017) to eliminate compounds that are frequent hitter.

Spiro compounds are gaining significant interest in medicinal chemistry due to their inherent three-dimensionality and structural novelty (Acosta-Quiroga et al., 2021; Zheng et al., 2014) but they also have a higher propensity of degradation overtime. This could be the case in a frequently used but long stored drug library, some spiro compounds were already found degraded in the LC-MS experiments and were eliminated. A future aspect could be to synthesize spiro compounds from the molecular scaffold of the chemical hit to have drug-like properties and specificity.

Similar approach to eliminate Michael acceptors that can form covalent bonds leading to non-specific effects in cellular assays were previously shown (Grimm et al., 2022).

I could have counter-screened against more members from the dynamin superfamily in my validation assays as done while identifying the compound AS-99 against histone

methyl transferase (ASH1L) (Rogawski et al., 2021). However, the final inhibitors did not show any inhibition towards Drp1 as such further members of dynamin superfamily of proteins were not tested.

6.3. Developing an EHD specific inhibitor

I adopted a strategy to detour from the conventional method of screening the target protein EHD2 directly but screening instead against another protein from the same family (in this case EHD4). Since both proteins are highly conserved in the catalytic site, this raised questions about the inhibitor specificity. A common inhibitor binding to all four EHDs would have pleiotropic effects when applied to a cell. Analysis of the cellular function of such inhibitor may be difficult. Such a trait would also not be desirable in drug discovery studies.

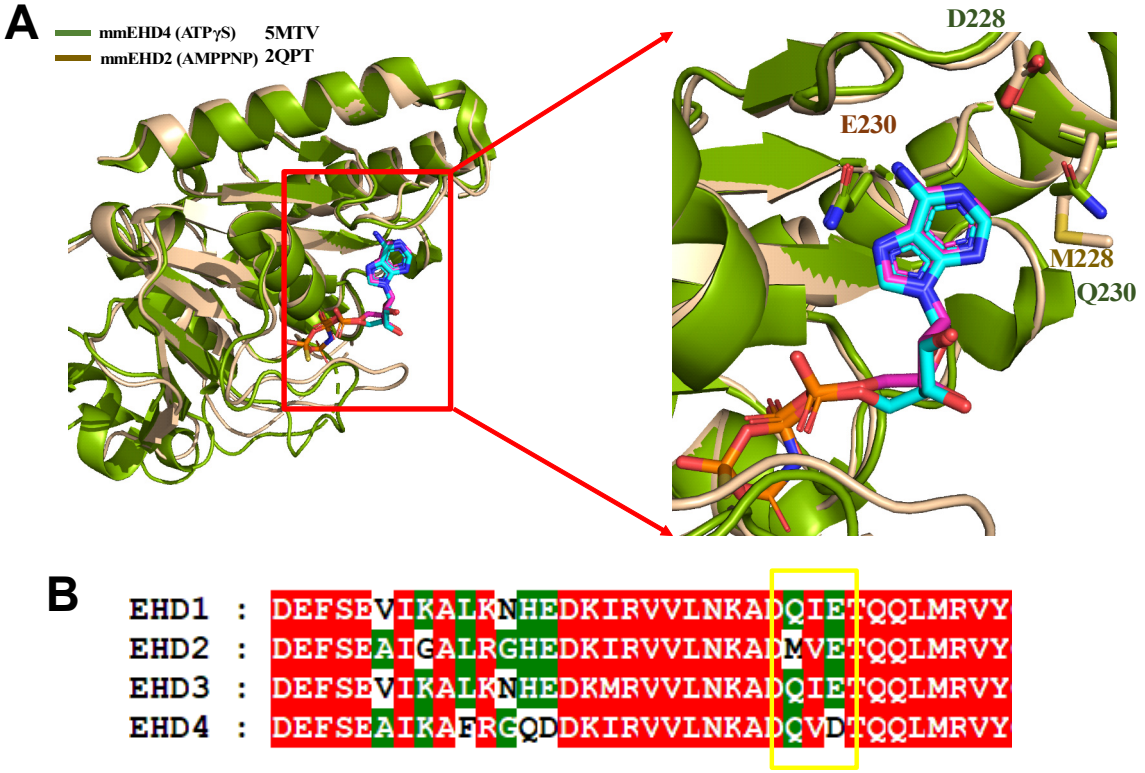

Figure 58: Residue difference in EHD2 and EHD4. Targeting these residues could address inhibitor specificity. (A) Left panel shows the structural alignment of the catalytic active site of EHD2 (PDB: 2QPT) and EHD4 (PDB: 5MTV). Inset (left panel) highlights the different residues in the binding pocket. (B) Part of sequence alignment of all the EHDs showing amino acid difference between EHD2 and EHD4 next to the G4 motif (T/NKxD) shown by the yellow rectangular panel.

To analyze inhibitor specificity, I performed a structural alignment for the active site of EHD2 and EHD4. The binding pockets superimpose well with each other showing no major structural differences (root mean square deviation of 0.75 Å for 1219 aligned Cα-atoms, see Figure 58A, left panel). However, a closer observation reveals that there are two amino acids different in the binding pocket (Figure 58A, right panel). In EHD2, there is a methionine and glutamic acid at residues 228 and 230, whereas the corresponding position in EHD4 carries an aspartic acid and a glutamine. Sequence alignment shows that one of the amino acids is just next to G4 motif (Figure 58B).

These amino acid exchanges could help to chemically synthesize specific drug molecules by structure-based modification of the compounds. This assumption is reinforced by the fact that three of the identified compounds inhibited EHD4 but had no effect on the enzymatic activity of EHD2 (see Figure 46).

Structure guided approaches have been used in previous drug screenings to obtain specific inhibitors for protein isoforms. A closely related example is that of protein kinase Akt, which has three isoforms sharing a high overall sequence similarity particularly within the conserved kinase domain (Quambusch et al., 2021). The authors have used X-ray crystallography studies and structure-based ligand design to develop isoform selective Akt inhibitors (Quambusch et al., 2021; Quambusch et al., 2019). A recent approach, of modulating the substituent chemical groups leading to an incremental size increase of the ligand until the molecule can no longer fit to an isoform, has helped in developing highly selective compounds targeting carbonic anhydrase (Dudutienė et al., 2020). Carbonic anhydrase consists of a family of 12 isoforms where the active pocket is highly similar (McKenna & Frost, 2014). Here the authors, designed a series of homologous compounds with different substituent groups, supported by molecular docking and crystallographic analysis. This approach led to the development of highly specific inhibitors against two isoforms of carbonic anhydrase which are anti-cancer and anti-obesity targets (Dudutienė et al., 2020).

Larger drug libraries containing diverse chemical compounds can be screened which could result in finding allosteric inhibitors targeting N or C-terminal domain. This approach could possibly help in finding inhibitors targeting specifically EHD1 and EHD3. Specific inhibitors have been developed for the family members of metal dependent phosphatases which are highly conserved in their catalytic site by targeting

the flanking regions of the catalytic core (Gilmartin et al., 2014; Grimm et al., 2022; Tagad et al., 2018).

A combined approach of high throughput screening and structure-guided drug design could result in a highly selective potent molecule having drug-like properties, e.g. as the discovery of potent inhibitors against leukemia (Pappalardi et al., 2021; Rogawski et al., 2021).

6.4. Regulation of fatty acid uptake with EHD2 inhibitors

How could an inhibitor targeting EHD2 interfere with fatty acid uptake? There would be two obvious possibilities (Figure 59).

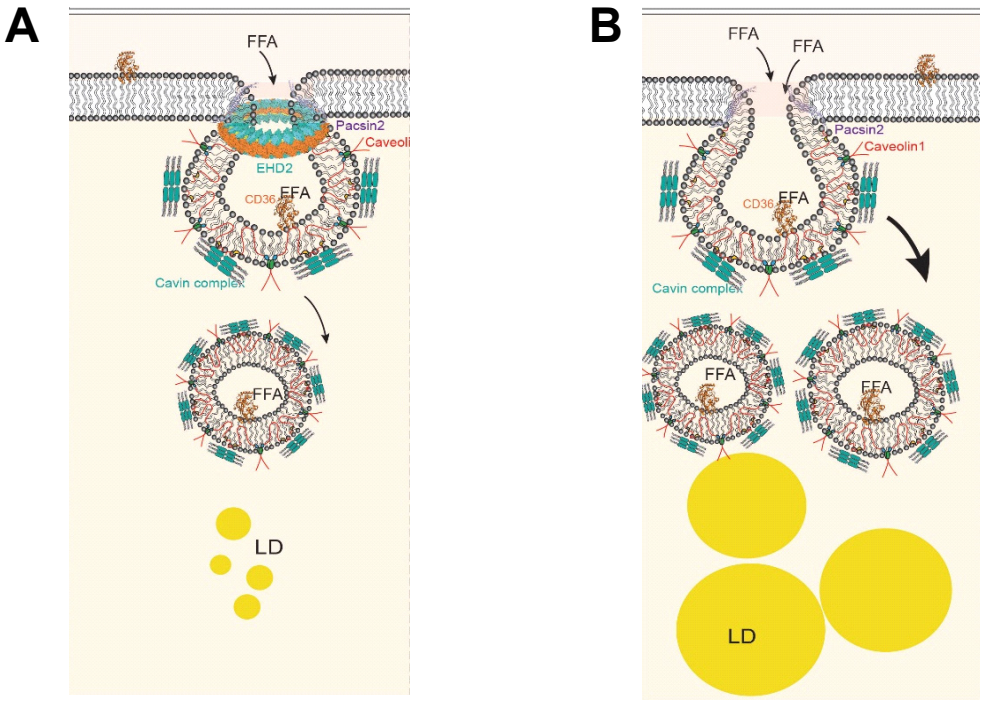

Figure 59: Working hypothesis for the action of EHD2 inhibitors. EHD2 ring formation at the neck of caveolae is depicted. The stability of the EHD2 ring could be modulated by inhibitor binding, which would, accordingly, regulate cellular fatty acid uptake. (A) An inhibitor that promotes oligomerization can lead to reduced fatty acid uptake in the cell. (B) In an alternative scenario, the inhibitor disrupts the oligomerization process leading to increase in fatty acid uptake in cells. LD- lipid droplet, FFA- free fatty acid, CD36- fatty acid translocase. Figure adapted from (Matthaeus et al., 2020).

Potential compounds could bind to the active site by displacing ATP from the pocket. In such a case, the compounds may increase the ATPase activity by stimulating the assembly or interfere with ATP-dependent oligomerization. One scenario could lead to increased stability of EHD2 oligomer, reducing caveolar mobility and therefore decreased fatty acid uptake (Figure 59A) while the second scenario would lead to ring-disassembly and therefore increased fatty acid uptake (Figure 59B). In a similar fashion, the compound may bind at a different position from the catalytic active site and thereby stabilize or destabilize oligomer formation.

I performed cell-based assays for the quantification of lipid droplet number and size as a measure of cellular fatty acid uptake. Two inhibitors, MS6 and MS7, altered the total lipid droplet area in the cell in an EHD2-dependent fashion, pointing towards a modification of caveolae-mediated cellular fatty acid uptake (Figure 52). Importantly, lipid droplet assays with a shorter incubation time, without including the inhibitor during fatty acid uptake, confirmed the potency of MS6 (Figure 53). In contrast, MEFs treated with MS7 did not show increased fatty acid uptake in this setup, which may point to a reversible action of the inhibitor (Figure 53).

It is intriguing to see that the inhibitors give opposite phenotypic effects in the cell-based assays, while the saturation kinetics indicates that both inhibitors are competitive. Thermal shift assays for these inhibitors show a decrease in the melting temperature of EHD2 and EHD4. This suggests that the inhibitors destabilize the protein. In the absence of any structural data for inhibitor binding, one could speculate that the inhibitor is binding at the dimer interface leading to weakening of dimer formation. This may destabilize the EHD2 oligomer, which would result in faster detachment of caveolae and increased fatty acid uptake. Future studies should address the consequences of inhibitor application for EHD2 oligomer formation and caveolar mobility. This could be done by analyzing oligomer formation in negative-stain EM studies (as shown in Figure 19) and caveolar mobility in TIRF assay, as described in (Matthaeus et al., 2020).

6.5. Possible use of EHD4 inhibitors

Inhibitors against EHD4, particularly the three EHD4-specific inhibitors MS4, MS5 and MS8, could be useful tools for better understanding EHD4-mediated signaling

pathways. EHD4 (earlier know as Pincher) was discovered as a protein induced by nerve growth factor (NGF) and mediates cytoplasmic signaling of NGF through its receptor, TrkA (Tropomyosin receptor kinase A) (Shao et al., 2002). Other roles of EHD4 include internalization of the trans-membrane protein Nogo-A into neuronal cells by EHD4-mediated endocytosis. Nogo-A is expressed in the adult central nervous system (CNS), where it inhibits axonal growth, regeneration and plasticity (Joset et al., 2010). EHD4 along with EHD1 is also involved in the endocytosis of L1/neuron-glia cell adhesion molecule (NgCAM) in neurons. NgCAM is known to regulate axonal growth (Yap et al., 2010).

Most of the described EHD4 functions are in the nervous system, in line with its high expression in peripheral neurons and the brain, making it an attractive target for mediating retrograde endosomal signaling. Although much progress has been made in addressing the role of EHD4 in mediating retrograde endosomal signaling, many open questions remain. For example, it is unclear whether single or multiple routes for EHD4-mediated endocytosis exist (Winckler & Yap, 2011). Furthermore, whether other EHD proteins are also involved in co-regulating endocytosis for TrkA (Winckler & Yap, 2011) still needs to be addressed.

EHD4 inhibitors may play a decisive role for understanding this function. In particular, it will be interesting to explore whether these inhibitors show an effect on the endosomal signaling in neurons. If such an effect in the cell would be observed, even possible therapeutic applications could be considered. For example, a role for EHD4-specific inhibitors would be to suppress Nogo-A signaling, which may help in functional recovery of the adult CNS in the aftermath of an injury by stimulating regeneration and nerve fiber growth. Such function would be supported by previous studies showing that EHD4 ATPase-deficient mutant completely block the internalization of Nogo-A (Joset et al., 2010).

6.6. Practical application of Drp1 modulators

An interesting aspect of this study was the surprising finding of two activators for Drp1, MS4 and MS5. Both compounds showed a dose-dependent response to increase the stimulated GTPase activity (Figure 39). Activators for dynamin superfamily proteins currently include Ryngo, an activator of dynamin and Silibinin, an activator for Drp1.

Ryngo was shown to target the oligomerization cycle of dynamin and was presented as an attractive potential therapeutic target to treat chronic kidney disease (Schiffer et al., 2015). Silibinin was shown to activate Drp1-dependant mitochondrial fission in cervical cancer cells (You et al., 2020). Both these compounds failed to show an increase in stimulated GTPase activity of Drp1 in two different assay setups (Figure 44A and C).

Inhibitors for EHD2 and EHD4 did not induce any significant change in melting temperature of Drp1 in thermal shift assay. However, the appearance of two distinct melting temperatures in Drp1 melting curve (Figure 49D) in the presence of the activators may point to a conformational change induced by the binding.

Drp1 mutants A395D, R403C and G326D (Fahrner et al., 2016; Vanstone et al., 2016; Waterham et al., 2007) lead to a severe diseased phenotype by destabilizing the Drp1 oligomer and therefore interfering with mitochondrial fission. These mutations are in the stalk region of Drp1, which mediates oligomerization. Drp1 oligomerization is important because it stimulates GTP hydrolysis and the oligomerization-dependent powerstroke leading to membrane constriction. Moreover, the Drp1 receptor MFF at the outer membrane of mitochondria binds stably only to oligomerized Drp1 (Liu & Chan, 2015), leading to its recruitment from the cytosol.

Activators increasing the GTPase activity could act by promoting or stabilizing oligomerization. Pharmacological application of such activators to mutant cell lines may promote or stabilize oligomerization of this hypomorphic variants, which could restore normal functioning of Drp1 at the mitochondria. Further experiments are required to corroborate the potential use of these activators as therapeutic drugs for mitochondria-based diseases.

7. Open question(s) and future perspectives

This study leads to the identification of two inhibitors, MS6 and MS7, whose cellular effects were specific to EHD2. When applied to cells, MS6 and MS7 showed a decrease and increase in lipid droplet area, respectively. Though the cellular lipid droplet assays were reproducible with different cryogenic stocks and passage numbers, it needs to be ascertained at different concentrations and shorter incubation times. The opposite phenotypic effects of MS6 and MS7 should be further studied in morphological and physiological perspectives in relation to EHD2 oligomerization and caveolar mobility.

Transmission electron microscopy (TEM) studies of negatively stained EHDs reconstituted on liposomes showed that in the presence of ATP, EHDs can tubulate liposomes and oligomerize into ring-like structures around them (Daumke et al., 2007; Melo et al., 2017). These tubulation assays in the presence of compounds would help to characterize whether oligomerization of EHD2 is affected. According to the findings in this study, it would be expected that MS6 potentiates oligomer formation whereas MS7 inhibits it. Inhibitors specific for EHD4 could be used as a negative control.

Future *in situ* electron microscopy studies are required to understand the consequences of the inhibitors for cellular membrane morphology. TEM can provide high-resolution ultrastructural information, e.g. cellular organelles can be seen without the need of any labels. Contrasted plastic sections of cells and/or cryo-focused ion beam (cryo-FIB) milled cells (lamellae), studied with TEM, could provide spatial information on caveolae and their attachment points at the plasma membrane, similarly to what has been shown by Matthaeus and colleagues (Matthaeus et al., 2020). This would provide a clearer picture of the effect of the inhibitor on regulating caveolar mobility and thereby explaining the downstream effect on caveolae-mediated fatty acid uptake.

Similar set of experiments could also be done using the identified, potentially specific, EHD4 inhibitors. For example, if an effect on receptor internalization, but not on caveolae morphology, would be observed, this would hint for an EHD4-specific function.

From a structural biology point of view, it would be desirable to understand at atomic resolution the molecular interactions established between the inhibitor and the target

protein. A co-crystal structure would help in understanding inhibitor binding. This would also further shed light on the oligomerization mechanism of EHD2 and explain its *in vivo* phenotypic expression. Co-crystal structures of the specific inhibitors of EHD4 will elucidate the mechanism of inhibitor binding that makes it specific to EHD4. This structural insight related to molecular interaction will be useful when designing and synthesizing new drug molecules to specifically target one EHD family member.

The activators for Drp1 are a good start point regarding modulating Drp1-stimulated GTPase activity but further experiments need to be done. It has to be shown that the activators promote/stabilize oligomerization, which in turn leads to increase in its enzymatic activity. Mutants resulting in disease phenotype needs to be expressed and purified. Similar experiments would need to be done on the mutants to show that the activators are promoting oligomerization and thus restoring the GTPase activity. The rescue of the disease phenotype needs to be shown in a cell-based assay which is currently not available. Alternatively, one can measure Drp1 activity in mitochondrial fission *in vivo* as mentioned in (Hu & Qi, 2020).

The work done in this thesis provides an extensively optimized methodology that can also be efficiently applied to find inhibitors for other members of dynamin superfamily of proteins. Drug screening for EHD proteins has led to the identification of EHD2 inhibitors that have cellular effect in fatty acid uptake which may come from targeting of caveolar mobility. Similarly, EHD4-specific inhibitors have been found and a very interesting finding has been of Drp1 activators. These findings will help us to better understand the respective signaling pathways and in future might have a therapeutic role in the disease.

8. References

Aboulaich, N., Vainonen, J. P., Strålfors, P., & Vener, A. V. (2004). Vectorial proteomics reveal targeting, phosphorylation and specific fragmentation of polymerase I and transcript release factor (PTRF) at the surface of caveolae in human adipocytes. *Biochem J*, *383*(Pt 2), 237-248. https://doi.org/10.1042/bj20040647

Acosta-Quiroga, K., Rojas-Peña, C., Nerio, L. S., Gutiérrez, M., & Polo-Cuadrado, E. (2021). Spirocyclic derivatives as antioxidants: a review [10.1039/D1RA01170G]. *RSC Advances*, *11*(36), 21926-21954. https://doi.org/10.1039/D1RA01170G

Ahmadian, M. R., Stege, P., Scheffzek, K., & Wittinghofer, A. (1997). Confirmation of the arginine-finger hypothesis for the GAP-stimulated GTP-hydrolysis reaction of Ras. *Nature Structural Biology*, *4*(9), 686-689. https://doi.org/10.1038/nsb0997-686

Alasdair Steven, W. B., Louise N. Johnson, Richard N. Perham. (2016). *Molecular Biology of Assemblies and Machines*. Garland Science. https://doi.org/https://doi.org/10.1201/9780429258763

Alexander, C., Votruba, M., Pesch, U. E., Thiselton, D. L., Mayer, S., Moore, A., Rodriguez, M., Kellner, U., Leo-Kottler, B., Auburger, G., Bhattacharya, S. S., & Wissinger, B. (2000). OPA1, encoding a dynamin-related GTPase, is mutated in autosomal dominant optic atrophy linked to chromosome 3q28. *Nat Genet*, *26*(2), 211-215. https://doi.org/10.1038/79944

Allantaz, F., Chaussabel, D., Stichweh, D., Bennett, L., Allman, W., Mejias, A., Ardura, M., Chung, W., Smith, E., Wise, C., Palucka, K., Ramilo, O., Punaro, M., Banchereau, J., & Pascual, V. (2007). Blood leukocyte microarrays to diagnose systemic onset juvenile idiopathic arthritis and follow the response to IL-1 blockade. *J Exp Med*, *204*(9), 2131-2144. https://doi.org/10.1084/jem.20070070

Ammann, L. P., & Goodman, S. R. (2009). Cluster analysis for the impact of sickle cell disease on the human erythrocyte protein interactome. *Exp Biol Med (Maywood)*, *234*(6), 703-711. https://doi.org/10.3181/0806-rm-211

Antonny, B., Burd, C., De Camilli, P., Chen, E., Daumke, O., Faelber, K., Ford, M., Frolov, V. A., Frost, A., Hinshaw, J. E., Kirchhausen, T., Kozlov, M. M., Lenz, M., Low, H. H., McMahon, H., Merrifield, C., Pollard, T. D., Robinson, P. J., Roux, A., & Schmid, S. (2016). Membrane fission by dynamin: what we know and what we need to know. *The EMBO Journal*, *35*(21), 2270-2284. https://doi.org/https://doi.org/10.15252/embj.201694613

Avanti. *18:1 PS and 18:0 PS*. https://avantilipids.com/

Baell, J., & Walters, M. A. (2014). Chemistry: Chemical con artists foil drug discovery. *Nature*, *513*(7519), 481-483. https://doi.org/10.1038/513481a

Baell, J. B., & Holloway, G. A. (2010). New substructure filters for removal of pan assay interference compounds (PAINS) from screening libraries and for their exclusion in bioassays. *J Med Chem*, *53*(7), 2719-2740. https://doi.org/10.1021/jm901137j

Bahl, K., Xie, S., Spagnol, G., Sorgen, P., Naslavsky, N., & Caplan, S. (2016). EHD3 Protein Is Required for Tubular Recycling Endosome Stabilization, and an Asparagine-Glutamic Acid Residue Pair within Its Eps15 Homology (EH) Domain Dictates Its Selective Binding to NPF Peptides. *J Biol Chem*, *291*(26), 13465-13478. https://doi.org/10.1074/jbc.M116.716407

Bajusz, D., Rácz, A., & Héberger, K. (2015). Why is Tanimoto index an appropriate choice for fingerprint-based similarity calculations? *Journal of Cheminformatics*, *7*(1), 20. https://doi.org/10.1186/s13321-015-0069-3

Beg, S., Almalki, W. H., Khatoon, F., Alharbi, K. S., Alghamdi, S., Akhter, M. H., Khalilullah, H., Baothman, A. A., Hafeez, A., Rahman, M., Akhter, S., & Choudhry, H. (2021). Lipid/polymer-based nanocomplexes in nucleic acid delivery as cancer vaccines. *Drug Discovery Today*, *26*(8), 1891-1903. https://doi.org/https://doi.org/10.1016/j.drudis.2021.02.013

Benard, G., & Karbowski, M. (2009). Mitochondrial fusion and division: Regulation and role in cell viability. *Seminars in Cell & Developmental Biology*, *20*(3), 365-374. https://doi.org/https://doi.org/10.1016/j.semcdb.2008.12.012

Berthold, M. R., Cebron, N., Dill, F., Gabriel, T. R., Kötter, T., Meinl, T., Ohl, P., Thiel, K., & Wiswedel, B. (2009). KNIME - the Konstanz information miner: version 2.0 and beyond. *SIGKDD Explor. Newsl.*, *11*(1), 26–31. https://doi.org/10.1145/1656274.1656280

Bisswanger, H. (2014). Enzyme assays. *Perspectives in Science*, *1*(1-6). https://doi.org/https://doi.org/10.1016/j.pisc.2014.02.005

Biswas, T., Pero, J. M., Joseph, C. G., & Tsodikov, O. V. (2009). DNA-Dependent ATPase Activity of Bacterial XPB Helicases. *Biochemistry*, *48*(12), 2839-2848. https://doi.org/10.1021/bi8022416

Bonifacino, J. S., & Glick, B. S. (2004). The mechanisms of vesicle budding and fusion. *Cell*, *116*(2), 153-166. https://doi.org/10.1016/s0092-8674(03)01079-1

Bradley, R. P., Slochower, D. R., Janmey, P. A., & Radhakrishnan, R. Divalent cations bind to phosphoinositides to induce ion and isomer specific propensities for nano-cluster initiation in bilayer membranes. *Royal Society Open Science*, *7*(5), 192208. https://doi.org/10.1098/rsos.192208

Bradley, R. P., Slochower, D. R., Janmey, P. A., & Radhakrishnan, R. (2020). Divalent cations bind to phosphoinositides to induce ion and isomer specific propensities for nano-cluster initiation in bilayer membranes. *Royal Society Open Science*, *7*(5), 192208. https://doi.org/doi:10.1098/rsos.192208

Brooks, S. G., Steven D. Kahl, Chahrzad Montrose, Sitta Sittampalam, Michelle C. Smith, and Jeffrey R. Weidner. (2012). *Basics of Enzymatic Assays for HTS*. Eli Lilly & Company and the National Center for Advancing Translational Sciences; 2004-. https://doi.org/https://www.ncbi.nlm.nih.gov/books/NBK92007/

Cameron, P. L., Ruffin, J. W., Bollag, R., Rasmussen, H., & Cameron, R. S. (1997). Identification of Caveolin and Caveolin-Related Proteins in the Brain. *The Journal of Neuroscience*, *17*(24), 9520-9535. https://doi.org/10.1523/jneurosci.17-24-09520.1997

Cao, H., Garcia, F., & McNiven, M. A. (1998). Differential distribution of dynamin isoforms in mammalian cells. *Mol Biol Cell*, *9*(9), 2595-2609. https://doi.org/10.1091/mbc.9.9.2595

Cao, Y.-L., Meng, S., Chen, Y., Feng, J.-X., Gu, D.-D., Yu, B., Li, Y.-J., Yang, J.-Y., Liao, S., Chan, D. C., & Gao, S. (2017). MFN1 structures reveal nucleotide-triggered dimerization critical for mitochondrial fusion. *Nature*, *542*(7641), 372-376. https://doi.org/10.1038/nature21077

Caplan, S., Naslavsky, N., Hartnell, L. M., Lodge, R., Polishchuk, R. S., Donaldson, J. G., & Bonifacino, J. S. (2002). A tubular EHD1-containing compartment involved in the recycling of major histocompatibility complex class I molecules to the plasma membrane. *EMBO J*, *21*(11), 2557-2567. https://doi.org/10.1093/emboj/21.11.2557

Carver, L. A., & Schnitzer, J. E. (2003). Caveolae: mining little caves for new cancer targets. *Nat Rev Cancer*, *3*(8), 571-581. https://doi.org/10.1038/nrc1146

Cassidy-Stone, A., Chipuk, J. E., Ingerman, E., Song, C., Yoo, C., Kuwana, T., Kurth, M. J., Shaw, J. T., Hinshaw, J. E., Green, D. R., & Nunnari, J. (2008). Chemical inhibition of the mitochondrial division dynamin reveals its role in Bax/Bak-dependent mitochondrial outer membrane permeabilization. *Dev Cell*, *14*(2), 193-204. https://doi.org/10.1016/j.devcel.2007.11.019

Catalán, V., Gómez-Ambrosi, J., Rodríguez, A., Silva, C., Rotellar, F., Gil, M. J., Cienfuegos, J. A., Salvador, J., & Frühbeck, G. (2008). Expression of caveolin-1 in human adipose tissue is upregulated in obesity and obesity-associated type 2 diabetes mellitus and related to inflammation. *Clin Endocrinol (Oxf)*, *68*(2), 213-219. https://doi.org/10.1111/j.1365-2265.2007.03021.x

Chan, D. C. (2012). Fusion and fission: interlinked processes critical for mitochondrial health. *Annu Rev Genet*, *46*, 265-287. https://doi.org/10.1146/annurev-genet-110410-132529

Chappie, J. S., Acharya, S., Leonard, M., Schmid, S. L., & Dyda, F. (2010). G domain dimerization controls dynamin's assembly-stimulated GTPase activity. *Nature*, *465*(7297), 435-440. https://doi.org/10.1038/nature09032

Chen, C., Méndez, E., Houck, J., Fan, W., Lohavanichbutr, P., Doody, D., Yueh, B., Futran, N. D., Upton, M., Farwell, D. G., Schwartz, S. M., & Zhao, L. P. (2008). Gene expression profiling identifies genes predictive of oral squamous cell carcinoma. *Cancer Epidemiol Biomarkers Prev*, *17*(8), 2152-2162. https://doi.org/10.1158/1055-9965.Epi-07-2893

Chen, M. S., Obar, R. A., Schroeder, C. C., Austin, T. W., Poodry, C. A., Wadsworth, S. C., & Vallee, R. B. (1991). Multiple forms of dynamin are encoded by shibire, a Drosophila gene involved in endocytosis. *Nature*, *351*(6327), 583-586. https://doi.org/10.1038/351583a0

Cheng, J. P. X., & Nichols, B. J. (2016). Caveolae: One Function or Many? *Trends in Cell Biology*, *26*(3), 177-189. https://doi.org/https://doi.org/10.1016/j.tcb.2015.10.010

Chow, B. W., Nuñez, V., Kaplan, L., Granger, A. J., Bistrong, K., Zucker, H. L., Kumar, P., Sabatini, B. L., & Gu, C. (2020). Caveolae in CNS arterioles mediate neurovascular coupling. *Nature*, *579*(7797), 106-110. https://doi.org/10.1038/s41586-020-2026-1

Clark, S. G., Shurland, D. L., Meyerowitz, E. M., Bargmann, C. I., & van der Bliek, A. M. (1997). A dynamin GTPase mutation causes a rapid and reversible temperature-inducible locomotion defect in C. elegans. *Proc Natl Acad Sci U S A*, *94*(19), 10438-10443. https://doi.org/10.1073/pnas.94.19.10438

Conner, S. D., & Schmid, S. L. (2003). Regulated portals of entry into the cell. *Nature*, *422*(6927), 37-44. https://doi.org/10.1038/nature01451

Copeland, R. A. (2005). Evaluation of enzyme inhibitors in drug discovery. A guide for medicinal chemists and pharmacologists. *Methods Biochem Anal*, *46*, 1-265.

Cortez, K. J., Lyman, C. A., Kottilil, S., Kim, H. S., Roilides, E., Yang, J., Fullmer, B., Lempicki, R., & Walsh, T. J. (2006). Functional genomics of innate host defense molecules in normal human monocytes in response to Aspergillus fumigatus. *Infect Immun*, *74*(4), 2353-2365. https://doi.org/10.1128/iai.74.4.2353-2365.2006

da Costa Cesar, I., Nogueira, F. H., & Pianetti, G. A. (2008). Comparison of HPLC, UV spectrophotometry and potentiometric titration methods for the determination of lumefantrine in pharmaceutical products. *J Pharm Biomed Anal*, *48*(1), 223-226. https://doi.org/10.1016/j.jpba.2008.05.006

Dahlin, J. L., & Walters, M. A. (2016). How to Triage PAINS-Full Research. *Assay Drug Dev Technol*, *14*(3), 168-174. https://doi.org/10.1089/adt.2015.674

Daumke, O., Lundmark, R., Vallis, Y., Martens, S., Butler, P. J., & McMahon, H. T. (2007). Architectural and mechanistic insights into an EHD ATPase involved in membrane remodelling. *Nature*, *449*(7164), 923-927. https://doi.org/10.1038/nature06173

Daumke, O., & Praefcke, G. J. K. (2016). Invited review: Mechanisms of GTP hydrolysis and conformational transitions in the dynamin superfamily. *Biopolymers*, *105*(8), 580-593. https://doi.org/https://doi.org/10.1002/bip.22855

Daumke, O., Roux, A., & Haucke, V. (2014). BAR domain scaffolds in dynamin-mediated membrane fission. *Cell*, *156*(5), 882-892. https://doi.org/10.1016/j.cell.2014.02.017

de Souza, W., Sant'Anna, C., & Cunha-e-Silva, N. L. (2009). Electron microscopy and cytochemistry analysis of the endocytic pathway of pathogenic protozoa. *Progress in Histochemistry and Cytochemistry*, *44*(2), 67-124. https://doi.org/https://doi.org/10.1016/j.proghi.2009.01.001

Dervan, E. W., Chen, H., Ho, S. L., Brummel, N., Schmid, J., Toomey, D., Haralambova, M., Gould, E., Wallace, D. M., Prehn, J. H., O'Brien, C. J., & Murphy, D. (2010). Protein macroarray profiling of serum autoantibodies in pseudoexfoliation glaucoma. *Invest Ophthalmol Vis Sci*, *51*(6), 2968-2975. https://doi.org/10.1167/iovs.09-4898

Desmond, J. C., Raynaud, S., Tung, E., Hofmann, W. K., Haferlach, T., & Koeffler, H. P. (2007). Discovery of epigenetically silenced genes in acute myeloid leukemias. *Leukemia*, *21*(5), 1026-1034. https://doi.org/10.1038/sj.leu.2404611

Doherty, G. J., & McMahon, H. T. (2009). Mechanisms of Endocytosis. *Annual Review of Biochemistry*, *78*(1), 857-902. https://doi.org/10.1146/annurev.biochem.78.081307.110540

Doherty, K. R., Demonbreun, A. R., Wallace, G. Q., Cave, A., Posey, A. D., Heretis, K., Pytel, P., & McNally, E. M. (2008). The endocytic recycling protein EHD2 interacts with myoferlin to regulate myoblast fusion. *J Biol Chem*, *283*(29), 20252-20260. https://doi.org/10.1074/jbc.M802306200

Domingues, L., Hurbain, I., Gilles-Marsens, F., Sirés-Campos, J., André, N., Dewulf, M., Romao, M., Viaris de Lesegno, C., Macé, A.-S., Blouin, C., Guéré, C., Vié, K., Raposo, G., Lamaze, C., & Delevoye, C. (2020). Coupling of melanocyte signaling and mechanics by caveolae is required for human skin pigmentation. *Nature Communications*, *11*(1), 2988. https://doi.org/10.1038/s41467-020-16738-z

Drab, M., Verkade, P., Elger, M., Kasper, M., Lohn, M., Lauterbach, B., Menne, J., Lindschau, C., Mende, F., Luft, F. C., Schedl, A., Haller, H., & Kurzchalia, T. V. (2001). Loss of caveolae, vascular dysfunction, and pulmonary defects in caveolin-1 gene-disrupted mice. *Science*, *293*(5539), 2449-2452. https://doi.org/10.1126/science.1062688

Duan, D., Torosyan, H., Elnatan, D., McLaughlin, C. K., Logie, J., Shoichet, M. S., Agard, D. A., & Shoichet, B. K. (2017). Internal Structure and Preferential Protein Binding of Colloidal Aggregates. *ACS Chemical Biology*, *12*(1), 282-290. https://doi.org/10.1021/acschembio.6b00791

Dudutienė, V., Zubrienė, A., Kairys, V., Smirnov, A., Smirnovienė, J., Leitans, J., Kazaks, A., Tars, K., Manakova, L., Gražulis, S., & Matulis, D. (2020). Isoform-Selective Enzyme Inhibitors by Exploring Pocket Size According to the Lock-and-Key Principle. *Biophysical Journal*, *119*(8), 1513-1524. https://doi.org/https://doi.org/10.1016/j.bpj.2020.08.037

Edeling, M. A., Smith, C., & Owen, D. (2006). Life of a clathrin coat: insights from clathrin and AP structures. *Nat Rev Mol Cell Biol*, *7*(1), 32-44. https://doi.org/10.1038/nrm1786

Emsley, P., Lohkamp, B., Scott, W. G., & Cowtan, K. (2010). Features and development of Coot. *Acta Crystallogr D Biol Crystallogr*, *66*(Pt 4), 486-501. https://doi.org/10.1107/S0907444910007493

Eyre, N. S., Cleland, L. G., Tandon, N. N., & Mayrhofer, G. (2007). Importance of the carboxyl terminus of FAT/CD36 for plasma membrane localization and function in long-chain fatty acid uptake. *J Lipid Res*, *48*(3), 528-542. https://doi.org/10.1194/jlr.M600255-JLR200

Faelber, K., Gao, S., Held, M., Posor, Y., Haucke, V., Noé, F., & Daumke, O. (2013). Chapter Fifteen - Oligomerization of Dynamin Superfamily Proteins in Health and Disease. In J. Giraldo & F. Ciruela (Eds.), *Progress in Molecular Biology and Translational Science* (Vol. 117, pp. 411-443). Academic Press. https://doi.org/https://doi.org/10.1016/B978-0-12-386931-9.00015-5

Fahrner, J. A., Liu, R., Perry, M. S., Klein, J., & Chan, D. C. (2016). A novel de novo dominant negative mutation in DNM1L impairs mitochondrial fission and presents as childhood epileptic encephalopathy. *Am J Med Genet A*, *170*(8), 2002-2011. https://doi.org/10.1002/ajmg.a.37721

Feng, J., Chen, Y., Pu, J., Yang, X., Zhang, C., Zhu, S., Zhao, Y., Yuan, Y., Yuan, H., & Liao, F. (2011). An improved malachite green assay of phosphate: mechanism and application. *Anal Biochem*, *409*(1), 144-149. https://doi.org/10.1016/j.ab.2010.10.025

Ferguson, S. M., & De Camilli, P. (2012). Dynamin, a membrane-remodelling GTPase. *Nature Reviews Molecular Cell Biology*, *13*(2), 75-88. https://doi.org/10.1038/nrm3266

Ferguson, S. M., Raimondi, A., Paradise, S., Shen, H., Mesaki, K., Ferguson, A., Destaing, O., Ko, G., Takasaki, J., Cremona, O., E, O. T., & De Camilli, P. (2009). Coordinated actions of actin and BAR proteins upstream of dynamin at endocytic clathrin-coated pits. *Dev Cell*, *17*(6), 811-822. https://doi.org/10.1016/j.devcel.2009.11.005

Fields, M. V. L. D. (1996). *Antibiotic and cytotoxic drug susceptibility assays using resazurin and poising agents* (US Patent No. U. patent.

Förstermann, U., & Sessa, W. C. (2012). Nitric oxide synthases: regulation and function. *Eur Heart J*, *33*(7), 829-837, 837a-837d. https://doi.org/10.1093/eurheartj/ehr304

Fra, A. M., Williamson, E., Simons, K., & Parton, R. G. (1995). De novo formation of caveolae in lymphocytes by expression of VIP21-caveolin. *Proc Natl Acad Sci U S A*, *92*(19), 8655-8659. https://doi.org/10.1073/pnas.92.19.8655

Frank, P. G., Pavlides, S., & Lisanti, M. P. (2009). Caveolae and transcytosis in endothelial cells: role in atherosclerosis. *Cell Tissue Res*, *335*(1), 41-47. https://doi.org/10.1007/s00441-008-0659-8

Frank, S., Gaume, B., Bergmann-Leitner, E. S., Leitner, W. W., Robert, E. G., Catez, F., Smith, C. L., & Youle, R. J. (2001). The role of dynamin-related protein 1, a mediator of mitochondrial fission, in apoptosis. *Dev Cell*, *1*(4), 515-525. https://doi.org/10.1016/s1534-5807(01)00055-7

Frohlich, C., Grabiger, S., Schwefel, D., Faelber, K., Rosenbaum, E., Mears, J., Rocks, O., & Daumke, O. (2013). Structural insights into oligomerization and mitochondrial remodelling of dynamin 1-like protein. *EMBO J*, *32*(9), 1280-1292. https://doi.org/10.1038/emboj.2013.74

Gackowski, M., Koba, M., Madra-Gackowska, K., & Kruszewski, S. (2019). Comparison of high-performance thin layer chromatography/UV-densitometry and UV-derivative spectrophotometry for the determination of trimetazidine in pharmaceutical formulations. *Acta Pharm*, *69*(3), 413-422. https://doi.org/10.2478/acph-2019-0028

Galindo, C. L., Sha, J., Ribardo, D. A., Fadl, A. A., Pillai, L., & Chopra, A. K. (2003). Identification of Aeromonas hydrophila cytotoxic enterotoxin-induced genes in macrophages using microarrays. *J Biol Chem*, *278*(41), 40198-40212. https://doi.org/10.1074/jbc.M305788200

Gammie, A. E., Kurihara, L. J., Vallee, R. B., & Rose, M. D. (1995). DNM1, a dynamin-related gene, participates in endosomal trafficking in yeast. *J Cell Biol*, *130*(3), 553-566. https://doi.org/10.1083/jcb.130.3.553

Gasteiger, E., Gattiker, A., Hoogland, C., Ivanyi, I., Appel, R. D., & Bairoch, A. (2003). ExPASy: The proteomics server for in-depth protein knowledge and analysis. *Nucleic Acids Res*, *31*(13), 3784-3788. https://doi.org/10.1093/nar/gkg563

Gaulton, A., Bellis, L. J., Bento, A. P., Chambers, J., Davies, M., Hersey, A., Light, Y., McGlinchey, S., Michalovich, D., Al-Lazikani, B., & Overington, J. P. (2012). ChEMBL: a large-scale bioactivity database for drug discovery. *Nucleic Acids Res*, *40*(Database issue), D1100-1107. https://doi.org/10.1093/nar/gkr777

George, M., Ying, G., Rainey, M. A., Solomon, A., Parikh, P. T., Gao, Q., Band, V., & Band, H. (2007). Shared as well as distinct roles of EHD proteins revealed by biochemical and functional comparisons in mammalian cells and C. elegans. *BMC Cell Biol*, *8*, 3. https://doi.org/10.1186/1471-2121-8-3

Gilmartin, A. G., Faitg, T. H., Richter, M., Groy, A., Seefeld, M. A., Darcy, M. G., Peng, X., Federowicz, K., Yang, J., Zhang, S.-Y., Minthorn, E., Jaworski, J.-P., Schaber, M., Martens, S., McNulty, D. E., Sinnamon, R. H., Zhang, H., Kirkpatrick, R. B., Nevins, N., . . . Kumar, R. (2014). Allosteric Wip1 phosphatase inhibition through flap-subdomain interaction. *Nature Chemical Biology*, *10*(3), 181-187. https://doi.org/10.1038/nchembio.1427

Goodchild, S. C., Sheynis, T., Thompson, R., Tipping, K. W., Xue, W.-F., Ranson, N. A., Beales, P. A., Hewitt, E. W., & Radford, S. E. (2014). β2-Microglobulin Amyloid Fibril-Induced Membrane Disruption Is Enhanced by Endosomal Lipids and Acidic pH. *PLoS One*, *9*(8), e104492. https://doi.org/10.1371/journal.pone.0104492

Gordon, C. P., Venn-Brown, B., Robertson, M. J., Young, K. A., Chau, N., Mariana, A., Whiting, A., Chircop, M., Robinson, P. J., & McCluskey, A. (2013). Development of second-generation indole-based dynamin GTPase inhibitors. *J Med Chem*, *56*(1), 46-59. https://doi.org/10.1021/jm300844m

Grant, B. D., & Donaldson, J. G. (2009). Pathways and mechanisms of endocytic recycling. *Nature Reviews Molecular Cell Biology*, *10*(9), 597-608. https://doi.org/10.1038/nrm2755

Grimm, T. M., Dierdorf, N. I., Betz, K., Paone, C., & Hauck, C. R. (2020). PPM1F controls integrin activity via a conserved phospho-switch. *Journal of Cell Biology*, *219*(12), e202001057. https://doi.org/10.1083/jcb.202001057

Grimm, T. M., Herbinger, M., Krüger, L., Müller, S., Mayer, T. U., & Hauck, C. R. (2022). Lockdown, a selective small-molecule inhibitor of the integrin phosphatase PPM1F, blocks cancer cell invasion. *Cell Chemical Biology*, *29*(6), 930-946.e939. https://doi.org/https://doi.org/10.1016/j.chembiol.2022.03.011

Guilherme, A., Soriano, N. A., Furcinitti, P. S., & Czech, M. P. (2004). Role of EHD1 and EHBP1 in perinuclear sorting and insulin-regulated GLUT4 recycling in 3T3-L1 adipocytes. *J Biol Chem*, *279*(38), 40062-40075. https://doi.org/10.1074/jbc.M401918200

Guilherme., Soriano, N. A., Bose, S., Holik, J., Bose, A., Pomerleau, D. P., Furcinitti, P., Leszyk, J., Corvera, S., & Czech, M. P. (2004). EHD2 and the novel EH domain binding protein EHBP1 couple endocytosis to the actin cytoskeleton. *J Biol Chem*, *279*(11), 10593-10605. https://doi.org/10.1074/jbc.M307702200

Guo, L., & Bramkamp, M. (2019). Bacterial dynamin-like protein DynA mediates lipid and content mixing. *Faseb j*, *33*(11), 11746-11757. https://doi.org/10.1096/fj.201900844RR

Hales, K. G., & Fuller, M. T. (1997). Developmentally regulated mitochondrial fusion mediated by a conserved, novel, predicted GTPase. *Cell*, *90*(1), 121-129. https://doi.org/10.1016/s0092-8674(00)80319-0

Hall, A. (2004). *GTPases*. Oxford University Press. https://www.amazon.de/-/en/Alan-Hall/dp/019963744X

Haller, O., & Kochs, G. (2011). Human MxA protein: an interferon-induced dynamin-like GTPase with broad antiviral activity. *J Interferon Cytokine Res*, *31*(1), 79-87. https://doi.org/10.1089/jir.2010.0076

Han, B., Copeland, C. A., Kawano, Y., Rosenzweig, E. B., Austin, E. D., Shahmirzadi, L., Tang, S., Raghunathan, K., Chung, W. K., & Kenworthy, A. K. (2016). Characterization of a caveolin-1 mutation associated with both pulmonary arterial hypertension and congenital generalized lipodystrophy. *Traffic*, *17*(12), 1297-1312. https://doi.org/https://doi.org/10.1111/tra.12452

Han, B., Copeland, C. A., Tiwari, A., & Kenworthy, A. K. (2016). Assembly and Turnover of Caveolae: What Do We Really Know? *Front Cell Dev Biol*, *4*, 68. https://doi.org/10.3389/fcell.2016.00068

Hansel, D. E., Rahman, A., House, M., Ashfaq, R., Berg, K., Yeo, C. J., & Maitra, A. (2004). Met proto-oncogene and insulin-like growth factor binding protein 3 overexpression correlates with metastatic ability in well-differentiated pancreatic endocrine neoplasms. *Clin Cancer Res*, *10*(18 Pt 1), 6152-6158. https://doi.org/10.1158/1078-0432.Ccr-04-0285

Hansen, C. G., Howard, G., & Nichols, B. J. (2011). Pacsin 2 is recruited to caveolae and functions in caveolar biogenesis. *J Cell Sci*, *124*(Pt 16), 2777-2785. https://doi.org/10.1242/jcs.084319

Henley, J. R., Krueger, E. W., Oswald, B. J., & McNiven, M. A. (1998). Dynamin-mediated internalization of caveolae. *J Cell Biol*, *141*(1), 85-99. https://doi.org/10.1083/jcb.141.1.85

Hill, M. M., Bastiani, M., Luetterforst, R., Kirkham, M., Kirkham, A., Nixon, S. J., Walser, P., Abankwa, D., Oorschot, V. M., Martin, S., Hancock, J. F., & Parton, R. G. (2008). PTRF-Cavin, a conserved cytoplasmic protein required for caveola formation and function. *Cell*, *132*(1), 113-124. https://doi.org/10.1016/j.cell.2007.11.042

Hill, T., Odell, L. R., Edwards, J. K., Graham, M. E., McGeachie, A. B., Rusak, J., Quan, A., Abagyan, R., Scott, J. L., Robinson, P. J., & McCluskey, A. (2005). Small molecule inhibitors of dynamin I GTPase activity: development of dimeric tyrphostins. *J Med Chem*, *48*(24), 7781-7788. https://doi.org/10.1021/jm0402081

Hill, T. A., Gordon, C. P., McGeachie, A. B., Venn-Brown, B., Odell, L. R., Chau, N., Quan, A., Mariana, A., Sakoff, J. A., Chircop, M., Robinson, P. J., & McCluskey, A. (2009). Inhibition of dynamin mediated endocytosis by the dynoles--synthesis and functional activity of a family of indoles. *J Med Chem*, *52*(12), 3762-3773. https://doi.org/10.1021/jm900036m

Hill, T. A., Odell, L. R., Quan, A., Abagyan, R., Ferguson, G., Robinson, P. J., & McCluskey, A. (2004). Long chain amines and long chain ammonium salts as novel inhibitors of dynamin GTPase activity. *Bioorganic & Medicinal Chemistry Letters*, *14*(12), 3275-3278. https://doi.org/https://doi.org/10.1016/j.bmcl.2004.03.096

Hinderlich, S., Neuenschwander, M., Wratil, P. R., Oder, A., Lisurek, M., Nguyen, L. D., von Kries, J. P., & Hackenberger, C. P. R. (2017). Small Molecules Targeting Human N-Acetylmannosamine Kinase. *Chembiochem*, *18*(13), 1279-1285. https://doi.org/10.1002/cbic.201700066

Horvath, A., Mathyakina, L., Vong, Q., Baxendale, V., Pang, A. L., Chan, W. Y., & Stratakis, C. A. (2006). Serial analysis of gene expression in adrenocortical hyperplasia caused by a germline PRKAR1A mutation. *J Clin Endocrinol Metab*, *91*(2), 584-596. https://doi.org/10.1210/jc.2005-1301

Howes, M. T., Kirkham, M., Riches, J., Cortese, K., Walser, P. J., Simpson, F., Hill, M. M., Jones, A., Lundmark, R., Lindsay, M. R., Hernandez-Deviez, D. J., Hadzic, G., McCluskey, A., Bashir, R., Liu, L., Pilch, P., McMahon, H., Robinson, P. J., Hancock, J. F., . . . Parton, R. G. (2010). Clathrin-independent carriers form a high capacity endocytic sorting system at the leading edge of migrating cells. *J Cell Biol*, *190*(4), 675-691. https://doi.org/10.1083/jcb.201002119

Hu, D., & Qi, X. (2020). Measuring Drp1 Activity in Mitochondrial Fission In Vivo. *Methods Mol Biol*, *2159*, 189-195. https://doi.org/10.1007/978-1-0716-0676-6_14

Hubert, M., Larsson, E., Vegesna, N. V. G., Ahnlund, M., Johansson, A. I., Moodie, L. W., & Lundmark, R. (2020). Lipid accumulation controls the balance between surface connection and scission of caveolae. *Elife*, *9*. https://doi.org/10.7554/eLife.55038

Ingerman , E., Perkins , E. M., Marino , M., Mears , J. A., McCaffery , J. M., Hinshaw , J. E., & Nunnari , J. (2005). Dnm1 forms spirals that are structurally tailored to fit mitochondria. *Journal of Cell Biology*, *170*(7), 1021-1027. https://doi.org/10.1083/jcb.200506078

Irwin, J. J., Duan, D., Torosyan, H., Doak, A. K., Ziebart, K. T., Sterling, T., Tumanian, G., & Shoichet, B. K. (2015). An Aggregation Advisor for Ligand Discovery. *J Med Chem*, *58*(17), 7076-7087. https://doi.org/10.1021/acs.jmedchem.5b01105

Ishihara, N., Nomura, M., Jofuku, A., Kato, H., Suzuki, S. O., Masuda, K., Otera, H., Nakanishi, Y., Nonaka, I., Goto, Y., Taguchi, N., Morinaga, H., Maeda, M., Takayanagi, R., Yokota, S., & Mihara, K. (2009). Mitochondrial fission factor Drp1 is essential for embryonic development and synapse formation in mice. *Nat Cell Biol*, *11*(8), 958-966. https://doi.org/10.1038/ncb1907

Itaya, K., & Ui, M. (1966). A new micromethod for the colorimetric determination of inorganic phosphate. *Clin Chim Acta*, *14*(3), 361-366. https://doi.org/10.1016/0009-8981(66)90114-8

Jansen, F. H., Krijgsveld, J., van Rijswijk, A., van den Bemd, G. J., van den Berg, M. S., van Weerden, W. M., Willemsen, R., Dekker, L. J., Luider, T. M., & Jenster, G. (2009). Exosomal secretion of cytoplasmic prostate cancer xenograft-derived proteins. *Mol Cell Proteomics*, *8*(6), 1192-1205. https://doi.org/10.1074/mcp.M800443-MCP200

Jin, R., Cao, R., & Baumgart, T. (2022). Curvature dependence of BAR protein membrane association and dissociation kinetics. *Sci Rep*, *12*(1), 7676. https://doi.org/10.1038/s41598-022-11221-9

Joseph Jose Thottacherry, M. S., Chaitra Prabhakara, and Satyajit Mayor. (2019). Spoiled for Choice: DiverseEndocytic Pathways Functionat the Cell Surface. *Annual Review of Cell and Developmental Biology*, *35:55-84*. https://doi.org/https://doi.org/10.1146/annurev-cellbio-100617-062710

Joset, A., Dodd, D. A., Halegoua, S., & Schwab, M. E. (2010). Pincher-generated Nogo-A endosomes mediate growth cone collapse and retrograde signaling. *J Cell Biol*, *188*(2), 271-285. https://doi.org/10.1083/jcb.200906089

Jović, M., Naslavsky, N., Rapaport, D., Horowitz, M., & Caplan, S. (2007). EHD1 regulates beta1 integrin endosomal transport: effects on focal adhesions, cell spreading and migration. *J Cell Sci*, *120*(Pt 5), 802-814. https://doi.org/10.1242/jcs.03383

Juang, R. (2004). *BC basics*. http://juang.bst.ntu.edu.tw/BCbasics/Animation.htm

Kageyama, Y., Zhang, Z., Roda, R., Fukaya, M., Wakabayashi, J., Wakabayashi, N., Kensler, T. W., Reddy, P. H., Iijima, M., & Sesaki, H. (2012). Mitochondrial division ensures the survival of postmitotic neurons by suppressing oxidative damage. *Journal of Cell Biology*, *197*(4), 535-551. https://doi.org/10.1083/jcb.201110034

Ketteler, J., & Klein, D. (2018). Caveolin-1, cancer and therapy resistance. *Int J Cancer*, *143*(9), 2092-2104. https://doi.org/10.1002/ijc.31369

Kirkham, M., & Parton, R. G. (2005). Clathrin-independent endocytosis: New insights into caveolae and non-caveolar lipid raft carriers. *Biochimica et Biophysica Acta (BBA) - Molecular Cell Research*, *1745*(3), 273-286. https://doi.org/https://doi.org/10.1016/j.bbamcr.2005.06.002

Koch, A., Thiemann, M., Grabenbauer, M., Yoon, Y., McNiven, M. A., & Schrader, M. (2003). Dynamin-like protein 1 is involved in peroxisomal fission. *J Biol Chem*, *278*(10), 8597-8605. https://doi.org/10.1074/jbc.M211761200

Kovtun, O., Tillu, V. A., Ariotti, N., Parton, R. G., & Collins, B. M. (2015). Cavin family proteins and the assembly of caveolae. *J Cell Sci*, *128*(7), 1269-1278. https://doi.org/10.1242/jcs.167866

Lab, L. p. M. *Liposome and Lipid tubule production*. https://www2.mrc-lmb.cam.ac.uk/groups/hmm/techniqs/Liposome.html

Labrousse, A. M., Zappaterra, M. D., Rube, D. A., & van der Bliek, A. M. (1999). C. elegans Dynamin-Related Protein DRP-1 Controls Severing of the Mitochondrial Outer Membrane. *Molecular Cell*, *4*(5), 815-826. https://doi.org/https://doi.org/10.1016/S1097-2765(00)80391-3

Lamaze, C., Tardif, N., Dewulf, M., Vassilopoulos, S., & Blouin, C. M. (2017). The caveolae dress code: structure and signaling. *Curr Opin Cell Biol*, *47*, 117-125. https://doi.org/10.1016/j.ceb.2017.02.014

Larsson, E., Morén, B., McMahon, K.-A., Parton, R. G., & Lundmark, R. (2022). Dynamin2 stabilizes plasma membrane-connected caveolae by restraining fission. *bioRxiv*, 2022.2005.2025.493372. https://doi.org/10.1101/2022.05.25.493372

Laudadio, E., Minnelli, C., Amici, A., Massaccesi, L., Mobbili, G., & Galeazzi, R. (2018). Liposomal Formulations for an Efficient Encapsulation of Epigallocatechin-3-gallate: An in- Silico/Experimental Approach. *Molecules*, *23*(2). https://doi.org/10.3390/molecules23020441

Lee, D. W., Zhao, X., Scarselletta, S., Schweinsberg, P. J., Eisenberg, E., Grant, B. D., & Greene, L. E. (2005). ATP binding regulates oligomerization and endosome association of RME-1 family proteins. *J Biol Chem*, *280*(17), 17213-17220. https://doi.org/10.1074/jbc.M412751200

Li, Z., Schulze, R. J., Weller, S. G., Krueger, E. W., Schott, M. B., Zhang, X., Casey, C. A., Liu, J., Stöckli, J., James, D. E., & McNiven, M. A. (2016). A novel Rab10-EHBP1-EHD2 complex essential for the autophagic engulfment of lipid droplets. *Sci Adv*, *2*(12), e1601470. https://doi.org/10.1126/sciadv.1601470

Lian, X., Matthaeus, C., Kaßmann, M., Daumke, O., & Gollasch, M. (2019). Pathophysiological Role of Caveolae in Hypertension. *Front Med (Lausanne)*, *6*, 153. https://doi.org/10.3389/fmed.2019.00153

Lin, S. X., Grant, B., Hirsh, D., & Maxfield, F. R. (2001). Rme-1 regulates the distribution and function of the endocytic recycling compartment in mammalian cells. *Nat Cell Biol*, *3*(6), 567-572. https://doi.org/10.1038/35078543

Lipa-Castro, A., Legrand, F.-X., & Barratt, G. (2021). Cochleate drug delivery systems: An approach to their characterization. *International Journal of Pharmaceutics*, *610*, 121225. https://doi.org/https://doi.org/10.1016/j.ijpharm.2021.121225

Lipardi, C., Mora, R., Colomer, V., Paladino, S., Nitsch, L., Rodriguez-Boulan, E., & Zurzolo, C. (1998). Caveolin Transfection Results in Caveolae Formation but Not Apical Sorting of Glycosylphosphatidylinositol (GPI)-anchored Proteins in Epithelial Cells. *Journal of Cell Biology*, *140*(3), 617-626. https://doi.org/10.1083/jcb.140.3.617

Lisurek, M., Rupp, B., Wichard, J., Neuenschwander, M., von Kries, J. P., Frank, R., Rademann, J., & Kühne, R. (2010). Design of chemical libraries with potentially bioactive molecules applying a maximum common substructure concept. *Molecular Diversity*, *14*(2), 401-408. https://doi.org/10.1007/s11030-009-9187-z

Liu, R., & Chan, D. C. (2015). The mitochondrial fission receptor Mff selectively recruits oligomerized Drp1. *Mol Biol Cell*, *26*(24), 4466-4477. https://doi.org/10.1091/mbc.E15-08-0591

Liu, R., & Chan, D. C. (2017). OPA1 and cardiolipin team up for mitochondrial fusion. *Nat Cell Biol*, *19*(7), 760-762. https://doi.org/10.1038/ncb3565

Liu, Y. W., Surka, M. C., Schroeter, T., Lukiyanchuk, V., & Schmid, S. L. (2008). Isoform and splice-variant specific functions of dynamin-2 revealed by analysis of conditional knock-out cells. *Mol Biol Cell*, *19*(12), 5347-5359. https://doi.org/10.1091/mbc.e08-08-0890

Liu., Brown, D., McKee, M., Lebrasseur, N. K., Yang, D., Albrecht, K. H., Ravid, K., & Pilch, P. F. (2008). Deletion of Cavin/PTRF causes global loss of caveolae, dyslipidemia, and glucose intolerance. *Cell Metab*, *8*(4), 310-317. https://doi.org/10.1016/j.cmet.2008.07.008

Losón, O. C., Song, Z., Chen, H., & Chan, D. C. (2013). Fis1, Mff, MiD49, and MiD51 mediate Drp1 recruitment in mitochondrial fission. *Mol Biol Cell*, *24*(5), 659-667. https://doi.org/10.1091/mbc.E12-10-0721

Low, H. H., & Löwe, J. (2006). A bacterial dynamin-like protein. *Nature*, *444*(7120), 766-769. https://doi.org/10.1038/nature05312

Ludwig, A., Howard, G., Mendoza-Topaz, C., Deerinck, T., Mackey, M., Sandin, S., Ellisman, M. H., & Nichols, B. J. (2013). Molecular Composition and Ultrastructure of the Caveolar Coat Complex. *PLOS Biology*, *11*(8), e1001640. https://doi.org/10.1371/journal.pbio.1001640

Ludwig., Howard, G., Mendoza-Topaz, C., Deerinck, T., Mackey, M., Sandin, S., Ellisman, M. H., & Nichols, B. J. (2013). Molecular composition and ultrastructure of the caveolar coat complex. *PLoS Biol*, *11*(8), e1001640. https://doi.org/10.1371/journal.pbio.1001640

Ma, H., Deacon, S., & Horiuchi, K. (2008). The challenge of selecting protein kinase assays for lead discovery optimization. *Expert Opin Drug Discov*, *3*(6), 607-621. https://doi.org/10.1517/17460441.3.6.607

Macia, E., Ehrlich, M., Massol, R., Boucrot, E., Brunner, C., & Kirchhausen, T. (2006). Dynasore, a cell-permeable inhibitor of dynamin. *Dev Cell*, *10*(6), 839-850. https://doi.org/10.1016/j.devcel.2006.04.002

Maher, E. A., Furnari, F. B., Bachoo, R. M., Rowitch, D. H., Louis, D. N., Cavenee, W. K., & DePinho, R. A. (2001). Malignant glioma: genetics and biology of a grave matter. *Genes Dev*, *15*(11), 1311-1333. https://doi.org/10.1101/gad.891601

Marg, A., Schoewel, V., Timmel, T., Schulze, A., Shah, C., Daumke, O., & Spuler, S. (2012). Sarcolemmal repair is a slow process and includes EHD2. *Traffic*, *13*(9), 1286-1294. https://doi.org/10.1111/j.1600-0854.2012.01386.x

Martinez-Outschoorn, U. E., Sotgia, F., & Lisanti, M. P. (2015). Caveolae and signalling in cancer. *Nat Rev Cancer*, *15*(4), 225-237. https://doi.org/10.1038/nrc3915

Matthaeus, C., Lahmann, I., Kunz, S., Jonas, W., Melo, A. A., Lehmann, M., Larsson, E., Lundmark, R., Kern, M., Bluher, M., Olschowski, H., Kompa, J., Brugger, B., Muller, D. N., Haucke, V., Schurmann, A., Birchmeier, C., & Daumke, O. (2020). EHD2-mediated restriction of caveolar dynamics regulates cellular fatty acid uptake. *Proc Natl Acad Sci U S A*, *117*(13), 7471-7481. https://doi.org/10.1073/pnas.1918415117

Matthaeus, C., Lian, X., Kunz, S., Lehmann, M., Zhong, C., Bernert, C., Lahmann, I., Müller, D. N., Gollasch, M., & Daumke, O. (2019). eNOS-NO-induced small blood vessel relaxation requires EHD2-dependent caveolae stabilization. *PLoS One*, *14*(10), e0223620. https://doi.org/10.1371/journal.pone.0223620

Matthaeus, C., Sochacki, K. A., Dickey, A., Puchkov, D., Haucke, V., Lehmann, M., & Taraska, J. W. (2022). The molecular organization of flat and curved caveolae indicates bendable structural units at the plasma membrane. *bioRxiv*, 2022.2003.2031.486578. https://doi.org/10.1101/2022.03.31.486578

Matthaeus, C., & Taraska, J. W. (2021). Energy and Dynamics of Caveolae Trafficking. *Front Cell Dev Biol*, *8*, 614472. https://doi.org/10.3389/fcell.2020.614472

Mayor, S., & Pagano, R. E. (2007). Pathways of clathrin-independent endocytosis. *Nat Rev Mol Cell Biol*, *8*(8), 603-612. https://doi.org/10.1038/nrm2216

Mayor, S., Parton, R. G., & Donaldson, J. G. (2014). Clathrin-independent pathways of endocytosis. *Cold Spring Harb Perspect Biol*, *6*(6). https://doi.org/10.1101/cshperspect.a016758

McBride, H. M., & Frost, A. (2016). Cell biology: Double agents for mitochondrial division. *Nature*, *540*(7631), 43-44. https://doi.org/10.1038/nature20482

McGovern, S. L., Caselli, E., Grigorieff, N., & Shoichet, B. K. (2002). A common mechanism underlying promiscuous inhibitors from virtual and high-throughput screening. *J Med Chem*, *45*(8), 1712-1722. https://doi.org/10.1021/jm010533y

McGovern, S. L., Helfand, B. T., Feng, B., & Shoichet, B. K. (2003). A specific mechanism of nonspecific inhibition. *J Med Chem*, *46*(20), 4265-4272. https://doi.org/10.1021/jm030266r

McKenna, R., & Frost, S. C. (2014). Overview of the Carbonic Anhydrase Family. In S. C. Frost & R. McKenna (Eds.), *Carbonic Anhydrase: Mechanism, Regulation, Links to Disease, and Industrial Applications* (pp. 3-5). Springer Netherlands. https://doi.org/10.1007/978-94-007-7359-2_1

McMillian, M. K., Li, L., Parker, J. B., Patel, L., Zhong, Z., Gunnett, J. W., Powers, W. J., & Johnson, M. D. (2002). An improved resazurin-based cytotoxicity assay for hepatic cells. *Cell Biol Toxicol*, *18*(3), 157-173. https://doi.org/10.1023/a:1015559603643

Mears, J. A., Ray, P., & Hinshaw, J. E. (2007). A Corkscrew Model for Dynamin Constriction. *Structure*, *15*(10), 1190-1202. https://doi.org/https://doi.org/10.1016/j.str.2007.08.012

Melo, A. A., Hegde, B. G., Shah, C., Larsson, E., Isas, J. M., Kunz, S., Lundmark, R., Langen, R., & Daumke, O. (2017). Structural insights into the activation mechanism of dynamin-like EHD ATPases. *Proc Natl Acad Sci U S A*, *114*(22), 5629-5634. https://doi.org/10.1073/pnas.1614075114

Melo, A. A., Sprink, T., Noel, J. K., Vázquez Sarandeses, E., van Hoorn, C., Loerke, J., Spahn, C. M. T., & Daumke, O. (2021). Cryo-electron tomography reveals structural insights into the membrane binding and remodeling activity of dynamin-like EHDs. *bioRxiv*, 2021.2009.2020.461157. https://doi.org/10.1101/2021.09.20.461157

Merck. *18:1 PS (DOPS)*.

Mershon, M. M., Rhoads, L. S., & Van Buskirk, R. G. (1994). Alamar Blue Discloses Latent Toxicity of Vesicant in Human Epidermal Model and Cells. *Journal of Toxicology: Cutaneous and Ocular Toxicology*, *13*(4), 289-310. https://doi.org/10.3109/15569529409037530

Mohan, J., Morén, B., Larsson, E., Holst, M. R., & Lundmark, R. (2015). Cavin3 interacts with cavin1 and caveolin1 to increase surface dynamics of caveolae. *J Cell Sci*, *128*(5), 979-991. https://doi.org/10.1242/jcs.161463

Mohanakrishnan, A., Tran, T. V. M., Kumar, M., Chen, H., Posner, B. A., & Schmid, S. L. (2017). A highly-sensitive high throughput assay for dynamin's basal GTPase activity. *PLoS One*, *12*(9), e0185639. https://doi.org/10.1371/journal.pone.0185639

Moren, B., Shah, C., Howes, M. T., Schieber, N. L., McMahon, H. T., Parton, R. G., Daumke, O., & Lundmark, R. (2012). EHD2 regulates caveolar dynamics via ATP-driven targeting and oligomerization. *Mol Biol Cell*, *23*(7), 1316-1329. https://doi.org/10.1091/mbc.E11-09-0787

Nagy, G. N., Suardíaz, R., Lopata, A., Ozohanics, O., Vékey, K., Brooks, B. R., Leveles, I., Tóth, J., Vértessy, B. G., & Rosta, E. (2016). Structural Characterization of Arginine Fingers: Identification of an Arginine Finger for the Pyrophosphatase dUTPases. *Journal of the American Chemical Society*, *138*(45), 15035-15045. https://doi.org/10.1021/jacs.6b09012

Naslavsky, N., & Caplan, S. (2005). C-terminal EH-domain-containing proteins: consensus for a role in endocytic trafficking, EH? *J Cell Sci*, *118*(Pt 18), 4093-4101. https://doi.org/10.1242/jcs.02595

Naslavsky, N., & Caplan, S. (2011). EHD proteins: key conductors of endocytic transport. *Trends Cell Biol*, *21*(2), 122-131. https://doi.org/10.1016/j.tcb.2010.10.003

Naslavsky, N., & Caplan, S. (2018). The enigmatic endosome – sorting the ins and outs of endocytic trafficking. *Journal of Cell Science*, *131*(13). https://doi.org/10.1242/jcs.216499

Naslavsky, N., Rahajeng, J., Rapaport, D., Horowitz, M., & Caplan, S. (2007). EHD1 regulates cholesterol homeostasis and lipid droplet storage. *Biochem Biophys Res Commun*, *357*(3), 792-799. https://doi.org/10.1016/j.bbrc.2007.04.022

Naslavsky, N., Rahajeng, J., Sharma, M., Jović, M., & Caplan, S. (2006). Interactions between EHD Proteins and Rab11-FIP2: A Role for EHD3 in Early Endosomal Transport. *Molecular Biology of the Cell*, *17*(1), 163-177. https://doi.org/10.1091/mbc.e05-05-0466

Nicholas, K. B., Nicholas H.B. Jr., and Deerfield, D.W. II. (1997). GeneDoc: Analysis and Visualization of Genetic Variation. *EMBNEW.NEWS 4:14*. https://doi.org/http://nrbsc.org/gfx/genedoc/index.html

Nunnari, J., & Suomalainen, A. (2012). Mitochondria: In Sickness and in Health. *Cell*, *148*(6), 1145-1159. https://doi.org/https://doi.org/10.1016/j.cell.2012.02.035

Obar, R. A., Collins, C. A., Hammarback, J. A., Shpetner, H. S., & Vallee, R. B. (1990). Molecular cloning of the microtubule-associated mechanochemical enzyme dynamin reveals homology with a new family of GTP-binding proteins. *Nature*, *347*(6290), 256-261. https://doi.org/10.1038/347256a0

Oh, P., Horner, T., Witkiewicz, H., & Schnitzer, J. E. (2012). Endothelin induces rapid, dynamin-mediated budding of endothelial caveolae rich in ET-B. *J Biol Chem*, *287*(21), 17353-17362. https://doi.org/10.1074/jbc.M111.338897

Oh, P., McIntosh, D. P., & Schnitzer, J. E. (1998). Dynamin at the neck of caveolae mediates their budding to form transport vesicles by GTP-driven fission from the plasma membrane of endothelium. *J Cell Biol*, *141*(1), 101-114. https://doi.org/10.1083/jcb.141.1.101

Okamoto, K., & Shaw, J. M. (2005). Mitochondrial morphology and dynamics in yeast and multicellular eukaryotes. *Annu Rev Genet*, *39*, 503-536. https://doi.org/10.1146/annurev.genet.38.072902.093019

Otera, H., & Mihara, K. (2011). Discovery of the membrane receptor for mitochondrial fission GTPase Drp1. *Small GTPases*, *2*(3), 167-172. https://doi.org/10.4161/sgtp.2.3.16486

Otera, H., Wang, C., Cleland, M. M., Setoguchi, K., Yokota, S., Youle, R. J., & Mihara, K. (2010). Mff is an essential factor for mitochondrial recruitment of Drp1 during mitochondrial fission in mammalian cells. *J Cell Biol*, *191*(6), 1141-1158. https://doi.org/10.1083/jcb.201007152

Page, B., Page, M., & Noel, C. (1993). A new fluorometric assay for cytotoxicity measurements in-vitro. *Int J Oncol*, *3*(3), 473-476. https://www.ncbi.nlm.nih.gov/pubmed/21573387

Pahl, J. H. W., Kwappenberg, K. M. C., Varypataki, E. M., Santos, S. J., Kuijjer, M. L., Mohamed, S., Wijnen, J. T., van Tol, M. J. D., Cleton-Jansen, A.-M., Egeler, R. M., Jiskoot, W., Lankester, A. C., & Schilham, M. W. (2014). Macrophages inhibit human osteosarcoma cell growth after activation with the bacterial cell wall derivative liposomal muramyl tripeptide in combination with interferon-γ. *Journal of Experimental & Clinical Cancer Research*, *33*(1), 27. https://doi.org/10.1186/1756-9966-33-27

Palade, G. E. (1953). The fine structure of blood capillaries. *J Appl Phys*, *24*, 1424. https://cir.nii.ac.jp/crid/1573387450263222528

Pappalardi, M. B., Keenan, K., Cockerill, M., Kellner, W. A., Stowell, A., Sherk, C., Wong, K., Pathuri, S., Briand, J., Steidel, M., Chapman, P., Groy, A., Wiseman, A. K., McHugh, C. F., Campobasso, N., Graves, A. P., Fairweather, E., Werner, T., Raoof, A., . . . McCabe, M. T. (2021). Discovery of a first-in-class reversible DNMT1-selective inhibitor with improved tolerability and efficacy in acute myeloid leukemia. *Nat Cancer*, *2*(10), 1002-1017.

Park, D. S., Woodman, S. E., Schubert, W., Cohen, A. W., Frank, P. G., Chandra, M., Shirani, J., Razani, B., Tang, B., Jelicks, L. A., Factor, S. M., Weiss, L. M., Tanowitz, H. B., & Lisanti, M. P. (2002). Caveolin-1/3 double-knockout mice are viable, but lack both muscle and non-muscle caveolae, and develop a severe cardiomyopathic phenotype. *Am J Pathol*, *160*(6), 2207-2217. https://doi.org/10.1016/s0002-9440(10)61168-6

Park, M., Penick, E. C., Edwards, J. G., Kauer, J. A., & Ehlers, M. D. (2004). Recycling endosomes supply AMPA receptors for LTP. *Science*, *305*(5692), 1972-1975. https://doi.org/10.1126/science.1102026

Parton, R. G., & del Pozo, M. A. (2013). Caveolae as plasma membrane sensors, protectors and organizers. *Nature Reviews Molecular Cell Biology*, *14*(2), 98-112. https://doi.org/10.1038/nrm3512

Pavlovic, J., Schröder, A., Blank, A., Pitossi, F., & Staeheli, P. (1993). Mx proteins: GTPases involved in the interferon-induced antiviral state. *Ciba Found Symp*, *176*, 233-243; discussion 243-237. https://doi.org/10.1002/9780470514450.ch15

Pelkmans, L., Kartenbeck, J., & Helenius, A. (2001). Caveolar endocytosis of simian virus 40 reveals a new two-step vesicular-transport pathway to the ER. *Nature Cell Biology*, *3*(5), 473-483. https://doi.org/10.1038/35074539

Picciano, J. A., Ameen, N., Grant, B. D., & Bradbury, N. A. (2003). Rme-1 regulates the recycling of the cystic fibrosis transmembrane conductance regulator. *Am J Physiol Cell Physiol*, *285*(5), C1009-1018. https://doi.org/10.1152/ajpcell.00140.2003

Pilch, P. F., & Liu, L. (2011). Fat caves: caveolae, lipid trafficking and lipid metabolism in adipocytes. *Trends in Endocrinology & Metabolism*, *22*(8), 318-324. https://doi.org/https://doi.org/10.1016/j.tem.2011.04.001

Porta, J. C., Han, B., Gulsevin, A., Chung, J. M., Peskova, Y., Connolly, S., Mchaourab, H. S., Meiler, J., Karakas, E., Kenworthy, A. K., & Ohi, M. D. (2022). Molecular architecture of the human caveolin-1 complex. *Science Advances*, *8*(19), eabn7232. https://doi.org/doi:10.1126/sciadv.abn7232

Pradhan, S., Bacolla, A., Wells, R. D., & Roberts, R. J. (1999). Recombinant human DNA (cytosine-5) methyltransferase. I. Expression, purification, and comparison of de novo and maintenance methylation. *J Biol Chem*, *274*(46), 33002-33010. https://doi.org/10.1074/jbc.274.46.33002

Praefcke, G. J. K., & McMahon, H. T. (2004). The dynamin superfamily: universal membrane tubulation and fission molecules? *Nature Reviews Molecular Cell Biology*, *5*(2), 133-147. https://doi.org/10.1038/nrm1313

Prakash, B., Praefcke, G. J., Renault, L., Wittinghofer, A., & Herrmann, C. (2000). Structure of human guanylate-binding protein 1 representing a unique class of GTP-binding proteins. *Nature*, *403*(6769), 567-571. https://doi.org/10.1038/35000617

Quambusch, L., Depta, L., Landel, I., Lubeck, M., Kirschner, T., Nabert, J., Uhlenbrock, N., Weisner, J., Kostka, M., Levy, L. M., Schultz-Fademrecht, C., Glanemann, F., Althoff, K., Müller, M. P., Siveke, J. T., &

Rauh, D. (2021). Cellular model system to dissect the isoform-selectivity of Akt inhibitors. *Nature Communications*, *12*(1), 5297. https://doi.org/10.1038/s41467-021-25512-8

Quambusch, L., Landel, I., Depta, L., Weisner, J., Uhlenbrock, N., Müller, M. P., Glanemann, F., Althoff, K., Siveke, J. T., & Rauh, D. (2019). Covalent-Allosteric Inhibitors to Achieve Akt Isoform-Selectivity. *Angew Chem Int Ed Engl*, *58*(52), 18823-18829. https://doi.org/10.1002/anie.201909857

Raimondi, A., Ferguson, S. M., Lou, X., Armbruster, M., Paradise, S., Giovedi, S., Messa, M., Kono, N., Takasaki, J., Cappello, V., O'Toole, E., Ryan, T. A., & De Camilli, P. (2011). Overlapping role of dynamin isoforms in synaptic vesicle endocytosis. *Neuron*, *70*(6), 1100-1114. https://doi.org/10.1016/j.neuron.2011.04.031

Razani, B., Engelman, J. A., Wang, X. B., Schubert, W., Zhang, X. L., Marks, C. B., Macaluso, F., Russell, R. G., Li, M., Pestell, R. G., Di Vizio, D., Hou, H., Jr., Kneitz, B., Lagaud, G., Christ, G. J., Edelmann, W., & Lisanti, M. P. (2001). Caveolin-1 null mice are viable but show evidence of hyperproliferative and vascular abnormalities. *J Biol Chem*, *276*(41), 38121-38138. https://doi.org/10.1074/jbc.M105408200

Razani, B., Wang, X. B., Engelman, J. A., Battista, M., Lagaud, G., Zhang, X. L., Kneitz, B., Hou, H., Jr., Christ, G. J., Edelmann, W., & Lisanti, M. P. (2002). Caveolin-2-deficient mice show evidence of severe pulmonary dysfunction without disruption of caveolae. *Mol Cell Biol*, *22*(7), 2329-2344. https://doi.org/10.1128/mcb.22.7.2329-2344.2002

Ren, H., Dou, S.-X., Rigolet, P., Yang, Y., Wang, P.-Y., Amor-Gueret, M., & Xi, X. G. (2007). The arginine finger of the Bloom syndrome protein: its structural organization and its role in energy coupling. *Nucleic Acids Research*, *35*(18), 6029-6041. https://doi.org/10.1093/nar/gkm544

Reubold, T. F., Eschenburg, S., Becker, A., Leonard, M., Schmid, S. L., Vallee, R. B., Kull, F. J., & Manstein, D. J. (2005). Crystal structure of the GTPase domain of rat dynamin 1. *Proc Natl Acad Sci U S A*, *102*(37), 13093-13098. https://doi.org/10.1073/pnas.0506491102

Ring, A., Le Lay, S., Pohl, J., Verkade, P., & Stremmel, W. (2006). Caveolin-1 is required for fatty acid translocase (FAT/CD36) localization and function at the plasma membrane of mouse embryonic fibroblasts. *Biochim Biophys Acta*, *1761*(4), 416-423. https://doi.org/10.1016/j.bbalip.2006.03.016

Ringstad, N., Gad, H., Löw, P., Di Paolo, G., Brodin, L., Shupliakov, O., & De Camilli, P. (1999). Endophilin/SH3p4 is required for the transition from early to late stages in clathrin-mediated synaptic vesicle endocytosis. *Neuron*, *24*(1), 143-154. https://doi.org/10.1016/s0896-6273(00)80828-4

Roback, L. (2015). American Society of Human Genetics,

Rogawski, D. S., Deng, J., Li, H., Miao, H., Borkin, D., Purohit, T., Song, J., Chase, J., Li, S., Ndoj, J., Klossowski, S., Kim, E., Mao, F., Zhou, B., Ropa, J., Krotoska, M. Z., Jin, Z., Ernst, P., Feng, X., . . . Grembecka, J. (2021). Discovery of first-in-class inhibitors of ASH1L histone methyltransferase with anti-leukemic activity. *Nature Communications*, *12*(1), 2792. https://doi.org/10.1038/s41467-021-23152-6

Rogers, D., & Hahn, M. (2010). Extended-Connectivity Fingerprints. *Journal of Chemical Information and Modeling*, *50*(5), 742-754. https://doi.org/10.1021/ci100050t

Root, K. T., Plucinsky, S. M., & Glover, K. J. (2015). Chapter Nine - Recent Progress in the Topology, Structure, and Oligomerization of Caveolin: A Building Block of Caveolae. In A. K. Kenworthy (Ed.), *Current Topics in Membranes* (Vol. 75, pp. 305-336). Academic Press. https://doi.org/https://doi.org/10.1016/bs.ctm.2015.03.007

Ross, J. L., Ali, M. Y., & Warshaw, D. M. (2008). Cargo transport: molecular motors navigate a complex cytoskeleton. *Current Opinion in Cell Biology*, *20*(1), 41-47. https://doi.org/https://doi.org/10.1016/j.ceb.2007.11.006

Rudack, T., Xia, F., Schlitter, J., Kötting, C., & Gerwert, K. (2012). The role of magnesium for geometry and charge in GTP hydrolysis, revealed by quantum mechanics/molecular mechanics simulations. *Biophys J*, *103*(2), 293-302. https://doi.org/10.1016/j.bpj.2012.06.015

Sandvig, K., Pust, S., Skotland, T., & van Deurs, B. (2011). Clathrin-independent endocytosis: mechanisms and function. *Curr Opin Cell Biol*, *23*(4), 413-420. https://doi.org/10.1016/j.ceb.2011.03.007

Santolini, E., Salcini, A. E., Kay, B. K., Yamabhai, M., & Di Fiore, P. P. (1999). The EH network. *Exp Cell Res*, *253*(1), 186-209. https://doi.org/10.1006/excr.1999.4694

Schiffer, M., Teng, B., Gu, C., Shchedrina, V. A., Kasaikina, M., Pham, V. A., Hanke, N., Rong, S., Gueler, F., Schroder, P., Tossidou, I., Park, J. K., Staggs, L., Haller, H., Erschow, S., Hilfiker-Kleiner, D., Wei, C., Chen, C., Tardi, N., . . . Sever, S. (2015). Pharmacological targeting of actin-dependent dynamin oligomerization ameliorates chronic kidney disease in diverse animal models. *Nat Med*, *21*(6), 601-609. https://doi.org/10.1038/nm.3843

Schindelin, J., Arganda-Carreras, I., Frise, E., Kaynig, V., Longair, M., Pietzsch, T., Preibisch, S., Rueden, C., Saalfeld, S., Schmid, B., Tinevez, J. Y., White, D. J., Hartenstein, V., Eliceiri, K., Tomancak, P., & Cardona, A. (2012). Fiji: an open-source platform for biological-image analysis. *Nat Methods*, *9*(7), 676-682. https://doi.org/10.1038/nmeth.2019

Schneider, C. A., Rasband, W. S., & Eliceiri, K. W. (2012). NIH Image to ImageJ: 25 years of image analysis. *Nat Methods*, *9*(7), 671-675. https://doi.org/10.1038/nmeth.2089

Schrauwen, I., Szelinger, S., Siniard, A. L., Kurdoglu, A., Corneveaux, J. J., Malenica, I., Richholt, R., Van Camp, G., De Both, M., Swaminathan, S., Turk, M., Ramsey, K., Craig, D. W., Narayanan, V., & Huentelman, M. J. (2015). A Frame-Shift Mutation in CAV1 Is Associated with a Severe Neonatal Progeroid and Lipodystrophy Syndrome. *PLoS One*, *10*(7), e0131797. https://doi.org/10.1371/journal.pone.0131797

Seemann, E., Sun, M., Krueger, S., Tröger, J., Hou, W., Haag, N., Schüler, S., Westermann, M., Huebner, C. A., Romeike, B., Kessels, M. M., & Qualmann, B. (2017). Deciphering caveolar functions by syndapin III KO-mediated impairment of caveolar invagination. *Elife*, *6*. https://doi.org/10.7554/eLife.29854

Senju, Y., Itoh, Y., Takano, K., Hamada, S., & Suetsugu, S. (2011). Essential role of PACSIN2/syndapin-II in caveolae membrane sculpting. *Journal of Cell Science*, *124*(12), 2032-2040. https://doi.org/10.1242/jcs.086264

Shah, C., Hegde, B. G., Moren, B., Behrmann, E., Mielke, T., Moenke, G., Spahn, C. M. T., Lundmark, R., Daumke, O., & Langen, R. (2014). Structural insights into membrane interaction and caveolar targeting of dynamin-like EHD2. *Structure*, *22*(3), 409-420. https://doi.org/10.1016/j.str.2013.12.015

Shajahan, A. N., Timblin, B. K., Sandoval, R., Tiruppathi, C., Malik, A. B., & Minshall, R. D. (2004). Role of Src-induced dynamin-2 phosphorylation in caveolae-mediated endocytosis in endothelial cells. *J Biol Chem*, *279*(19), 20392-20400. https://doi.org/10.1074/jbc.M308710200

Shao, Y., Akmentin, W., Toledo-Aral, J. J., Rosenbaum, J., Valdez, G., Cabot, J. B., Hilbush, B. S., & Halegoua, S. (2002). Pincher, a pinocytic chaperone for nerve growth factor/TrkA signaling endosomes. *J Cell Biol*, *157*(4), 679-691. https://doi.org/10.1083/jcb.200201063

Sharma, M., Naslavsky, N., & Caplan, S. (2008). A role for EHD4 in the regulation of early endosomal transport. *Traffic*, *9*(6), 995-1018. https://doi.org/10.1111/j.1600-0854.2008.00732.x

Shin, J., Monti, S., Aires, D. J., Duvic, M., Golub, T., Jones, D. A., & Kupper, T. S. (2007). Lesional gene expression profiling in cutaneous T-cell lymphoma reveals natural clusters associated with disease outcome. *Blood*, *110*(8), 3015-3027. https://doi.org/10.1182/blood-2006-12-061507

Shiota, T., Traven, A., & Lithgow, T. (2015). Mitochondrial biogenesis: cell-cycle-dependent investment in making mitochondria. *Curr Biol*, *25*(2), R78-r80. https://doi.org/10.1016/j.cub.2014.12.006

Shpetner, H. S., & Vallee, R. B. (1989). Identification of dynamin, a novel mechanochemical enzyme that mediates interactions between microtubules. *Cell*, *59*(3), 421-432. https://doi.org/10.1016/0092-8674(89)90027-5

Shvets, E., Bitsikas, V., Howard, G., Hansen, C. G., & Nichols, B. J. (2015). Dynamic caveolae exclude bulk membrane proteins and are required for sorting of excess glycosphingolipids. *Nat Commun*, *6*, 6867. https://doi.org/10.1038/ncomms7867

Sievers, F., Wilm, A., Dineen, D., Gibson, T. J., Karplus, K., Li, W., Lopez, R., McWilliam, H., Remmert, M., Söding, J., Thompson, J. D., & Higgins, D. G. (2011). Fast, scalable generation of high-quality protein multiple sequence alignments using Clustal Omega. *Molecular Systems Biology*, *7*(1), 539. https://doi.org/https://doi.org/10.1038/msb.2011.75

Sigma-Aldrich. *LOPAC® Library of Pharmacologically Active Compounds*. https://www.sigmaaldrich.com/DE/en/product/sigma/sc001

Sigma. *Brain PS*. https://www.sigmaaldrich.com/catalog/product/avanti/840032c?lang=de&region=DE&cm_sp=Insite-_-prodRecCold_xviews-_-prodRecCold3-2

Smirnova, E., Griparic, L., Shurland, D. L., & van der Bliek, A. M. (2001). Dynamin-related protein Drp1 is required for mitochondrial division in mammalian cells. *Mol Biol Cell*, *12*(8), 2245-2256. https://doi.org/10.1091/mbc.12.8.2245

Smith, C. A., Dho, S. E., Donaldson, J., Tepass, U., & McGlade, C. J. (2004). The cell fate determinant numb interacts with EHD/Rme-1 family proteins and has a role in endocytic recycling. *Mol Biol Cell*, *15*(8), 3698-3708. https://doi.org/10.1091/mbc.e04-01-0026

Soulet, F., Yarar, D., Leonard, M., & Schmid, S. L. (2005). SNX9 regulates dynamin assembly and is required for efficient clathrin-mediated endocytosis. *Mol Biol Cell*, *16*(4), 2058-2067. https://doi.org/10.1091/mbc.e04-11-1016

Stoeber, M., Stoeck, I. K., Hänni, C., Bleck, C. K., Balistreri, G., & Helenius, A. (2012). Oligomers of the ATPase EHD2 confine caveolae to the plasma membrane through association with actin. *EMBO J*, *31*(10), 2350-2364. https://doi.org/10.1038/emboj.2012.98

Tagad, H. D., Debnath, S., Clausse, V., Saha, M., Mazur, S. J., Appella, E., & Appella, D. H. (2018). Chemical Features Important for Activity in a Class of Inhibitors Targeting the Wip1 Flap Subdomain [https://doi.org/10.1002/cmdc.201700779]. *ChemMedChem*, *13*(9), 894-901. https://doi.org/https://doi.org/10.1002/cmdc.201700779

Takei, K., McPherson, P. S., Schmid, S. L., & De Camilli, P. (1995). Tubular membrane invaginations coated by dynamin rings are induced by GTP-gamma S in nerve terminals. *Nature*, *374*(6518), 186-190. https://doi.org/10.1038/374186a0

Taniwaki, M., Daigo, Y., Ishikawa, N., Takano, A., Tsunoda, T., Yasui, W., Inai, K., Kohno, N., & Nakamura, Y. (2006). Gene expression profiles of small-cell lung cancers: molecular signatures of lung cancer. *Int J Oncol*, *29*(3), 567-575.

Tripal, P., Bauer, M., Naschberger, E., Mörtinger, T., Hohenadl, C., Cornali, E., Thurau, M., & Stürzl, M. (2007). Unique Features of Different Members of the Human Guanylate-Binding Protein Family. *Journal of Interferon & Cytokine Research*, *27*(1), 44-52. https://doi.org/10.1089/jir.2007.0086

Tripathi, A. K., Sha, W., Shulaev, V., Stins, M. F., & Sullivan, D. J., Jr. (2009). Plasmodium falciparum-infected erythrocytes induce NF-kappaB regulated inflammatory pathways in human cerebral endothelium. *Blood*, *114*(19), 4243-4252. https://doi.org/10.1182/blood-2009-06-226415

Uhlén, M., Fagerberg, L., Hallström, B. M., Lindskog, C., Oksvold, P., Mardinoglu, A., Sivertsson, Å., Kampf, C., Sjöstedt, E., Asplund, A., Olsson, I., Edlund, K., Lundberg, E., Navani, S., Szigyarto, C. A.-K., Odeberg, J., Djureinovic, D., Takanen, J. O., Hober, S., . . . Pontén, F. (2015). Tissue-based map of the human proteome. *Science*, *347*(6220), 1260419. https://doi.org/10.1126/science.1260419

Valdez, G., Akmentin, W., Philippidou, P., Kuruvilla, R., Ginty, D. D., & Halegoua, S. (2005). Pincher-mediated macroendocytosis underlies retrograde signaling by neurotrophin receptors. *J Neurosci*, *25*(21), 5236-5247. https://doi.org/10.1523/jneurosci.5104-04.2005

van der Bliek, A. M., & Meyerowitz, E. M. (1991). Dynamin-like protein encoded by the Drosophila shibire gene associated with vesicular traffic. *Nature*, *351*(6325), 411-414. https://doi.org/10.1038/351411a0

Vanstone, J. R., Smith, A. M., McBride, S., Naas, T., Holcik, M., Antoun, G., Harper, M. E., Michaud, J., Sell, E., Chakraborty, P., Tetreault, M., Care4Rare, C., Majewski, J., Baird, S., Boycott, K. M., Dyment, D. A., MacKenzie, A., & Lines, M. A. (2016). DNM1L-related mitochondrial fission defect presenting as refractory epilepsy. *Eur J Hum Genet*, *24*(7), 1084-1088. https://doi.org/10.1038/ejhg.2015.243

Varanini, Z. P., G. Pjnton, R. Maggioni, A. . (1988). Characterization of a potassium-stimulated ATPase in membrane fraction isolated from roots of grapevine seedlings. *Vitis*, *27*, 209-222.

Wakabayashi, J., Zhang, Z., Wakabayashi, N., Tamura, Y., Fukaya, M., Kensler, T. W., Iijima, M., & Sesaki, H. (2009). The dynamin-related GTPase Drp1 is required for embryonic and brain development in mice. *J Cell Biol*, *186*(6), 805-816. https://doi.org/10.1083/jcb.200903065

Wang, S., Tukachinsky, H., Romano, F. B., & Rapoport, T. A. (2016). Cooperation of the ER-shaping proteins atlastin, lunapark, and reticulons to generate a tubular membrane network. *Elife*, *5*, e18605. https://doi.org/10.7554/eLife.18605

Warnock., Hinshaw, J. E., & Schmid, S. L. (1996). Dynamin Self-assembly Stimulates Its GTPase Activity*. *Journal of Biological Chemistry*, *271*(37), 22310-22314. https://doi.org/https://doi.org/10.1074/jbc.271.37.22310

Waterham, H. R., Koster, J., van Roermund, C. W., Mooyer, P. A., Wanders, R. J., & Leonard, J. V. (2007). A lethal defect of mitochondrial and peroxisomal fission. *N Engl J Med*, *356*(17), 1736-1741. https://doi.org/10.1056/NEJMoa064436

Wells, C. I., Al-Ali, H., Andrews, D. M., Asquith, C. R. M., Axtman, A. D., Dikic, I., Ebner, D., Ettmayer, P., Fischer, C., Frederiksen, M., Futrell, R. E., Gray, N. S., Hatch, S. B., Knapp, S., Lucking, U., Michaelides, M., Mills, C. E., Muller, S., Owen, D., . . . Drewry, D. H. (2021). The Kinase Chemogenomic Set (KCGS): An Open Science Resource for Kinase Vulnerability Identification. *Int J Mol Sci*, *22*(2). https://doi.org/10.3390/ijms22020566

Winckler, B., & Yap, C. C. (2011). Endocytosis and endosomes at the crossroads of regulating trafficking of axon outgrowth-modifying receptors. *Traffic*, *12*(9), 1099-1108. https://doi.org/10.1111/j.1600-0854.2011.01213.x

Xing, Y., Wen, Z., Gao, W., Lin, Z., Zhong, J., & Jiu, Y. (2020). Multifaceted Functions of Host Cell Caveolae/Caveolin-1 in Virus Infections. *Viruses*, *12*(5). https://doi.org/10.3390/v12050487

Yamada, E. (1955). The fine structure of the gall bladder epithelium of the mouse. *J Biophys Biochem Cytol*, *1*(5), 445-458. https://doi.org/10.1083/jcb.1.5.445

Yang, J. J., Ursu, O., Lipinski, C. A., Sklar, L. A., Oprea, T. I., & Bologa, C. G. (2016). Badapple: promiscuity patterns from noisy evidence. *J Cheminform*, *8*, 29. https://doi.org/10.1186/s13321-016-0137-3

Yang, M., & Wang, G. (2016). ATPase activity measurement of DNA replicative helicase from Bacillus stearothermophilus by malachite green method. *Anal Biochem*, *509*, 46-49. https://doi.org/10.1016/j.ab.2016.06.028

Yao, Q., Chen, J., Cao, H., Orth, J. D., McCaffery, J. M., Stan, R. V., & McNiven, M. A. (2005). Caveolin-1 interacts directly with dynamin-2. *J Mol Biol*, *348*(2), 491-501. https://doi.org/10.1016/j.jmb.2005.02.003

Yap, C. C. C., Lasiecka, Z. M., Caplan, S., & Winckler, B. (2010). Alterations of EHD1/EHD4 Protein Levels Interfere with L1/NgCAM Endocytosis in Neurons and Disrupt Axonal Targeting. *The Journal of Neuroscience*, *30*(19), 6646. https://doi.org/10.1523/JNEUROSCI.5428-09.2010

Yap., Lasiecka, Z. M., Caplan, S., & Winckler, B. (2010). Alterations of EHD1/EHD4 protein levels interfere with L1/NgCAM endocytosis in neurons and disrupt axonal targeting. *J Neurosci*, *30*(19), 6646-6657. https://doi.org/10.1523/jneurosci.5428-09.2010

Yohannes, E., Chang, J., Christ, G. J., Davies, K. P., & Chance, M. R. (2008). Proteomics analysis identifies molecular targets related to diabetes mellitus-associated bladder dysfunction. *Mol Cell Proteomics*, *7*(7), 1270-1285. https://doi.org/10.1074/mcp.M700563-MCP200

Yoon, G., Malam, Z., Paton, T., Marshall, C. R., Hyatt, E., Ivakine, Z., Scherer, S. W., Lee, K. S., Hawkins, C., & Cohn, R. D. (2016). Lethal Disorder of Mitochondrial Fission Caused by Mutations in DNM1L. *J Pediatr*, *171*, 313-316.e311-312. https://doi.org/10.1016/j.jpeds.2015.12.060

You, Y., He, Q., Lu, H., Zhou, X., Chen, L., Liu, H., Lu, Z., Liu, D., Liu, Y., Zuo, D., Fu, X., Kwan, H., & Zhao, X. (2020). Silibinin Induces G2/M Cell Cycle Arrest by Activating Drp1-Dependent Mitochondrial Fission in Cervical Cancer. *Front Pharmacol*, *11*, 271. https://doi.org/10.3389/fphar.2020.00271

Yukawa, A., Iino, R., Watanabe, R., Hayashi, S., & Noji, H. (2015). Key Chemical Factors of Arginine Finger Catalysis of F1-ATPase Clarified by an Unnatural Amino Acid Mutation. *Biochemistry*, *54*(2), 472-480. https://doi.org/10.1021/bi501138b

Zarif, L. (2002). Elongated supramolecular assemblies in drug delivery. *Journal of Controlled Release*, *81*(1), 7-23. https://doi.org/https://doi.org/10.1016/S0168-3659(02)00010-X

Zegzouti, H., Zdanovskaia, M., Hsiao, K., & Goueli, S. A. (2009). ADP-Glo: A Bioluminescent and homogeneous ADP monitoring assay for kinases. *Assay Drug Dev Technol*, *7*(6), 560-572. https://doi.org/10.1089/adt.2009.0222

Zhang, J. H., Chung, T. D., & Oldenburg, K. R. (1999). A Simple Statistical Parameter for Use in Evaluation and Validation of High Throughput Screening Assays. *J Biomol Screen*, *4*(2), 67-73. https://doi.org/10.1177/108705719900400206

Zhang, W., Ou, X., & Wu, X. (2019). Proteomics profiling of plasma exosomes in epithelial ovarian cancer: A potential role in the coagulation cascade, diagnosis and prognosis. *Int J Oncol*, *54*(5), 1719-1733. https://doi.org/10.3892/ijo.2019.4742

Zheng, Y., Tice, C. M., & Singh, S. B. (2014). The use of spirocyclic scaffolds in drug discovery. *Bioorganic & Medicinal Chemistry Letters*, *24*(16), 3673-3682. https://doi.org/https://doi.org/10.1016/j.bmcl.2014.06.081

Zhou, Y., Ariotti, N., Rae, J., Liang, H., Tillu, V., Tee, S., Bastiani, M., Bademosi, A. T., Collins, B. M., Meunier, F. A., Hancock, J. F., & Parton, R. G. (2020). Dissecting the nanoscale lipid profile of caveolae. *bioRxiv*, 2020.2001.2016.909408. https://doi.org/10.1101/2020.01.16.909408

9.1. Appendix A: IC_{50} curves

n_H stands for Hill coefficient

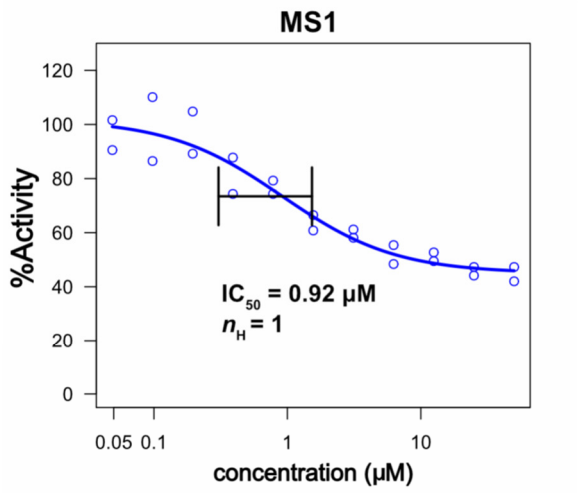

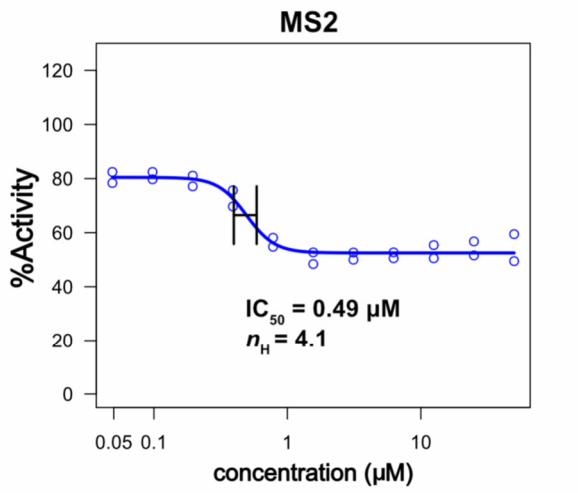

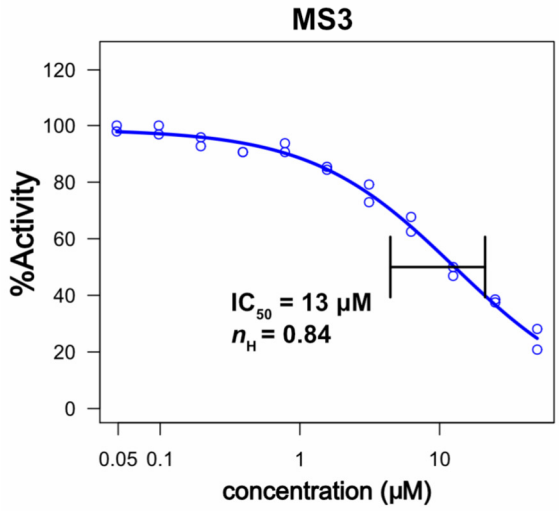

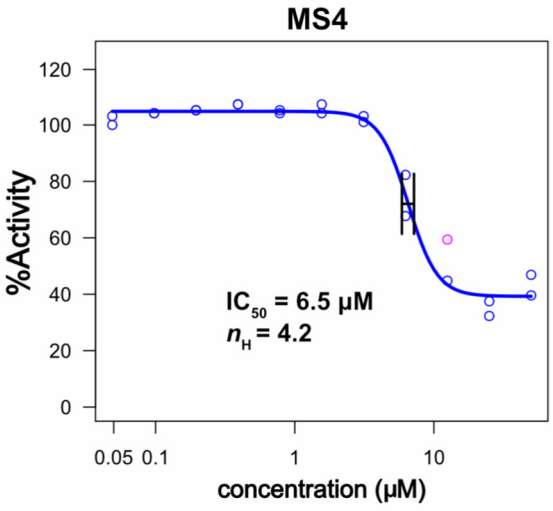

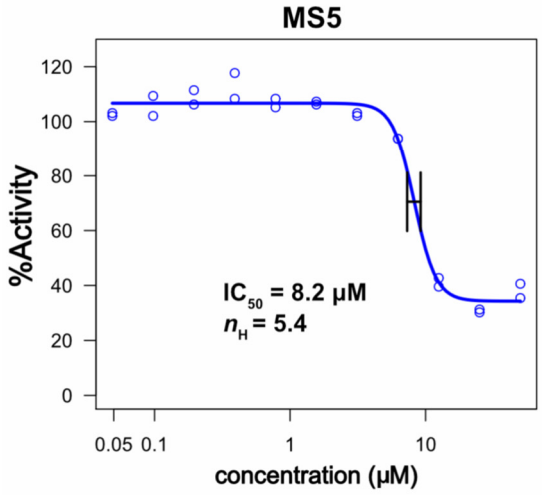

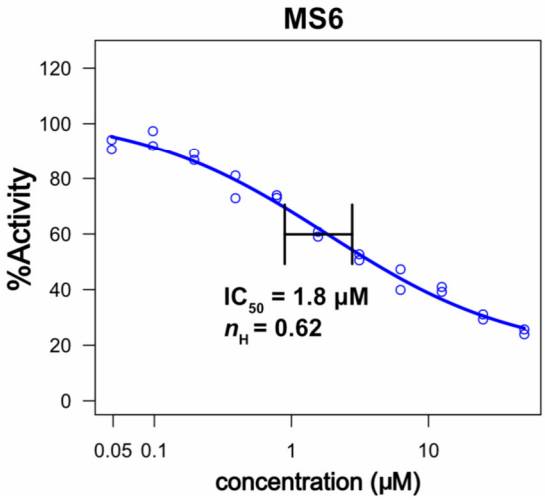

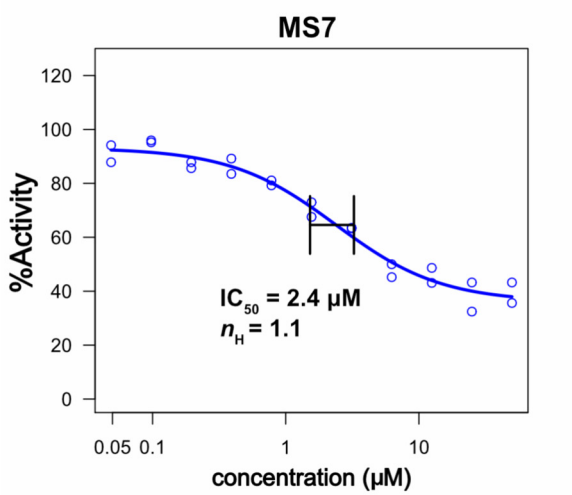
MS7
%Activity
120
100
80
60
40
20
0
IC50 = 2.4 µM
nH = 1.1
0.05 0.1
1
10
concentration (µM)

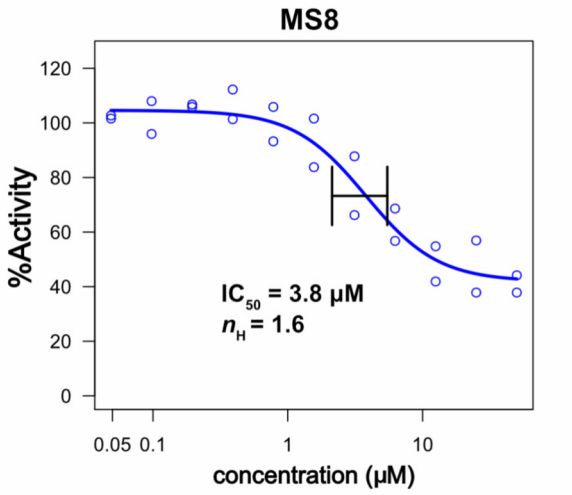
MS8
%Activity
120
100
80
60
40
20
0
IC50 = 3.8 µM
nH = 1.6
0.05 0.1
1
10
concentration (µM)

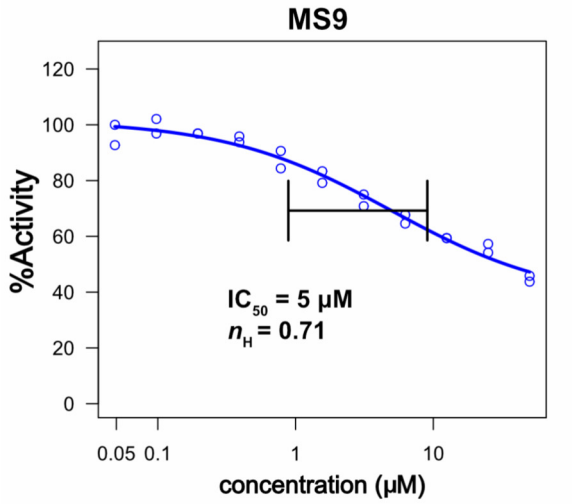
MS9
%Activity
120
100
80
60
40
20
0
IC50 = 5 µM
nH = 0.71
0.05 0.1
1
10
concentration (µM)

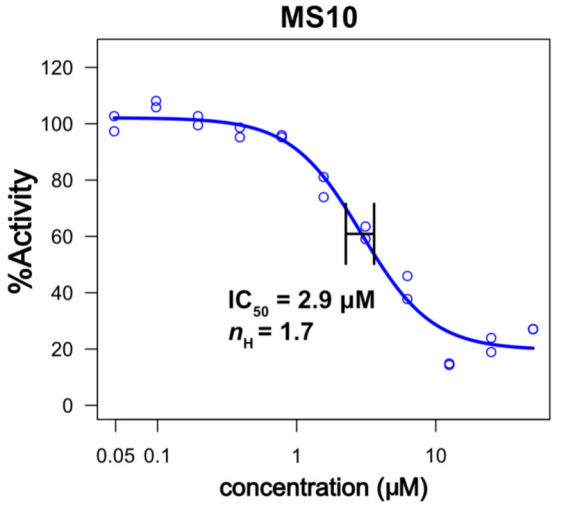
MS10
%Activity
120
100
80
60
40
20
0
IC50 = 2.9 µM
nH = 1.7
0.05 0.1
1
10
concentration (µM)

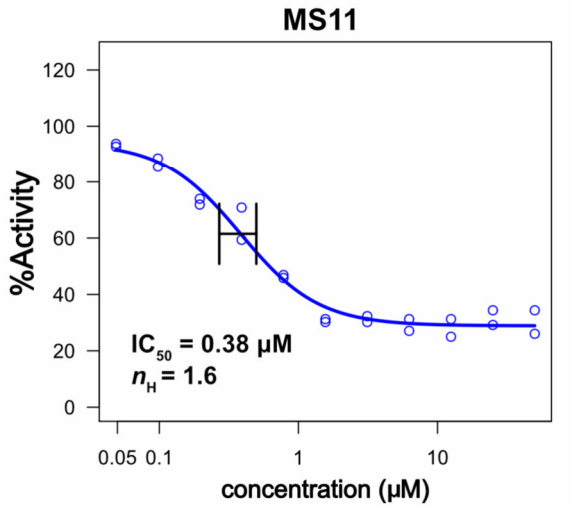
MS11
%Activity
120
100
80
60
40
20
0
IC50 = 0.38 µM
nH = 1.6
0.05 0.1
1
10
concentration (µM)

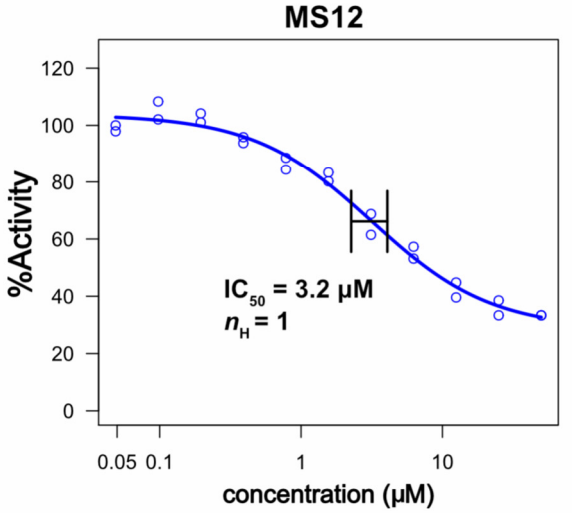
MS12
%Activity
120
100
80
60
40
20
0
IC50 = 3.2 µM
nH = 1
0.05 0.1
1
10
concentration (µM)

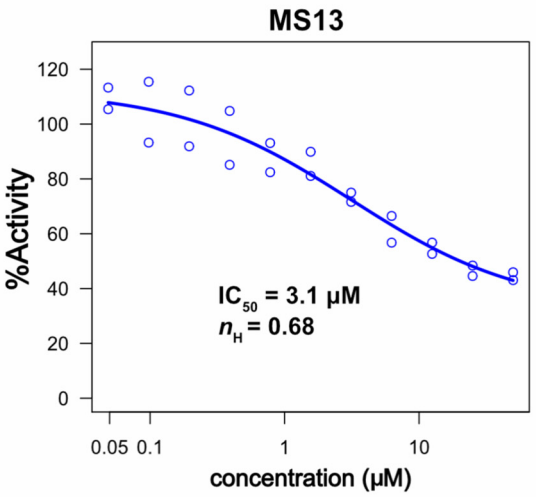
MS13
%Activity
120
100
80
60
40
20
0
IC50 = 3.1 µM
nH = 0.68
0.05 0.1
1
10
concentration (µM)

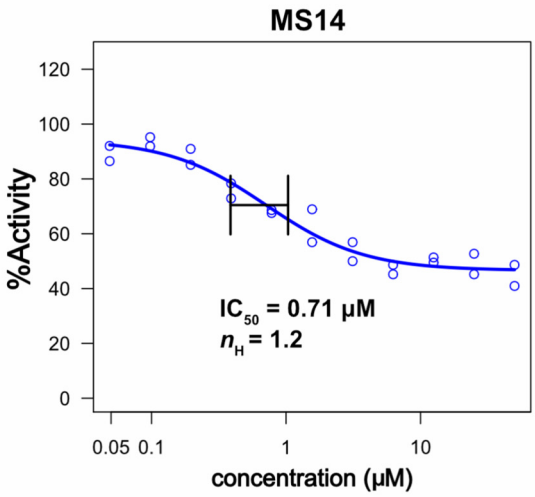
MS14
%Activity
120
100
80
60
40
20
0
IC50 = 0.71 µM
nH = 1.2
0.05 0.1
1
10
concentration (µM)

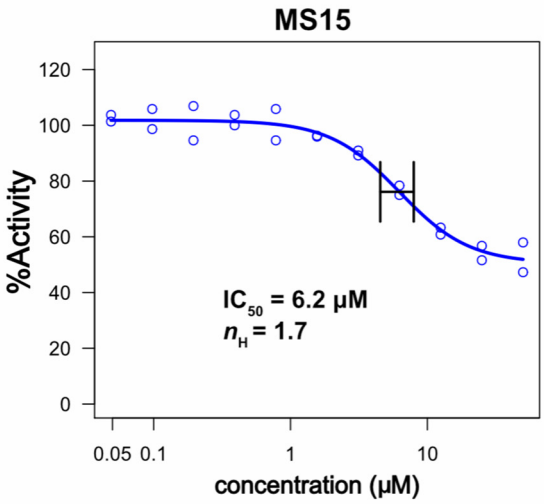
MS15
%Activity
120
100
80
60
40
20
0
IC50 = 6.2 µM
nH = 1.7
0.05 0.1
1
10
concentration (µM)

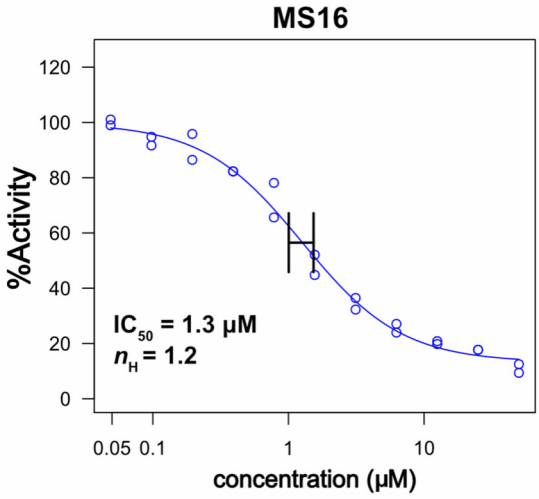
MS16
%Activity
120
100
80
60
40
20
0
IC50 = 1.3 µM
nH = 1.2
0.05 0.1
1
10
concentration (µM)

9.2. Appendix B: EHDs and Drp1 structures

Protein	PDB	Nucleo-tide	Species	Method	Resolution (Å)	Reference
EHD						
EHD1	2JQ6	-	*Homo sapiens*	Solution NMR	-	Kiken et al., 2007
EHD2	2QPT	AMPPNP	*Mus musculus*	XRD	3.1	Daumke et al., 2007
EHD2	4CID	AMPPNP	*Mus musculus*	XRD	3.0	Shah et al., 2014
EHD4	5MTV	ATPγS	*Mus musculus*	XRD	2.79	Melo at al., 2017
EHD4	5MVF	ADP	*Mus musculus*	XRD	3.27	Melo at al., 2017
Dynamin related protein						
Drp1	3W69	GMPPNP	*Homo sapiens*	XRD	2.0	Kishida and Sugio et al., 2013
Drp1	3W6O	GMPPCP	*Homo sapiens*	XRD	1.9	Kishida and Sugio et al., 2013
Drp1	3W6P	GDP-AlF4	*Homo sapiens*	XRD	1.7	Kishida and Sugio et al., 2013
Drp1	5WP9	MID49	*Homo sapiens*	cryo-EM	4.22	Kalia et al., 2018
Drp1	4BEJ	-	*Homo sapiens*	XRD	3.5	Frohlich et al., 2013
Drp1	4HIV	GMPPNP	*Homo sapiens*	XRD	2.3	Wenger et al., 2012

9.3. Appendix C:Script

Semi-automated script for measuring lipid droplet area

```
/*
 * Macro template to process multiple images in a folder
 */

#@ File (label = "Input directory", style = "directory") input
#@ File (label = "Output directory Images", style = "directory") output_image
#@ File (label = "Output directory CSV", style = "directory") output
#@ File (label = "Output directory Segmentation", style = "directory") output_roi
#@ String (label = "File suffix", value = ".czi") suffix

// See also Process_Folder.py for a version of this code
// in the Python scripting language.

processFolder(input);

// function to scan folders/subfolders/files to find files with correct suffix
function processFolder(input) {
	list = getFileList(input);
	list = Array.sort(list);
	for (i = 0; i < list.length; i++) {
		//if(File.isDirectory(input + File.separator + list[i]))
		//	processFolder(input + File.separator + list[i]);
		if(endsWith(list[i], suffix))
			processFile(input, output, output_image, list[i]);
	}
	processFolderDroplet(output_image)
}
```

```
function processFolderDroplet(input) {
	list = getFileList(input);
	list = Array.sort(list);
	for (u = 0; u < list.length; u++) {
		//if(File.isDirectory(input + File.separator + list[i]))
		//	processFolder(input + File.separator + list[i]);
		if(endsWith(list[u], ".tif"))
			processFileDroplet(output, output_image, list[u]);
	}
}

function processFileDroplet(output, output_image, file) {
	open(output_image + "\\" + file);
	MeasureDroplets();
}

function processFile(input, output, output_image, file) {
	// Do the processing here by adding your own code.
	// Leave the print statements until things work, then remove them.
	open(input + "\\" + file);
	run("Brightness/Contrast...");
	run("Enhance Contrast", "saturated=0.35");
   waitForUser("Add all cells to ROI-manager, then hit OK");
   nROIs = roiManager("count");
   for (i = 0; i<nROIs;i++){
	roiManager("select", i);
	run("Duplicate...", " ");
	name = substring(file, 0, lastIndexOf(file, "."));
	saveAs("Tiff", output_image +"/" + name+"_" + i + ".tif");
	close();
```

```
    }
    roiManager("reset")
        close();
        close();
}

function MeasureDroplets() {
        run("Duplicate...", " ");
        setAutoThreshold("Default dark");
    run("Threshold...");
    waitForUser("Adjust Threshhold for Droplets (press apply!!), then hit OK");
    run("Erode"); run("Erode");
    run("Dilate"); run("Dilate");
    run("Watershed");
    run("Analyze Particles...", "size=0-Infinity exclude add");
    waitForUser("This is your segmentation");
    run("Flatten");
    saveAs("JPG", output_roi + "/" + getTitle() + "_roi.jpg");
    close();
    if (roiManager("Count") > 0) {
    run("Select All");
    roiManager("Measure");
    saveAs("Results", output +"/Droplets" + file +".csv");
    }
    roiManager("reset")
    run("Clear Results");
        close();
}
```